COMMON PROPER ORTHOGONAL DECOMPOSITION-BASED EMULATION AND SYSTEM IDENTIFICATION FOR MODEL-BASED ANALYSIS OF COMBUSTION DYNAMICS

A Dissertation
Presented to
The Academic Faculty

by

Shiang-Ting Yeh

In Partial Fulfillment
of the Requirements for the Degree
Doctor of Philosophy in the
Department of Aerospace Engineering

Georgia Institute of Technology
August 2018

COMMON PROPER ORTHOGONAL DECOMPOSITION-BASED EMULATION AND SYSTEM IDENTIFICATION FOR MODEL-BASED ANALYSIS OF COMBUSTION DYNAMICS

Approved by:

Dr. Vigor Yang, Advisor
School of Aerospace Engineering
Georgia Institute of Technology

Dr. C.F. Jeff Wu
School of Industrial
Georgia Institute of Technology

Dr. Tim Lieuwen
School of Aerospace Engineering
Georgia Institute of Technology

Dr. Lakshmi Sankar
Aerospace Engineering
Georgia Institute of Technology

Dr. Joseph Oefelein
School of Aerospace Engineering
Georgia Institute of Technology

Date Approved: [May 10, 2018]

ACKNOWLEDGEMENTS

Foremost, I would like to express my sincere gratitude to my advisor Prof. Vigor Yang for the continuous support of my Ph.D study and research, for his patience, motivation, enthusiasm, and immense knowledge. His guidance helped me in all the time of research and writing of this thesis. I could not have imagined having a better advisor and mentor for my Ph.D study.

Besides my advisor, I would like to thank the rest of my thesis committee: Prof. Joseph Oefelein, Prof. Tim Lieuwen, Prof. Lakshmi Sankar, and Prof. C.F. Jeff Wu, for their encouragement, insightful comments, and hard questions.

I thank my fellow labmates in the Yang Group: Xingjian Wang, Yixing Li, Liwei Zhang, Yanxing Wang, Yu-Hung Chang, Murali Gopal Muraleedharan, Chris Lioi, Tim Dawson, along with ISyE counterparts: Simon Mak, Chih-li Sung for the stimulating discussions.

I also thank my girlfriend Ko-Chun Liu for her moral support. Last but not the least, I would like to thank my parents, An-I Yeh and Yueh-Ing Chang, for giving birth to me at the first place and supporting me throughout my life.

TABLE OF CONTENTS

LIST OF TABLES

LIST OF FIGURES

LIST OF SYMBOLS AND ABBREVIATIONS

Symbols

A	Geometrical characteristic parameter, area
a	Non-dimensional parameter of swirl injector
α	Spreading angle of the liquid spray
b	Non-dimensional parameter of swirl injector
c	Maximum % of circumference
c^*	Characteristic velocity
C_D	Discharge coefficient
γ	Ratio of specific heat, C_p/C_v
d	Diameter of injector element
δ	Wall thickness; slot width for 2D axisymmetric simulation
Δl	Distance from injector headend
Δp	Pressure drop
ϵ	Coefficient of jet contraction
f	Friction factor, or frequency
H	Transfer function (signal processing)
h	Annulus height (~liquid film thickness)
Im	Imaginary part of complex variable
L	Length of injector element
λ	Gas dynamic function; tangent of nozzle surface inclination to injector axis
M	Mach number
MR	Mixture ratio, momentum ratio

m	Number of rows
$\dot{m}$	Mass flow rate
μ	Mass flow coefficient
N	Number (count)
n	Number of tangential inlet passages
ν	Kinematic viscosity
ξ	Hydraulic-loss coefficient (steady), Liquid surface displacement (unsteady)
p	Pressure
Π	Response or transfer function
σ	Surface tension, or spacing between elements
Q	Volumetric flow rate
r	Radius of liquid film
R	Universal gas constant; radius of injector element
R_A	Inverse swirl number
Re	Reynolds number
ρ	Density
S	Surface
s	Step height
Sh	Strouhal number
T	Temperature, K, or inter-element spacing thickness
t	Time
U	Velocity
Φ	Phase angle
φ	Coefficient of passage fullness

V	Volume
v	Velocity of disturbance propagation
Ω	Amplitude of liquid surface wave
ω	Radian frequency

Subscripts

a, ax	Axial
b	Between
c	Injector cup
cc	Combustion chamber
choke	Choked flow constraint
e	Nozzle exit
el	Per element
eq	Equivalent
exp	Experimental
ex	Exit
ext	External
f	Propellant feed system, or fuel
face	Faceplate
fl	Flow
fr	Friction
g	Gas or gas-post
i	Injector
id	Ideal
in	Inlet

jet	Jet
k	Head end of injector/vortex chamber
m	Liquid vortex (in the manifold)
min	Minimum
n	Nozzle
o	oxidizer
or	Orifice
out	Outlet
r	Radial, recess
s	Vortex chamber
sw	Surface wave
Σ	Total
th	Throat
u	Circumferential
v	Vapor
vw	Vorticity wave
w	Wave
0	Stagnation

Superscripts

$\bar{}$ (bar)	Dimensionless parameter

Abbreviations

CFD	Computational fluid dynamics
CI	Confidence interval

CPOD	Common proper orthogonal decomposition
DLR	Deutsches Zentrum für Luft
DNS	Direct numerical simulation
DoE	Design of Experiments
FDF	Flame describing function
FFSC	Full-flow staged-combustion
FRSC	Fuel-rich staged combustion
FTF	Flame transfer function
GCLSC	Gas-centered liquid-swirl coaxial injector
GOx	Gaseous oxygen
GP	Gaussian process
LES	Large eddy simulation
LH_2	Liquid hydrogen
LOx	Liquid oxygen
MaxPro	Maximum projection
MBSE	Model-based system engineering
MCC	Main combustion chamber
MISO	Multiple-input, single-output
MLE	Maximum likelihood estimation
MSPE	Mean-squared prediction error
ORSC	Oxygen-rich staged combustion
PCA	Principle component analysis
POD	Proper orthogonal decomposition
PSD	Power spectral density
RBNN	Radial basis neural networks

RMSRE	Root-mean-square-relative error
RP-1	Rocket fuel
RSA	Response surface approximations
SI	System identification
SISO	Single-input, single-output
TCA	Thrust chamber assembly
UQ	Uncertainty quantification

SUMMARY

Physical experiments on high-performance power generation and propulsion systems, such as those of airbreathing and rocket engines, are expensive due to the harsh requirements of operating conditions and high level of system complexity. In addition, it is difficult to gain information about the underlying mechanisms of the physiochemical processes involved because of the limited insight offered by optical diagnostics available at such extreme operating conditions. High-fidelity simulations can be employed to capture more salient features of the flow and combustion dynamics in engines. However, these computations are often too expensive and time-consuming for design purposes.

To enable use of modeling and simulation in the design workflow, the present study proposes a data-driven framework for modeling and analysis to facilitate decision making for combustor designs. Its core is a surrogate model employing a machine-learning technique called kriging, which is combined with data-driven basis functions to extract and model the underlying coherent structures from high-fidelity simulation results. This emulation framework encompasses key design parameter sensitivity analysis, physics-guided classification of design parameter sets, and flow evolution modeling for efficient design survey. A sensitivity analysis using Sobol' indices and a decision tree are incorporated into the framework to better inform the model. This information improves the surrogate model training process, which employs basis functions as regression functions over the design space for the kriging model. The novelty of the proposed approach is the construction of the model through Common Proper Orthogonal Decomposition, allowing for data-reduction and extraction of common coherent structures. The significantly reduced

computation time required for evaluating new design points enables efficient survey of the design space.

To further utilize simulation results and connect component design with overall system performance, a data analytic methodology is used to quantify the combustion dynamics and used for system-level stability analysis. The distributed response serves as an acoustic source term in the generalized wave equation, which can be used to assess the stability of complex propulsion systems. Treating the extracted coherent structures as time series signals, the combustion response can be deduced through autoregressive model selection, accounting for data sparsity, multicollinearity, and noise. The results show that acoustic-vortical dynamics is the dominant mechanism determining flame stabilization. This data-driven methodology quantifies the gain and phase relationship between flowfield variables and unsteady heat release. The methodology not only accounts for the distributed combustion response through incorporation of proper orthogonal decomposition (POD) analysis, but also uses the data to identify relevant time scales, circumventing the need for forcing and focusing on intrinsic dynamics. Thus, a design survey of the system stability based on the injector dynamics can be conducted.

CHAPTER 1. INTRODUCTION

In modern design methodologies, much of the procedure revolves around testing. With respect to rocket engine development, the F-1 engine is often treated as an example of high capital investment and innovative development, leading to the success of landing on the moon. However, the amount of testing required to achieve such a feat was high. Physical experiments on high-performance power generation and propulsion systems, such as those of airbreathing and rocket engines, are extremely expensive, due to the harsh operating conditions and high level of system complexity [1-3]. Furthermore, the operating conditions limit the use of many types of diagnostic techniques; optical diagnostics are typically the method of choice. These methods, however, offer limited insight into the underlying mechanisms of the physiochemical processes involved [4-6]. Experimental information alone is not enough to fully analyze, design and optimize the propulsion system, so existing design practices rely on past experience, empirical calculations, and intuition.

High-fidelity simulations can be employed to capture more salient features of the flow and combustion dynamics in engines [7, 8], but these computations are often too expensive and time-consuming for design purposes. In the development process, achieving an optimal design requires models capable of evaluating alternative designs and identifying trade-offs in a timely manner. Furthermore, the formulation of such models requires understanding of the key physics and the incorporation of decision making to resolve multiple, potentially conflicting, requirements. The present study, as a specific example, treats a simplex swirl injector, a central component of many airbreathing and rocket

combustion devices [9-11], including rich flow physics. Each high-fidelity calculation of the three-dimensional flow evolution using the Large Eddy Simulation (LES) technique takes about 500,000 CPU hours to obtain statistically meaningful data for a grid of 4 million mesh points [12, 13]. Given the number of geometric attributes and operating conditions to be surveyed, the design space exploration necessitates a prohibitive number of sample points.

This chapter presents a general introduction to rocket engine development and the issues that motivate the work. Past and current design practices for selecting engine components are described and their limitations are noted. Then, an outline for the subsequent chapters is presented.

1.1 Staged Combustion

Liquid bi-propellant engines usually contain three primary components: the thrust chamber that burns the propellants, a turbopump assembly that uses a turbine to drive propellant pumps, and a mechanism for creating high-enthalpy flow that drives the turbine [14]. The method used to create the high-enthalpy flow categorizes the propulsion system. Figure 1 shows the flow diagrams of three cycles for liquid rocket engines. In an expander cycle, the propellant is heated by going through propellant lines around the combustion chamber and the nozzle, then passes through the turbine to be burned in the chamber. This simple method cannot generate a large pressure head to drive a turbine, and is limited to smaller engines like the RL-10.

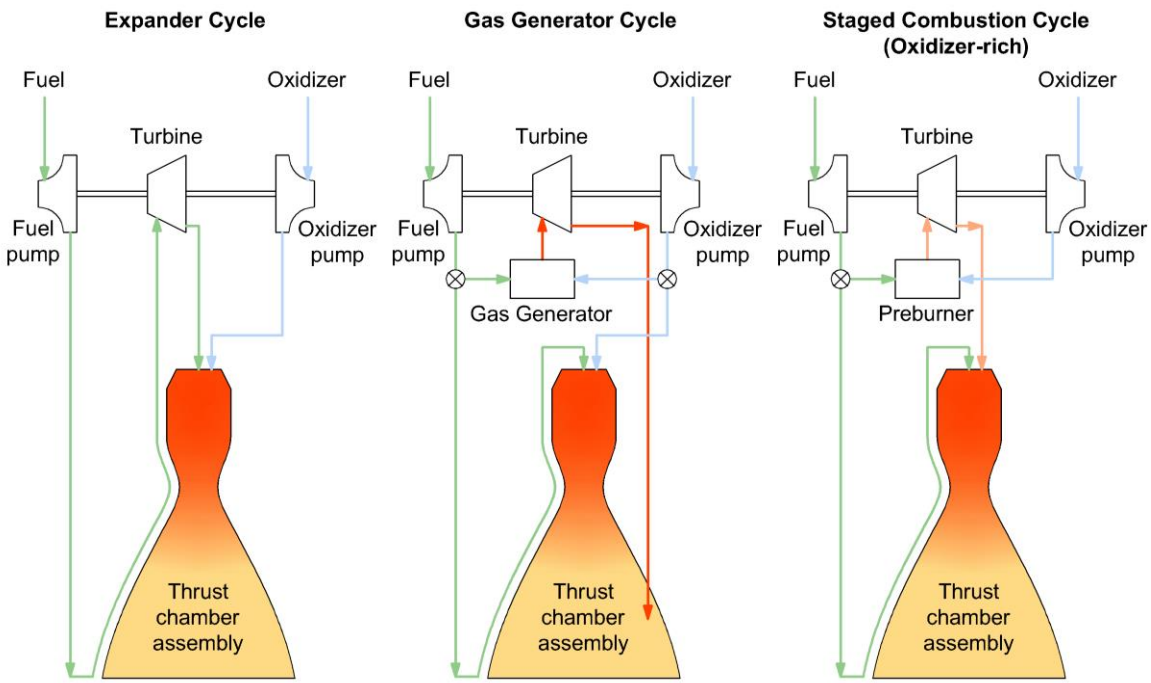

Figure 1. Engine cycle flow diagrams [14]

The gas generator cycle uses a secondary combustion chamber to burn a fraction of the propellant and the exhaust is passed through the turbine before being dumped in the expanding nozzle. This has been a standard design for low pressure (< 100 atm) liquid oxygen (LOx)/RP-1 engines in the US. The most famous example is the F-1 engine in the Saturn V that took the Apollo program to the Moon.

Staged-combustion cycle engines takes one step further and uses one or more preburners to burn a portion of the propellant, then passes the hot gas products through the turbine before entering the combustion chamber where it combusts with the rest of the propellant. This complex design offers the highest performance for high mass flow rate engines, as seen in the RD-180 engine used by the Atlas V launch vehicle.

1.1.1 Advantages of Staged-Combustion Engine Cycles

The staged-combustion cycle offers several advantages. The obvious advantage of the staged-combustion cycle is the fact that all of the available propellant goes through the combustion chamber, removing secondary flow losses present in gas generator cycles. The entirety of the propellant is expanded through the nozzle, maximizing the accelerated mass flow rate.

Another advantage is the high pressure generated by the turbopump system, increasing the pressure ratio and cycle efficiency. The high pressures not only promote complete combustion, but also allow for higher nozzle expansion ratios and increased specific impulses. Generally, staged-combustion engines increase specific impulse by 5-10% compared to engines running on open cycles. In addition, high-pressure operation allows the propellant fluid to be in the supercritical regime. As the flow can be considered a single phase with no vaporization, flow instabilities and combustion sensitivity to the propellant flow is reduced. In addition, low-pressure gas experiments can be utilized to model the supercritical flow behavior, reducing early phase design costs.

There has been increased interest in LOx/kerosene staged-combustion engines for first stage booster applications. Over time, payloads and mission complexity have increased, and the required performance of first stage engines have increased. LOx/kerosene engines offer high thrust density and thrust-to-weight ratios, while having better control and specific impulse than solid propellant stages. LOx/liquid hydrogen ($LH_{2)}$ engines that have lower thrust densities and higher specific impulses require larger volume

propellant tanks, which increase vehicle dry mass. Thus, staged-combustion LOx/RP-1 provide the optimal compromise between thrust density and specific impulse.

1.1.2 Challenges of Staged-Combustion Cycle Engines

While staged-combustion engines provide superior performance, the design creates additional challenges. The added complexity, of ducting the preburner exhaust through the turbine(s) and into the combustion chamber, requires more complex and heavier components. There is an additional design requirement of preburner exhaust not exceeding the temperature limits of the turbine blades while providing enough high-enthalpy flow to power the turbopumps. Another concern associated with engine complexity is the potential for coupling of flow instabilities with the system dynamics. Preburner combustion dynamics may induce flow instabilities in the turbine, which can propagate into the thrust chamber assembly (TCA) and excite thermoacoustic instabilities. Therefore, preventing the coupling of these instabilities becomes a key design objective that is typically accomplished by injector acoustic tuning and baffles [15].

Preburner exhaust in oxygen-rich staged combustion (ORSC) engines is a hot oxidizing gas, so most metals are subject to material oxidation and even metal ignition. To prevent material failures, materials and coatings resistant to oxidation are typically applied. Fuel-rich staged-combustion (FRSC) has historically been implemented with LOx/LH_2 propellants, so the cryogenic temperatures of the fuel lead to concerns of hydrogen embrittlement. The non-equilibrium combustion can result in soot formation and coking within the propellant feed lines. First-order power balance calculations have shown that

oxygen-rich preburners provide 87% higher chamber pressures than fuel-rich cycles, considering equal system temperatures and peak system pressures [16].

Full-flow staged-combustion (FFSC) features two separate preburners that each drive a separate propellant turbopump and its schematic is shown in Fig. 2. This cycle allows for higher mass flow rates, which produces smaller pressure drops to drive pumps and higher pressures in the main combustion chamber (MCC). A case study involving a hypothetical LOX/LH_2 engine shows that while the power required to drive an FFSC engine is approximately 13% greater than that of a more traditional fuel-rich power cycle, the turbine power produced under similar preburner temperatures and pressures is over 40% greater for a FFSC power cycle [16]. Although theoretically superior to the other cycles, no FFSC engine has been successfully flown, although it should be noted SpaceX's Raptor engine is currently undergoing development testing.

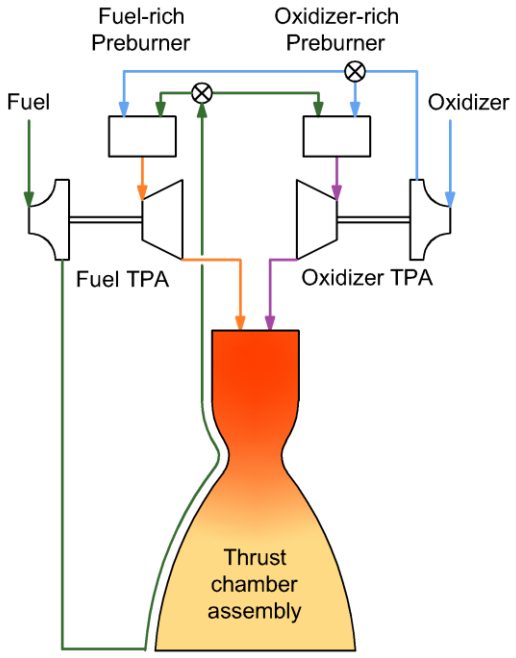

Figure 2. Full-flow staged combustion flow diagram.

Combustion instabilities pose a great threat at the extremely high pressures of high-power engines, as any significant pressure fluctuation can easily push the operating conditions beyond the material limits. Major stability issues were, for example, encountered in the F-1 engine development program, as reviewed by Oefelein and Yang [17]. Project First tackled the major undertaking of eliminating these issues in the F-1 engine; over 2000 full-scale tests (62.5% of all F-1 full-scale development tests) were conducted during that program, to evaluate injector designs and baffle arrangements aimed at combustion instability mitigation.

There are a few benefits to the high pressures. Since the fluids are within the supercritical regime, there is no longer any difference between the gas and liquid phases. Thus, no vaporization occurs and the mixture can be treated as a single fluid. Still, major efforts are required to alleviate instabilities. Injector design selection and tuning have been the main methods for dealing with this problem. Circular and radial baffles constituted from injection elements protruding into the combustion chamber were the solution chosen for the RD-170 engine [15, 18].

1.2 Current and Past Design Practices

Injectors of the past and even of today are primarily design through the use of empirical models [10, 15]. Simple sub-scale tests, which are then scaled to full-scale, have provided the basis for design decisions. Cold flow tests are used to explore the mixing capabilities of an injection design, measuring performance metrics such as spreading angle and liquid film thickness [19, 20]. Various design parameters are tested through modular thrust chamber apparatus [21-25]. In this way, the entire system can be analyzed and

designed by switching out injectors, changing chamber length and nozzles in addition to varying the operating conditions such as chamber pressure and mass flow rates.

However, most experimental techniques are insufficient to predict for many conditions that could enhance injector performance or combustion chamber life. For this reason, researchers now look to use simulation techniques to aid in injector design. The inherent issue with simulations is the need for rigorous validation of the models themselves and the length computational times associated with multi-element injector flows.

With adequate validation, high-fidelity simulations are typically incorporated in modern design practices. Experimental correlations and classical theories can be used to determine the preliminary design. Then, simulations are used to fine-tune or analyze the design. In addition, using modeling and simulation in coordination with optimization techniques can enable efficient trade-off studies for complex design problems.

In the early design stages of complex systems, there is a need to survey the design space to identify the optimal range for design parameters and feasible starting points [26]. An integrated design process of combining design principles such as Taguchi methods and response surface methodology [27] into one mathematical framework can be used to address this multi-objective design concept problem. The critical component of the optimization problem is properly identifying the objective function. From a combustion dynamics perspective, quantifying and formulating the objective function is a great challenge as there is no clear metric for combustion stability. In most cases, a designer can only conclude relative stability margins with respect to the different configurations, making this problem a great challenge.

1.3 Research Objectives

As previously mentioned, the simulations at hand require long run times and optimization based on an inexpensive surrogate is required. For the spatio-temporal simulations, a surrogate model needs to be formulated such that the essential flow physics are captured. Surrogate-based optimization can provide quantitative assessment of design trade-offs and facilitate global sensitivity evaluations of the design parameters. A major challenge to the successful full-scale development of aerospace systems is dealing with competing objectives such as vehicle performance, system stability, and manufacturing cost [28]. The surrogates constructed using data drawn from high-fidelity simulations and provide efficient approximations of the objectives at new design points, rendering trade-off studies feasible. As a sufficient number of different designs must be tested to build the surrogate model, the process of selecting different designs is Design of Experiments (DoE) [27, 29]. DoE is a statistical methodology to determine the ideal training dataset for surrogate modeling, based on a given design space. The details of DoE will be elaborated in 3.3.1.

The data required for formulating the surrogate model can be severely limited due to time and computational constraints of the high-fidelity simulations. In some cases, this problem can be alleviated by performing a low-fidelity model and translating the result to the higher-fidelity model. In other instances, low-fidelity data, employing corrections for improved accuracy, can be combined with the high-fidelity data to reduce the overall number of expensive runs. With the continuing progress of modeling capabilities, simulation-based optimization has proven to be a useful tool in the design process.

However, complex design problems such as rocket engine components can still be a daunting task.

Rocket engine component design is a complex process that can be more straightforward and efficient by combining computational fluid dynamics (CFD) and data-driven surrogate modeling, along with connecting component and system level analysis. Model-based design of propulsion systems can be challenging due to initial time and computational constraints. Tools like low-fidelity analysis and design of experiments help reduce computational expense. With an established database, the model framework enables efficient trade-off analysis for design space surveys. This capability is the return on the early investment into time and computational resources for creating a data vault for a particular set of operating conditions and geometric configurations.

The objective of this research is to develop a framework for enabling and supporting design decisions, utilizing modeling and simulation. The present work applies new machine-learning techniques and investigates the practical performance of the emulator with respect to flow physics. In order to maximize the benefits of efficient design surveys using the spatio-temporal reduced order model, a design objective must be selected. In addition, the component design should be linked to the overall system performance. Besides thermal management and combustion efficiency, combustion instability is of utmost importance in all combustion devices because of its destructive potential, but especially in the high-pressure combustion chambers of rocket engines. Thus, there is a need to characterize the complex and nonlinear nature of combustion dynamics to advance engine design methodologies.

Comprehensive combustion stability analysis has long been sought after, as *a priori* understanding of the coupling mechanisms would greatly reduce the number of tests and the capital required for developing new engines. To reiterate, there is a necessity to identify and quantify the physical mechanisms operating over multiple time and length scales involved in combustion dynamics. The proposed methodology leverages high-fidelity LES in combination with machine-learning techniques to quantify the distributed combustion response. This response is intended to serve as an acoustic source term in the generalized wave equation, which can analyze the stability of complex propulsion systems.

1.4 Dissertation Outline

The thesis is structured as follows. In Chapter 2, a review of injector dynamics is illustrated, shedding light upon key flow physics and baseline design procedures deduced from theory. Chapter 3, presents the data-driven framework utilizing modeling and simulation and the application of the framework is shown, while assessing the surrogate model using performance metrics, root-mean-square errors, and power spectrum density (PSD) of simulated and predicted flowfields. Chapter 4 discusses an extracted response, in the form of a flame transfer function that links the component design to a specific system-level performance. The section further explains the methodology for data correlation and system identification to quantify the combustion dynamics. Chapter 5 provides an example of system-level analysis and Chapter 6 concludes with a summary, along with directions for future work.

CHAPTER 2. INJECTOR DYNAMICS AND DESIGN

2.1 Injector Design

In order to advance rocket injector technology, the flow field characteristics, design constraints, and injector dynamics need to be understood, and design tools that will help analyze and predict this set of parameters are necessary. All underlying mechanisms, physics, and known factors dictating the behavior for the preburner and main combustor injectors of ORSC engines have to be identified, investigated, and quantified. The design tools are the end result of this process. Furthermore, the selection and design of an injector should be based on several considerations: combustion efficiency, thermal loading management, combustion stability, and manufacturing constraints [10].

Injection elements provide mixing and atomization of the propellants for combustion chambers and preburners. These processes determine the effects of combustion efficiency, combustion stability and heat transfer characteristics. The basic requirements that injectors must fulfill are:

1) High combustion efficiency – the mixture ratio and flow intensity should be homogeneous in the majority of the chamber, while the pressure drop across the injection elements should be minimized
2) Protection from overheating – the mixture ratio near walls and baffles may be modified to reduce the thermal loads on them
3) Suppression of combustion and flow instabilities – the injectors should be designed to damp acoustic energy from the system and have low sensitivity to

operating condition changes, providing stable operation throughout the prescribed operating range

Russian-developed swirl injectors currently employed by the RD-170 engines have many advantages over impinging jet injectors. For the same pressure drop and mass flow rate, the atomization rates of the propellants are significantly improved by the implementation of swirl injectors, due to the formation of a hollow spray cone. Swirl injectors rely on their dynamics rather than injector orientation for mixing, so they have higher tolerance and less sensitivity to manufacturing defects. They also self-tune during transient conditions, thus simplifying startup operation. Furthermore, cavitation or choking of the passage is less likely to occur with swirl injectors due to the larger flow passage area. Although liquid film development imposes a longer startup time, this bears no consequence for the first-stage ORSC rocket engines of interest.

Their advantages outweigh their disadvantages, but the design of swirl injectors has yet to be fully understood. Swirl injectors have many key design parameters that affect performance, and these effects have yet to be identified, explored and quantified. While performance is not simple to evaluate and quantify, swirl injector performance is typically described by the liquid film thickness and spreading angle at the injector exit. The former dictates the size of the liquid droplets after film break-up, and the latter affects the intra-element mixing efficiency.

To advance injector technology, a clear design methodology is required to better predict injector performance and establish a preliminary injector design. The development of this procedure requires capturing all the factors that affect the flow field of the injector,

and quantifying how each factor affects the performance. The basis of the design will focus on hydrodynamic theory as detailed by Bazarov et al. [10]. The theory for gaseous monopropellant jet and ideal swirl injectors will be combined to formulate the design methodology for bipropellant injectors used in the MCC (and the preburner for completeness). The methodology for liquid bipropellant swirl injector with internal mixing is corrected for injector dynamics and propellant mixing time. In addition, acoustics have also been incorporated into design considerations, treating the gaseous post of the injector as an acoustic resonator, with the length tuned to a half-wave length [15]. For a given system and mission requirement, a power balance establishes the parameters such as flow rates and mixture ratios throughout the system.

The operating conditions for the RD-170 are well summarized by Manski et al. [30]. Injector schematics for the MCC injectors are also publicly available in a U.S. Patent application [31]. These sources provide the starting point for the preliminary injector design proposed by the described injector design theory. The baseline configuration is established here using the extended design methodology based on hydrodynamic and acoustic considerations for the combustion chamber.

The subsequent section will briefly review the key hydrodynamic theories detailed in Chapter 2 of the *Liquid Rocket Thrust Chambers: Aspects of Modeling, Analysis, and Design* [10]. The design procedure is based on conservation of mass and momentum, using the principle of maximum flow rate to close the formulation for swirl injector hydrodynamic theory. Table 1 shows the symbol nomenclature for the derivation and the design procedure section.

Table 1. Symbol nomenclature

Parameter	Variable Definition
A	Geometrical characteristic parameter, area
a	Non-dimensional parameter of swirl injector
α	Spreading angle of the liquid spray
b	Non-dimensional parameter of swirl injector
c	Maximum % of circumference
c^*	Characteristic velocity
C_D	Discharge coefficient
γ	Ratio of specific heat, C_p/C_v
d	Diameter of injector element
δ	Wall thickness; slot width for 2D axisymmetric simulation
Δp	Pressure drop
ϵ	Coefficient of jet contraction
f	Friction factor, or frequency
h	Annulus height (~liquid film thickness)
Im	Imaginary part of complex variable
L	Length of injector element
λ	Gas dynamic function; tangent of nozzle surface inclination to injector axis
M	Mach number
MR	Mixture ratio, momentum ratio
m	Number of rows
$\dot{m}$	Mass flow rate
μ	Mass flow coefficient
N	Number (count)
n	Number of tangential inlet passages
ν	Kinematic viscosity
ξ	Hydraulic-loss coefficient (steady), Liquid surface displacement (unsteady)
p	Pressure
Π	Response or transfer function
σ	Surface tension, or spacing between elements

Q	Volumetric flow rate
r	Radius of liquid film
R	Universal gas constant; radius of injector element
R_A	Inverse swirl number
Re	Reynolds number
ρ	Density
S	Surface
s	Step height
Sh	Strouhal number
T	Temperature, K, or inter-element spacing thickness
t	Time
U	Velocity
Φ	Phase angle
φ	Coefficient of passage fullness
V	Volume
v	Velocity of disturbance propagation
Ω	Amplitude of liquid surface wave
ω	Radian frequency

Subscripts

a, ax	Axial
b	Between
c	Injector cup
cc	Combustion chamber
choke	Choked flow constraint
e	Nozzle exit
el	Per element
eq	Equivalent
exp	Experimental
ex	Exit
ext	External
f	Propellant feed system, or fuel
face	Faceplate
fl	Flow

fr	Friction
g	Gas or gas-post
i	Injector
id	Ideal
in	Inlet
jet	Jet
k	Head end of injector/vortex chamber
m	Liquid vortex (in the manifold)
min	Minimum
n	Nozzle
or	Orifice
out	Outlet
r	Radial
s	Vortex chamber
sw	Surface wave
Σ	Total
th	Throat
u	Circumferential
v	Vapor
vw	Vorticity wave
w	Wave
0	Stagnation

Superscripts

$^{-}$ (bar)	Dimensionless parameter

2.2 Hydrodynamic Theory of Jet Injectors

Classical monopropellant jet injector, shown schematically in Fig. 3, can be analyzed based on Bernoulli's theorem. The mass flow rate of a jet injector can be calculated from

$$p_{01} = p_1 + \frac{\rho U_1^2}{2} = p_2 + \frac{\rho U_2^2}{2} + \Delta p_{1-2} \tag{2.1}$$

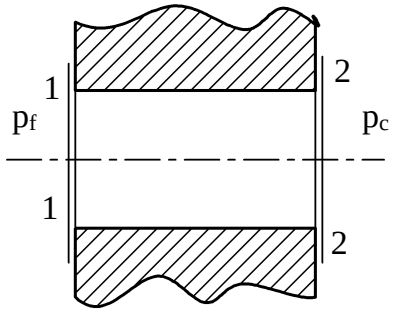

Figure 3. Schematic diagram of jet injector [10].

However, due to the fact that the exit flow area is usually smaller than the nozzle cross sectional area, a coefficient of jet contraction is required to enforce continuity. For continuous exhaust, $A_2 = A_n$ and $\varepsilon = 1.0$. If the propellant is fed from a large manifold (the case for the MCC injectors for ORSC engines), the inlet velocity can be neglected and the static pressure is equivalent to the stagnation pressure. The pressure drop across the injector can then be obtained, while accounting for any hydraulic losses. For an ideal fluid with no hydraulic losses, the mass flow rate equation becomes:

$$\dot{m}_{i,id} = A_n\sqrt{2\rho\Delta p_i} \tag{2.2}$$

The liquid flow is separated from the sharp edge at the entrance of the injector due to the inertia. The flow then continues and expands through the rest of the injector. The jet contraction from the flow forms an annular space between the jet and the wall when the ratio between the length and the diameter is less than 1.5. Since this flow is unstable and reduces the mass flow rate, short injectors are rarely used and higher aspect ratios are

desirable. Cavitation is still an issue for high velocity flows inside injectors that are sufficiently long.

Cavitation occurs in the exit flow when the pressure difference across the orifice reaches a critical value. If the inlet corner of an orifice is sharp enough to cause flow detachment, cavitation starts with a vapor region forming inside the orifice. If the downstream pressure is low enough, the cavitation worsens and the vapor region grows beyond the exit of the orifice. In order to prevent this, the orifice must be rounded enough to avoid flow detachment and the pressure drop must be kept sufficiently low. Another way of viewing cavitation inception is that the pressure recovery has to be enough such that the local pressure is greater than the vapor pressure. The pressure recovery has to be slower behind the orifice to prevent violent cavity implosions if cavitation has started. The degree of cavitation can be estimated with the non-dimensional parameter *Ca*, the cavitation number, described by:

$$Ca = 2\frac{(p - p_v)}{\rho U^2} \tag{2.3}$$

For gaseous combustible mixtures, the formulation is based on conservation of mass and energy along with the equation of state. Equation (2.2) is the result of mathematical manipulation of the conservation of mass and momentum via the pressure drop across the injector. The mass flow rate of the injector can be expressed as

$$\dot{m}_i = \mu \rho_2 U_2 A_2 \tag{2.4}$$

where μ is the flow coefficient. The gas density of at the injector exit can be obtained by assuming isentropic flow throughout the passage, resulting in the state equation:

$$\rho_2 = \rho_{01}\left[\frac{p_2}{p_{01}}\right]^{1/\gamma} \tag{2.5}$$

The ideal exit velocity becomes

$$U_2 = \sqrt{\frac{2\gamma}{\gamma-1}RT_{01}\left[1-\left(\frac{p_{cc}}{p_{01}}\right)^{\frac{\gamma-1}{\gamma}}\right]} \tag{2.6}$$

where the ratio of the specific heats is denoted by γ and the gas constant is denoted by R. The sum of the chamber pressure p_c and the injector pressure drop Δp_i is the total pressure of the gas flow denoted by p_{01}. The total temperature T_{01} is the gas temperature in the manifold.

A velocity coefficient λ can be defined as

$$\lambda_2 = \frac{U_2}{U_{th}} = \sqrt{\frac{\gamma+1}{\gamma-1}\left[1-\left(\frac{p_{cc}}{p_{01}}\right)^{\frac{\gamma-1}{\gamma}}\right]} \tag{2.7}$$

where

$$U_{th} = \sqrt{2\frac{\gamma}{\gamma+1}RT_{01}} \tag{2.8}$$

With the use of a characteristic velocity defined as

$$c^* = \frac{\sqrt{\gamma R T_{01}}}{\gamma\sqrt{[2/(\gamma+1)]^{(\gamma+1)/(\gamma-1)}}} \tag{2.9}$$

and gas dynamic coefficient function

$$q(\lambda_2) = \left(\frac{\gamma+1}{2}\right)^{\frac{1}{\gamma-1}} \lambda_2 \left(1 - \frac{\gamma-1}{\gamma+1}\,\lambda_2^2\right)^{\frac{1}{\gamma-1}} \tag{2.10}$$

the injector mass flow rate can be expressed as

$$\dot{m}_i = \mu \frac{(p_{cc} + \Delta p_i) A_n}{c^*} q(\lambda_2) \tag{2.11}$$

There is an ideal exit velocity for a given operating condition and propellant. With given conditions such as mass flow rate and pressure drop, this exit velocity can be used to size the injector that will be discussed in a later section

2.3 Hydrodynamic Theory of Swirl Injectors

The formulation of injector dynamics is based on the fundamental principles of conservation of mass, momentum, angular momentum, and maximum flow. Using these principles, analytic equations are derived to capture and quantify injector behavior based on a few design parameters. The results are then coupled with experimental results to 4produce a design procedure. For a swirl injector, the most important parameter is the geometric characteristic constant *A*, which is indicative of swirl strength and can be used to predict the liquid film thickness and spreading angle of a monopropellant swirl injector.

In the most ideal case for a liquid monopropellant swirl injector, as shown schematically in Fig. 4, the flow generated by the tangential passages is assumed to be uniform.

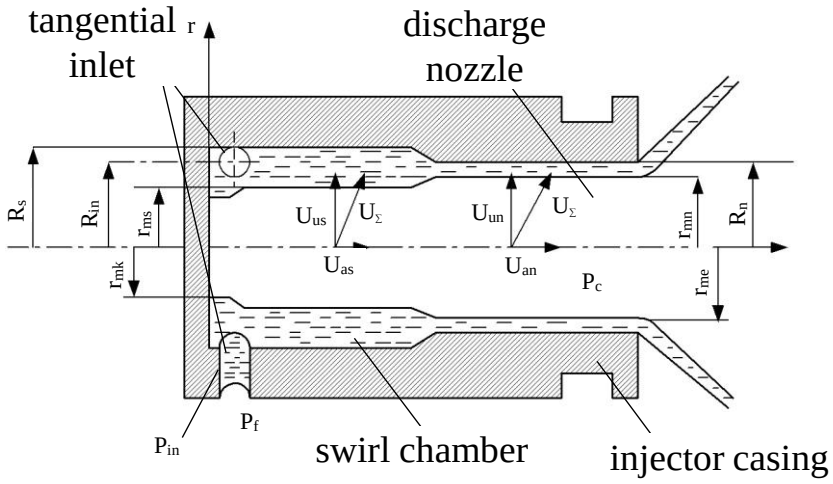

Figure 4. Schematic diagram of liquid flow along swirl injector.

The propellant enters the injector from the tangential passages and creates a swirling flow. At the outlet of the injector, the flow exits with mostly axial momentum and forms a conical sheet that atomizes downstream. At the injector exit, the ratio of the circumferential velocity and the axial velocity determines the spreading angle. In this ideal swirl injector, the internal surface pressure of the liquid vortex is equal to the combustion chamber pressure. The pressure drop through the injector converts the liquid potential energy into kinetic energy. The liquid flow velocity on the surface of the vortex chamber has the form:

$$U_\Sigma = \sqrt{\frac{2}{\rho}\Delta p_i} = \sqrt{U_u^2 + U_r^2 + U_{ax}^2} \tag{2.12}$$

where the subscripts u, r, and a represent the circumferential, radial, and axial components of velocity, respectively. The parameters for the swirl injector design can be related to each other through Bernoulli's equation, and conservation of mass, energy and angular momentum. Again, the mass flow rate is expressed as:

$$\dot{m} = \mu\rho A_n U_\Sigma = \mu A_n \sqrt{2\rho(p_f - p_{cc})} \tag{2.13}$$

Here μ is the mass flow coefficient to be defined later. At the tangential inlet, the velocity U_{in} can be found from

$$U_{\text{in}} = \sqrt{2(p_f - p_{in})/\rho} \tag{2.14}$$

Angular momentum is conserved, so the azimuthal velocity at various locations is:

$$U_{\text{in}} R_{\text{in}} = U_{uk} r_{mk} = U_{um} r_m = U_{rn} r_{mn} \tag{2.15}$$

The subscripts m, k, and in represent the ideal liquid vortex, the head end of the injector and the inlet, respectively. The total velocity equals the circumferential velocity because U_{ax} and U_r are zero at the liquid surface at the head end of the vortex chamber. As the radial velocity cannot be infinite, the liquid film radius is non-zero at any axial location, and there is a gas core present within the injector. A coefficient can be defined to represent the fraction of areas filled by the film in the nozzle:

$$\varphi = \frac{\pi(R_n^2 - r_{mn}^2)}{\pi R_n^2} = 1 - \frac{r_{mn}^2}{R_n^2} \tag{2.16}$$

where R_n is the radius of the nozzle and r_{mn} is the radius of the liquid film surface in the nozzle. In similar fashion, the non-dimensional parameter μ is defined for the relationship between the actual flow rate and the maximum possible flow rate through the nozzle. The mass flow rate coefficient μ can be described as the ratio of the actual mass flow rate to the maximum possible flow rate through the nozzle:

$$\mu = \frac{\rho U_{an} A_n \varphi}{\rho U_\Sigma A_n} = \frac{U_{an}\varphi}{U_\Sigma} \tag{2.17}$$

With the use of the conservation of angular momentum, the mass flow coefficient becomes:

$$\mu = \varphi \sqrt{\frac{U_\Sigma^2 - U_{un}^2}{U_\Sigma^2}} = \varphi \sqrt{1 - \frac{r_{mk}^2}{r_{mn}^2}} \tag{2.18}$$

The geometric parameters are used to form a non-dimensional geometric characteristic parameter A, defined by

$$A = \frac{A_n R_{in}}{A_{in} R_n} \tag{2.19}$$

where R_n is the nozzle radius, R_{in} the radial location of the center of the inlet passage, and A_{in} the total area of inlet passages. This non-dimensional parameter can be used as an indication of the swirl strength. As the radial location of the center of the inlet passage, or swirling arm, increases, the tangential inflow has a longer moment arm to swirl around, and the swirl strength increases. As the area of the inlet passages decreases with a constant mass flow rate, the inlet velocity increases, increasing the swirl strength. With this swirling

motion, an important result of the swirl injector dynamics is the formation of the hollow cone. This cone has a spreading angle, α, which the velocity components at the nozzle exit can determine:

$$\tan \alpha = \frac{U_{un}}{U_{an}} \tag{2.20}$$

Since there is one more variable than number of equations, an additional equation is required to close the formulation. This is found in the form of the principle of maximum flow. Introducing $\Delta p_t = p_f - p_{cc}$ for this derivation, the pressure and centrifugal forces on a liquid element of radius r with dr, length $rd\Phi$ and unit thickness are taken to be equal:

$$rd\Phi dp = dm\frac{U_u^2}{r} \tag{2.21}$$

where U_u is the circumferential velocity at radius r inside the liquid film and $dm = \rho r dr d\Phi$. Using the conservation of angular momentum, the foregoing relation may be integrated to yield:

$$p = \frac{\rho}{2}(U_{um}^2 - U_u^2) \tag{2.22}$$

Assuming the axial velocity is uniform and that it depends only on axial location, Bernoulli's equation can subsequently be used to solve for the axial velocity, U_a given the pressure:

$$U_{ax} = \sqrt{\frac{2\Delta p_t}{\rho} - U_{um}^2} \tag{2.23}$$

Again, the conservation of angular momentum is utilized to yield a relation for the circumferential velocity:

$$U_{um} = \frac{U_{in} R_{in}}{r_m} \tag{2.24}$$

The total volumetric flow rate can be described as the product of the inlet passage area and velocity U_{in}:

$$Q = n\pi r_{in}^2 U_{in} \tag{2.25}$$

where n is the number of tangential inlet passages and r_{in} the radius of tangential inlet passage. Substituting U_{um} from Eq. (2.24) into Eq. (2.23), and substituting the value of U_{in} from Eq. (2.25) yields the new relation for U_{ax}. This equation can then be related to the definition of passage fullness φ:

$$Q = \varphi(\pi R_n^2 U_a) \tag{2.26}$$

Bringing in the relations for the geometrical characteristic parameter A and the coefficient of passage fullness, the equation for volumetric flow rate becomes:

$$Q = \frac{1}{\sqrt{\frac{A^2}{1-\varphi} + \frac{1}{\varphi^2}}} \pi R_n^2 \sqrt{\frac{2\Delta p_t}{\rho}} \tag{2.27}$$

$\sqrt{2\Delta p_t/\rho}$ describes the total velocity, $\pi R_n^2 \sqrt{2\Delta p_t/\rho}$ is the total volumetric flow rate possible through the nozzle. Using the definition of the flow coefficient, the following relation for the mass flow coefficient can be rewritten as follows:

$$\mu = \frac{1}{\sqrt{\frac{A^2}{1-\varphi} + \frac{1}{\varphi^2}}} \tag{2.28}$$

The mass flow coefficient depends on the geometrical characteristic parameter and the coefficient of passage fullness. The effects these parameters have indicate the existence of an optimum maximum flow rate. For an increase in φ, the decrease in the axial velocity is faster than the increase in the equivalent flow area, leading to a decrease in mass flow rate. If φ is decreased, then the decrease in the equivalent flow area is faster than the increase in the axial velocity, leading to a decrease in mass flow rate. Combining these two trends, there exists a maximum flow rate. This is illustrated in Fig. 5. Applying the maximizing condition $d\mu/d\varphi = 0$ to Eq. (2.28) gives the relation between φ and A:

$$\frac{d\mu}{d\varphi} = -\frac{1}{2}\left(\frac{A^2}{1-\varphi} + \frac{1}{\varphi^2}\right)\left(\frac{A^2}{(1-\varphi)^2} - \frac{2}{\varphi^3}\right) = 0 \Rightarrow A^2 = \frac{2(1-\varphi)^2}{\varphi^3} \tag{2.29}$$

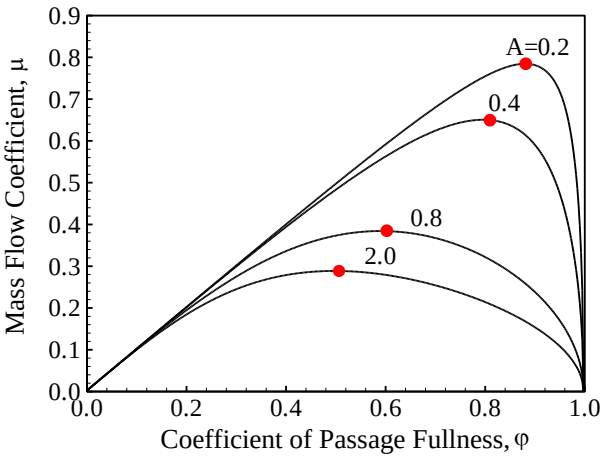

Figure 5. Existence of maximum flow rate.

Substitution of this into Eq. (2.28) gives the final equation required to close injector analysis:

$$\mu = \varphi \sqrt{\frac{\varphi}{2 - \varphi}} \tag{2.30}$$

Using the flow continuity condition, the liquid mass flow rates in the nozzle and tangential passages are equated:

$$U_{an} = \frac{\mu}{\varphi} U_{\Sigma} = \frac{\mu}{\varphi} \sqrt{\frac{2}{\rho}(p_f - p_{cc})} \tag{2.31}$$

Using the flow continuity condition, the liquid mass flow rates in the nozzle and tangential passages are equated:

$$\mu A_n \sqrt{2\rho(p_f - p_{cc})} = \mu_t n \pi r_{in}^2 \sqrt{2\rho(p_f - p_{in})} \tag{2.32}$$

The next step is to determine the azimuthal velocity U_{um} at some random point of the liquid vortex at the radius r_m. The subscript "m" represents the variables at the liquid surface. The use of the conservation of angular momentum yields

$$U_{um} = \frac{R_{in}}{r_m} U_{in} = \frac{r_{mk}}{r_m} U_{\Sigma} = \frac{R_{in}}{r_m} \sqrt{\frac{2}{\rho}(p_f - p_{in})} \tag{2.33}$$

where U_{Σ} is the idealized total liquid velocity. The use of Bernoulli's theorem to the cylindrical part of the nozzle passage yields

$$p_f = p_{cc} + \frac{\rho}{2}(U_{un}^2 + U_{an}^2) \tag{2.34}$$

Substituting in U_{un} and U_{an} from Eq. (2.31) and (2.33) into the above equation and rearranging results with

$$\frac{p_f - p_{in}}{p_f - p_{cc}} = \frac{\Delta p_{in}}{\Delta p_i} = \frac{1 - \mu^2/\varphi^2}{(R_{in}/r_{mn})^2} \tag{2.35}$$

The principle of maximum flow expression for μ and $r_{mn} = R_n\sqrt{1-\varphi}$ are used for substitution in the above equation to yield the ratio of the pressure drops across the tangential passage and the injector as a whole:

$$\frac{\Delta p_{in}}{\Delta p_i} = \frac{2(1-\varphi)^2/(2-\varphi)}{(R_{in}/R_n)^2} \tag{2.36}$$

The above equation is valid only for injectors having $R_{in}/R_n > 1$; otherwise, it may give a non-physical solution with $\Delta p_{in}/\Delta p_i$ >1. When the criterion is unmet, the principle of maximum flow does not hold for the injector. The injector parameters can now be expressed in terms of non-dimensional parameters by normalizing all the radii with respect to R_n and all velocities with respect to U_Σ. To simplify notation, all the normalized quantities are expressed with a bar over them. Substituting the axial velocity in the nozzle given by Eq. (2.31) into the $U_{un}^2 = U_\Sigma^2 - U_{an}^2$ yields

$$U_{un}^2 = U_\Sigma^2\left(1 - \frac{\mu^2}{\varphi^2}\right) \tag{2.37}$$

Substitution of $r_{mn} = R_n\sqrt{1-\varphi}$ and the above equation into the conservation of angular momentum, the radius of the liquid film at the head end becomes

$$r_{mk} = \frac{U_{un}r_{mn}}{U_\Sigma} = R_n\sqrt{1-\frac{\mu^2}{\varphi^2}}\sqrt{1-\varphi} \tag{2.38}$$

Substituting the mass flow coefficient into the above equation and then dividing both sides by R_n, the normalized radius of the liquid film yields

$$\bar{r}_{mk} = \sqrt{\frac{2(1-\varphi)^2}{2-\varphi}} = \sqrt{a} \tag{2.39}$$

The sole dependence of the injector flowfield upon the geometric characteristic parameter A makes it a convenient variable. The azimuthal velocities U_{un} and U_{ue} increase with A, whereas the axial velocities U_{an} and U_{ae} decrease with increasing A. The coefficient of passage fullness, φ, and the mass flow coefficient, μ, also show a decrease with an increase in A.

At the head end of the vortex chamber, $U_a = 0$ and the pressure ratio yields

$$\frac{\Delta p_{in}}{\Delta p_i} = \frac{U_{in}^2}{U_{uk}^2} = \left(\frac{r_{mk}}{R_{in}}\right)^2 = \frac{(r_{mk}/R_n)^2}{(R_{in}/R_n)^2} \tag{2.40}$$

The ratio of the liquid film radius at the head end to that in the nozzle becomes

$$\frac{\bar{r}_{mk}^2}{\bar{r}_{mn}^2} = \frac{a}{1-\varphi} = \frac{2(1-\varphi)}{2-\varphi} \tag{2.41}$$

In the non-dimensional form, $\bar{U}_\Sigma = 1$ and the use of the conservation of angular momentum yields the circumferential velocity in the nozzle:

$$\bar{U}_{un} = \frac{\bar{r}_{mk}}{\bar{r}_{mn}} = \sqrt{\frac{2(1-\varphi)}{2-\varphi}} \tag{2.42}$$

The axial velocity in the nozzle becomes:

$$\bar{U}_{an} = \sqrt{1-\bar{U}_{un}^2} = \sqrt{1-\frac{2(1-\varphi)}{2-\varphi}} = \sqrt{\frac{\varphi}{2-\varphi}} \tag{2.43}$$

Figure 6 shows the effects of the geometric characteristic parameter, A, on various commonly used parameters. The azimuthal velocities U_{un} and U_{ue} increase with A, while the axial velocities U_{an} and U_{ae} decrease with increasing A. The coefficient of passage fullness φ and the mass flow coefficient μ show a decrease with increasing A.

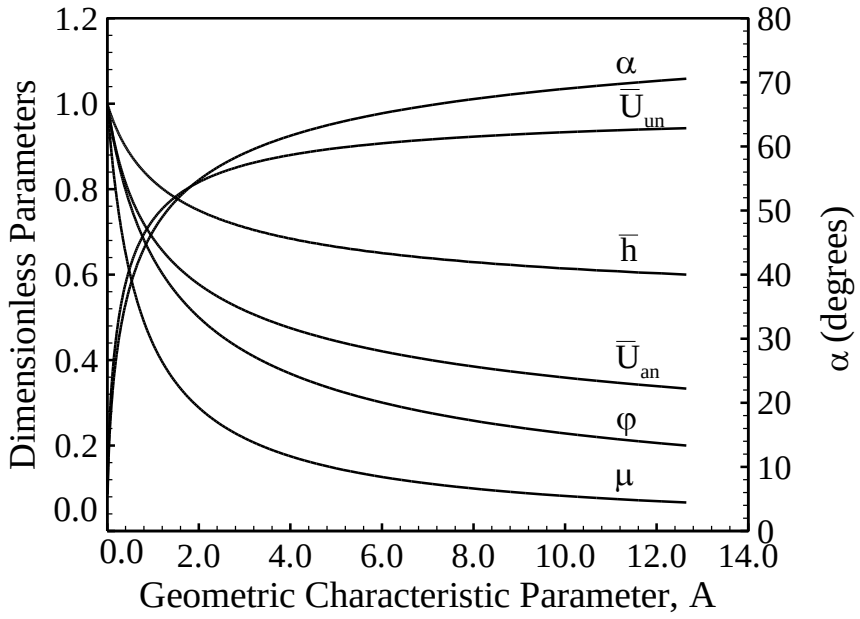

Figure 6. Effects of geometric characteristic parameter A on other injector design and flow parameters

The combination of Eqs. (2.42) and (2.43) determines the spreading angle of the liquid sheet at the injector exit using the ratio of the axial and circumferential velocities:

$$\alpha_n = \tan^{-1}\left(\frac{U_{un}}{U_{an}}\right) = \tan^{-1}\left(\frac{\bar{U}_{un}}{\bar{U}_{an}}\right) = \tan^{-1}\sqrt{\frac{2(1-\varphi)}{\varphi}} \tag{2.44}$$

Just downstream of the nozzle exit, the normalized circumferential velocity is

$$\bar{U}_{ue} = \frac{U_{ue}}{U_{\Sigma}} = \frac{r_{mk}}{R_n} = \bar{r}_{mk} = \sqrt{a} \tag{2.45}$$

and the normalized axial velocity is

$$\bar{U}_{ae} = \sqrt{1-a} \tag{2.46}$$

The spreading angle downstream of the nozzle exit is thus

$$\alpha_e = \tan^{-1}\sqrt{\frac{a}{1-a}} \tag{2.47}$$

The velocity in the tangential passage can be determined from the conservation of angular momentum in Eq. (2.15):

$$\bar{U}_{in}\bar{R}_{in} = \bar{r}_{mk} \tag{2.48}$$

With the expression of $\bar{r}_{mk}$ from Eq. (2.39) used in the above equation, the velocity in the tangential passage becomes:

$$\bar{U}_{in} = \frac{\sqrt{a}}{\bar{R}_{in}} \tag{2.49}$$

For application to a real swirl injector, viscous effects must be incorporated. The use of numerical calculations is required as no analytical solutions can be obtained in general. A hydraulic loss coefficient ξ_i, which represents the total pressure loss in the injector, and an angular momentum loss coefficient K are added to the formulation. The modified Bernoulli's equation is

$$p_f = p_{cc} + \frac{\rho U_{in}^2}{2} + \frac{\rho U_{an}^2}{2} + \xi_i \frac{\rho U_{in}^2}{2} \tag{2.50}$$

Therefore, the axial velocity becomes:

$$U_{an} = \sqrt{\frac{2}{\rho}\Delta p_i - \xi_i U_{in}^2 - U_{un}^2} \tag{2.51}$$

The Δp_i term represents the pressure drop across the injector. The mass flow rate through the injector nozzle can be presented in the following manner to characterize the realistic condition:

$$\dot{m}_i = \varphi \pi R_n^2 \rho U_{an} = \varphi \pi R_n^2 \sqrt{2\rho \Delta p_i - \xi_i \rho^2 U_{in}^2 - \rho^2 U_{un}^2} \tag{2.52}$$

where

$$U_{in} = \frac{\dot{m}_i}{n\pi r_{in}^2 \rho} \quad \text{and} \quad U_{un} = \frac{K R_{in} U_{in}}{r_{mn}} \tag{2.53}$$

and K is the angular momentum loss coefficient. The axial velocity has been assumed to be always uniform over any cross section. Introducing the definition of the geometrical characteristic parameter A and the coefficient of the nozzle opening $\bar{R}_{in} = R_{in}/R_n$, the equations above become

$$U_{in} = \frac{\dot{m}_i A}{\pi R_n^2 \rho \bar{R}_{in}} = \frac{\dot{m}_i A_n R_{in}}{\pi R_n^2 \rho \bar{R}_{in} A_{in} R_n} = \frac{\dot{m}_i}{n\pi r_{in}^2 D} \tag{2.54}$$

With the knowledge of Eq. (2.54) and

$$U_{un} = \frac{KR_{in}U_{in}}{r_{mn}} \quad \text{and} \quad r_{mn} = R_n\sqrt{1-\phi} \tag{2.55}$$

the following equations can be stated:

$$\begin{aligned} U_{in} &= \frac{\dot{m}_i A}{\pi R_n^2 \rho \bar{R}_{in}} \\ U_{un} &= \frac{K\dot{m}_i}{\rho\pi R_n^2\sqrt{1-\varphi}}A \end{aligned} \tag{2.56}$$

Equations (2.56) are substituted into Eq. (2.52) to solve for the definition of the flow characteristic parameter A that accounts for viscous losses:

$$\dot{m}_i = \mu_i \pi R_n^2 \sqrt{2\rho\Delta p_i} \tag{2.57}$$

where the mass flow coefficient μ_i takes the form

$$\mu_i = \frac{1}{\sqrt{\frac{1}{\varphi^2} + \frac{A^2K^2}{1-\varphi} + \xi_i \frac{A^2}{R_{in}^2}}} \tag{2.58}$$

The principle of maximum flow still holds and yields:

$$AK = \frac{\sqrt{2}(1-\varphi)}{\varphi\sqrt{\varphi}} \tag{2.59}$$

Plugging into the definition for mass flow coefficient along with the substitution of Eq. (2.57), the modified total velocity can then be obtained:

$$U_{\Sigma n} = \sqrt{1 - \xi_i \mu_i^2 \frac{A^2}{\bar{R}_{in}^2}} \sqrt{\frac{2}{\rho} \Delta p_i} \tag{2.60}$$

The ratio of the axial velocity to the total velocity determines the spreading angle in the following manner:

$$\sin \alpha = \frac{R_n}{r_{mn}} \mu_i A \frac{K}{\sqrt{1 - \xi_i \mu_i^2 A^2 / \bar{R}_{in}^2}} \tag{2.61}$$

Since $\sin \alpha$ can be approximated as just the inverse of r, the r_{mn} term can then be replaced by the average radius r_{av}, which is defined as

$$r_{av} = \frac{R_n + r_{mn}}{2} = \frac{R_n}{2} \left(1 + \sqrt{1 - \varphi}\right) \tag{2.62}$$

The spreading angle finally becomes

$$\alpha = \sin^{-1} \frac{2 \mu_i A K}{\left(1 + \sqrt{1 - \varphi}\right) \sqrt{1 - \xi_i \mu_i \, A^2 / \bar{R}_{in}^2}} \tag{2.63}$$

A few equivalent characteristic parameters are introduced that account for the viscous losses:

$$A_{\mathrm{eq}} \equiv AK = \frac{\sqrt{2}\left(1-\varphi_{\mathrm{eq}}\right)}{\varphi_{\mathrm{eq}}\sqrt{\varphi_{\mathrm{eq}}}}$$

$$\mu_{\mathrm{eq}} = \frac{\varphi_{\mathrm{eq}}\sqrt{\varphi_{\mathrm{eq}}}}{\sqrt{2-\varphi_{\mathrm{eq}}}} \tag{2.64}$$

The actual flow coefficient μ_i can be defined as follows:

$$\mu_i = \frac{\mu_{\mathrm{eq}}}{\sqrt{1+\frac{\xi_i \mu_{\mathrm{eq}}^2 A^2}{\bar{R}_{\mathrm{in}}^2}}} \tag{2.65}$$

By replacing A with A_{eq} in Fig. 6, the trends for the case of an ideal injector still hold for a real injector. The following equation can be used to determine A_{eq} for an open-type injector, where $R_{\mathrm{in}} = R_n$ and $A_{\mathrm{eq}} = A$.

$$A_{\mathrm{eq}} = \frac{R_{\mathrm{in}} R_n}{n r_{\mathrm{in}}^2 + \frac{\lambda}{2} R_{\mathrm{in}}\left(R_{\mathrm{in}} - R_n\right)}$$

$$\lambda = 0.3164/(Re_{\mathrm{in}})^{0.25} \tag{2.66}$$

is the friction coefficient and

$$Re_{\mathrm{in}} = \frac{U_{\mathrm{in}} r_{\mathrm{in}} 2\sqrt{n}}{\nu} = \frac{2\dot{m}_i}{\pi\sqrt{n} r_{\mathrm{in}} \rho \nu} \tag{2.67}$$

The majority of the losses are from the inlet ports. Thus the hydraulic loss coefficient can be approximated by

$$\xi_i = \xi_{\text{in}} + \lambda \frac{l_{\text{in}}}{d_{\text{in}}} \tag{2.68}$$

Typically during the design stage, the mass flow rate and pressure drop across the injector are predefined and the propellant properties are known. The actual flow coefficient and dimensions can be determined through the following design analysis.

1. The spray cone angle $2\alpha_n$ (twice the spreading angle) is first defined based off the injector operating conditions. Typical values of the spray cone angle lie between 90 and 120 degrees.
2. Once the spray cone angle is set, the geometric characteristic parameter A and flow coefficient μ can be determined from Fig. 6 or from Eqs. (2.44), (2.29), and (2.30).
3. The nozzle radius can be obtained from $R_n = 0.475\sqrt{\frac{\dot{m}_i}{\mu\sqrt{\rho\Delta p_i}}}$
4. The number of inlet ports and the inlet-port radial location R_{in} are specified based on structural considerations. The inlet-port radius r_{in} can be calculated by $r_{\text{in}} = \sqrt{\frac{R_{\text{in}}R_n}{nA}}$
5. The following injection element dimensions are defined:
    a. passage length of the inlet ports, $l_{\text{in}} = (3\sim6)r_{\text{in}}$
    b. nozzle length, $l_n = (0.5\sim2)R_n$
    c. vortex chamber length, $l_s > 2R_{\text{in}}$
    d. vortex chamber radius, $R_s = R_{\text{in}} + r_{\text{in}}$

6. The Reynolds number Re_{in} and friction coefficient λ can be determined using $Re_{\text{in}} = \frac{U_{\text{in}} r_{\text{in}} 2\sqrt{n}}{\nu} = \frac{2\dot{m}_i}{\pi\sqrt{n} r_{\text{in}} \rho \nu}$ and $\lambda = 0.3164/(Re_{\text{in}})^{0.25}$, respectively.
7. The equivalent geometric characteristic parameter A_{eq} is found from $A_{\text{eq}} = \frac{R_{\text{in}} R_n}{n r_{\text{in}}^2 + \frac{\lambda}{2} R_{\text{in}} (R_{\text{in}} - R_n)}$ and can be used to obtain μ_{eq} and α_{eq} from Fig. 6.
8. The tilting angle θ relative to the inlet plane can be computed from $\theta = 90 \text{ deg} - \tan^{-1} \frac{R_s}{l_{\text{in}}}$, Subsequently, the inlet hydraulic loss coefficient ξ_{in} is found by relation $\xi_{\text{in}} = -0.0067\theta + 1.1$. The hydraulic loss coefficient ξ_i across the injector can then be determined from $\xi_i = \xi_{\text{in}} + \lambda \frac{l_{\text{in}}}{d_{\text{in}}}$
9. The actual flow coefficient μ_i is obtained from $\mu_i = \frac{\mu_{\text{eq}}}{\sqrt{1 + \frac{\xi_i \mu_{\text{eq}}^2 A^2}{R_{\text{in}}^2}}}$
10. A new nozzle radius is defined based off the actual flow coefficient, $R_n^{(i)} = 0.475 \sqrt{\frac{\dot{m}_i}{\mu_i \sqrt{\rho \Delta p_i}}}$, Additionally, new geometric characteristic parameter is determined from $A^{(i)} = \frac{R_{\text{in}} R_n^{(i)}}{n r_{\text{in}}^2}$. Here, the superscript (i) denotes the iteration number.
11. Steps 1-10 are repeated until convergence with the use of $A^{(i)}$ in place of A to determine flow coefficient μ instead of the spray angle.

Another method of extracting the desired parameters is from trends obtained from model experiments. Correlations between the geometric characteristic parameter A and the spray cone angle $2\alpha_n$, flow coefficient μ_i, and normalized film radius $\bar{r}_m$ can be developed

from these experiments. This method is simpler than the previous method but is limited by the quantity of experimental data. Figure 7 shows some of the experimental correlations between the spray cone angle, flow rate coefficient, and relative liquid radius and the geometric characteristic parameter. The procedure for designing a swirl injection element from experimental data is as follows:

1. The spray cone angle 2α and normalized injector length $\bar{l}_n = l_n/D_n$ is set. The geometric characteristic parameter A is then found from Fig. 7a.
2. Using this value of A, the flow rate coefficient is determined from Fig. 7b
3. The nozzle radius R_n can be computed using $R_n = 0.475\sqrt{\frac{\dot{m}_i}{\mu\sqrt{\rho\Delta p_i}}}$.
4. The number of inlet ports n and radial location of the ports R_{in} are prescribed. Using these values, the inlet radius is calculated from $r_{\text{in}} = \sqrt{\frac{R_{\text{in}}R_n}{nA}}$.
5. The Reynolds number Re_{in} is found from Eq. (2.67). If $Re_{\text{in}} < 10^4$, step 4 should be repeated using different values of n and/or R_{in}.
6. The relative liquid radius $\bar{r}_m$ is determined from Fig. 7c and the absolute liquid radius can be found by multiplying $\bar{r}_m$ by R_n.
7. Other injector parameters (e.g., l_{in}, l_n, l_s, R_s, etc.) can be determined as needed.

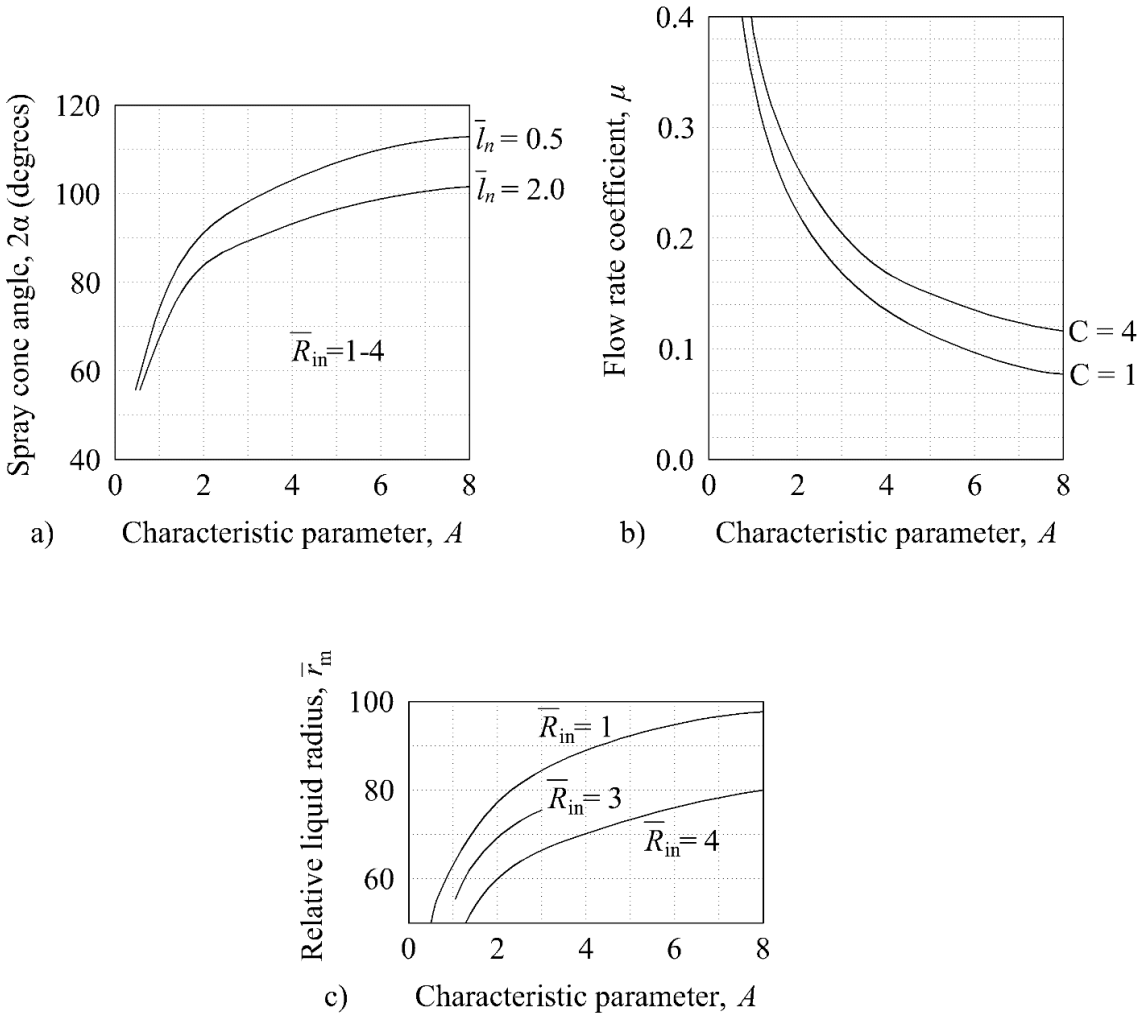

Figure 7. Experimental data of a) spreading angle, b) flow rate coefficient, and relative liquid radius as a function of geometric characteristic parameter *A* [10].

2.4 Linear Dynamics of Swirl Injectors

An injector may be considered as a dynamic system that experiences self-excited oscillations. Fluctuations in pressure, flow velocity, temperature and density are initially generated by the propellant feed or the combustion processes, then parameters indicative of the injector's performance (such as atomization, vaporization, and mixing) are adversely

affected by the oscillations. The swirl injector has a feedback mechanism between the flow rate and pressure fluctuation, between the tangential inlets and the nozzle exit. Variations of chamber pressure will cause pressure drop fluctuations across the tangential inlets, leading to fluctuations in flow rate at the nozzle exit. Any chamber pressure oscillations will affect velocity (or mass flow), film thickness, atomized particle size, and spreading angle. In addition, other properties, such as circumferential velocity, and pressure drop fluctuations in the liquid vortex will also vary due to pressure fluctuations across the injector. All these coupled effects will result in performance changes such as drop size distribution and spreading angle.

A response function can be derived which predicts the injector dynamics resulting from imposed or self-excited pressure and velocity oscillations [9]. It should be noted that the equations employed here are also valid for jet injectors. The general response can be summarized by these trends: the phase angle between the oscillations increases and the relative amplitude of the velocity oscillation decreases with increase in oscillation frequency, decrease in pressure drop across the injector, increase in liquid density, increase in tangential passage length, the extent of injector swirling arm, and decrease in geometric characteristic parameter. It is assumed the tangential passages are short compared to the wavelength of the disturbance in the liquid.

On the basis of the principle of maximum flow, a wave equation can be derived for the motion of the swirling liquid surface. For small disturbances, the equation is linear and the principle of superposition holds.

Assuming the perturbation of the pressure drop across the injector to be time harmonic, and assuming the fluid to be an ideal incompressible liquid,

$$\Delta\tilde{p} = \tilde{p}_f - \tilde{p}_k = \Delta p + |\Delta p'|e^{i\omega t} \tag{2.69}$$

where $|\Delta p'|$ represents the pressure oscillation amplitude. Integrating the one-dimensional Euler equation with respect to x from 0 to L_0 results in:

$$\frac{d\tilde{u}}{dt} + \frac{\tilde{u}^2}{2L_0} = \frac{\Delta p}{\rho L_0} + \frac{|\Delta p'|e^{i\omega t}}{\rho L_0} \tag{2.70}$$

Note that there is only one component of velocity, due to the assumption of one-dimensionality. With the assumption of small amplitude disturbances, Eq. (2.70) can be linearized as

$$\frac{du'}{dt} + \frac{uu'}{L_0} = \frac{\Delta p'}{\rho L_0} = \frac{|\Delta p'|e^{i\omega t}}{\rho L_0} \tag{2.71}$$

The solution to the above equation is

$$u' = \frac{\Delta p'}{\rho L_0}\frac{e^{i\omega t}}{\frac{u}{L_0} + i\omega} \tag{2.72}$$

With further algebraic manipulation, the ratio of the velocity disturbance to the disturbance of the pressure drop across the injector is obtained:

$$\frac{u'}{\Delta p'} = \frac{1}{\rho u}\frac{1-\frac{i\omega L_0}{u}}{1+\left(\frac{\omega L_0}{u}\right)^2} \tag{2.73}$$

The above expression can be rewritten as the ratio between dimensionless parameters and using the Bernoulli equation $\Delta p = \rho u^2/2$ we obtain a transfer function relation.

$$\Pi_j = \frac{u'/u}{\Delta p'/\Delta p} = \frac{1}{2}\frac{1-\frac{i\omega L_0}{u}}{1+\left(\frac{\omega L_0}{u}\right)^2} = \frac{1}{2}\frac{1-iSh_j}{1+Sh_j^2} \tag{2.74}$$

The Strouhal number of the injector is defined as $Sh_j \equiv \omega L_0/u$. For practical injector dimensions and the oscillation frequencies commonly found in ORSC engines, the injector can be considered as a simple inertia element in which the amplitude of the flow oscillation decreases smoothly as the Strouhal number increases, and the phase angle increases asymptotically towards $\pi/2$. In the case of long liquid injectors and coaxial gas-liquid injectors, resonance at multiple frequencies may occur when the injector length becomes comparable to the wave length of the perturbation. The influence of the injector length needs to be taken into consideration for cryogenic liquids because the speed of sound is relatively low as a result of the gas bubbles. The phase angle is defined as

$$\Phi_{in} = -\tan^{-1}\left(\frac{\omega L_{in}}{u_{in}}\right) \tag{2.75}$$

Furthermore, in real injectors one must account for viscous and compressibility effects, as well as the fact the injector walls are not ideal. The liquid viscosity results in boundary layer formation along the walls, causing spatially non-uniform velocity profiles.

However, the viscosity of fuels is usually small, allowing for these effects to be ignored to a first approximation. However, this changes when the length of the injector reaches a certain threshold as pointed out by the numerical study conducted by Nan Zong [12]. A primary effect of compressibility is the existence of propagating acoustic pressure waves, which have a finite velocity at a wavelength comparable to the injector length. For the most commonly used propellants, the wavelength of the pressure disturbances is more than two orders of magnitude larger than the injector length at frequencies up to several kilohertz, indicating that compressibility may be safely neglected. However, injectors operating under cavitation conditions are an exception. When the injector is filled with a two-phase liquid in which the speed of sound is below the original fluid's speed of sound, the above equations become invalid. The same can be said about superheated or highly compressible liquids that are discharged from the injector. Numerical calculations are required for corrections due to these issues.

In the case of a swirl injector, where the tangential inlets are relatively short relative to the wavelength, the relations derived for a jet injector remain valid. To further illustrate the behavior of the tangential inlet, the phase angle can be obtained from the real and imaginary parts of the transfer function obtained earlier. The result shows that the phase angle between the velocity oscillation and pressure drop oscillation increases, while the relative amplitude of the velocity oscillation decreases, with the following factors: increase in oscillation frequency, decrease of pressure drop across the injector, increase in liquid density, increase in tangential entry length and the extent of the injector swirling arm, and decrease of the geometric characteristic parameter. To develop an analytical model of the disturbance propagation, it is assumed that (1) the flow is inviscid, (2) the disturbance wave

amplitude is much smaller than the wavelength, (3) the axial component of velocity is uniform over any cross-section of the injector, and (4) there is no radial velocity component. The derivation begins with the conservation of angular momentum. For a strong swirl, the centrifugal force is balanced by the pressure gradient:

$$\frac{\partial p}{\partial r} = \rho \frac{u_u^2}{r} \tag{2.76}$$

Integrating from the liquid surface $r_m + \xi$ where $p = p_0$, the pressure at any arbitrary r is given by

$$p = p_0 + \int_{r_m+\xi}^{r} \rho \frac{u_{in}^2 R_{in}^2}{r^3} dr = p_0 - \frac{1}{2}\rho u_{in}^2 R_{in}^2 \left[\frac{1}{r^2} - \frac{1}{(r_m+\xi)^2}\right] \tag{2.77}$$

where ξ is a fluctuating liquid film thickness and r_m is the radial location of the liquid surface. Differentiating the above equation yields

$$\frac{\partial p}{\partial z} = -\rho u_{in}^2 R_{in}^2 \frac{1}{(r_m+\xi)^3}\frac{\partial \xi}{\partial z} \approx -\rho u_{in}^2 R_{in}^2 \frac{1}{r_{in}^3}\frac{\partial \xi}{\partial z} \tag{2.78}$$

The linearized momentum equation in the axial direction is

$$\frac{\partial u_a}{\partial t} = -\frac{1}{\rho}\frac{\partial p}{\partial z} \tag{2.79}$$

Substitution of Eq. (2.109) into (2.110) results in

$$\frac{\partial u_a}{\partial t} = u_{in}^2 R_{in}^2 \frac{1}{r_m^3}\frac{\partial \xi}{\partial z} \tag{2.80}$$

Now the conservation of mass for an annular liquid control volume of thickness dz may be expressed as

$$2\pi(r_m + \xi)dz\frac{\partial \xi}{\partial t}dt = -\frac{\partial}{\partial z}\{u_a \pi[R^2 - (r_m + \xi)^2\ ]\}dzdt \tag{2.81}$$

where R is the radius of the vortex chamber. Noting that

$$\left|2u_a r_m \frac{\partial \xi}{\partial z}\right| \ll \left|\frac{\partial u_a}{\partial z}[R^2 - r_m^2]\right|$$

Equation (2.112) can be simplified to yield

$$2r_m \frac{\partial \xi}{\partial t} = -\frac{\partial u_a}{\partial z}(R^2 - r_m^2) \tag{2.82}$$

Equations (2.111) and (2.113) are the two equations of interest. Differentiating both equations with respect to z and t, respectively, and eliminating common terms, produces the wave equation

$$\frac{\partial^2 \xi}{\partial t^2} = -\frac{1}{r_m^4} u_{in}^2 R_{in}^2 \left(\frac{R^2 - r_m^2}{2}\right)\frac{\partial^2 \xi}{\partial z^2} \tag{2.83}$$

This is analogous to Landau's equation for surface waves in a shallow pool. It may be expressed

$$\frac{\partial^2 \xi}{\partial t^2} = u_w^2 \frac{\partial^2 \xi}{\partial z^2} \tag{2.84}$$

where the wave velocity has been identified as

$$u_w = \sqrt{\frac{u_{in}^2 R_{in}^2 (R^2 - r_m^2)}{2 r_m^4}} \tag{2.85}$$

The first term within the radical represents the centrifugal acceleration on the liquid surface, while the second represents an effective thickness of the liquid film. For an axisymmetric rotating flow with a free interior, linearization of the equations of motion leads to a relationship between the fluctuations of the liquid surface and axial velocity:

$$\frac{\partial u_a{}'}{\partial t} = u_{in}^2 R_{in}^2 \frac{1}{r_m^3} \frac{\partial \xi}{\partial z} \tag{2.86}$$

With substitution and integration, the fluctuating axial velocity component on the liquid vortex free surface becomes:

$$|u_a{}'| = \frac{\Omega u_{in}^2 R_{in}^2}{u_w r_m^3} = \frac{\Omega u_\Sigma^2}{u_w r_m} \tag{2.87}$$

In accordance with the principle of maximum flow, the surface wave speed should be the same as the axial velocity of the liquid flow inside the injector nozzle, analogous to gas flow in a choked nozzle. Introducing the coefficient of passage fullness φ into Eq. (2.85) produces

$$\bar{u}_w = \frac{u_w}{u_\Sigma} = \sqrt{\frac{2(1-\varphi)^2}{(2-\varphi)}\frac{\varphi}{2(1-\varphi)^2}} = \sqrt{\frac{\varphi}{2-\varphi}} \tag{2.88}$$

The surface wave is advected by the mean liquid flow, and so the absolute velocity of a disturbance on the liquid surface with respect to the nozzle is the sum of the propagation velocity and the flow velocity. Next it is of interest to determine the amplitude of the liquid surface oscillation for a given oscillation amplitude within the tangential entry. The instantaneous volume flow rate through the swirling chamber is

$$Q_0 + Q' = 2\pi \int_{r_m+\xi}^{R} (u_a + u_a')rdr = 2\pi \int_{r_m+\xi}^{R} u_a rdr + 2\pi \int_{r_m+\xi}^{R} u_a' rdr \tag{2.89}$$

The right hand side can be integrated to yield

$$Q' = 2\pi u_a r_m \xi + \pi u_a'(R^2 - r_m^2) \tag{2.90}$$

The above equation illustrates how the oscillatory component of the volume flow rate arises from the oscillations of the open cross sectional area occupied by the liquid (the first term), and by oscillations of the liquid velocity axial component (the second term). Taking the magnitude of the foregoing expression and substituting $|u_a'|$ from Eq. (2.87) yields

$$|Q'| = \pi|u_a'|(R^2 - r_m^2) = \frac{\pi\Omega u_{in}^2 R_{in}^2 (R^2 - r_m^2)}{u_w r_m^3} = \frac{\pi\Omega u_\Sigma^2 r_m^2 (R^2 - r_m^2)}{u_w r_m^3} \tag{2.91}$$

With normalization by the axial velocity component at the head end and the radius of the liquid film, the oscillation of volume flow rate becomes:

$$|Q'| = \frac{\pi \bar{\Omega} u_{\Sigma}^2 R_n^2 (\bar{R}^2 - a)}{\bar{u}_w} \tag{2.92}$$

By continuity, the oscillatory flow rates in the vortex chamber bottom section and the input passages are equal. By equating the two and using the definition of the geometric characteristic parameter:

$$\bar{\Omega} = \frac{1}{A\sqrt{2(\bar{R}^2 - a)}} \left| \frac{u'_{in}}{u_{in}} \right| \tag{2.93}$$

For a vortex chamber of zero length, the surface wave amplitude can be determined by the acoustic conductivity of its nozzle:

$$\bar{\Omega}_0 = \frac{\bar{\Omega}\sqrt{\bar{R}_{in}^2 - a}}{2\sqrt{\varphi}} = \frac{\varphi \bar{R}_{in}}{4\sqrt{1-\varphi}} \frac{u'_{in}}{u_{in}} \tag{2.94}$$

An additional factor is wave propagation: the reflection coefficients at the head end and nozzle exit. The surface wave causes oscillation of the circumferential velocity in the radial direction due to conservation of angular momentum, which in turn gives rise to a centrifugal pressure gradient. For injectors in which dimensions are much smaller than the disturbance wavelengths in the gas and liquid, the pressure oscillations in the combustion chamber propagate through the liquid vortex layer essentially instantaneously. This causes fluctuations in the pressure drop across the tangential entry, which leads to oscillations in the liquid flow rate. The end result is that two traveling surface waves along the liquid surface are established and form a standing wave, as illustrated in Fig. 8. The reflection

coefficients can be used to determine the resonance properties of the liquid vortex, which affect the amplitude and phase angles of the pressure oscillations.

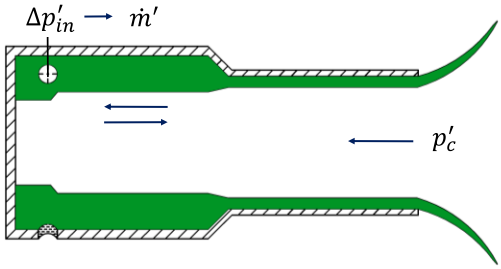

Figure 8. Injector dynamics schematic

Surface waves have a reflection coefficient defined by Π and the remaining surface waves travel through the nozzle which can be defined by $1 - \Pi$.

$$\Pi = \frac{\dot{m}'_s - \dot{m}'_n}{\dot{m}'_n} = 1 - \frac{\dot{m}'_n}{\dot{m}'_s} \tag{2.95}$$

The pressure drop oscillation across the injector results in some pressure drop oscillation across the tangential passage. This in turn produces oscillations in liquid flow rate, which are shifted in phase. Disturbances in circumferential velocity propagate along the liquid film and generate waves of vorticity in the adjacent gas. Use principle of superposition for influence of reflected waves within vortex chamber [32]:

$$\xi_s = \xi_1 \sum_{n=0}^{\infty} \Pi^n e^{i(\omega t-(2n)\phi_v)-(2n)v\phi_v}$$

$$\xi_n = \xi_1 \sum_{n=0}^{\infty} \Pi^n e^{i(\omega t-(2n+1)\phi_v)-(2n+1)v\phi_v} \tag{2.96}$$

The number of reflections, *n*, is chosen for when additions made less than 0.1% contribution to amplitude of existing wave. These two equations represent the response of the vortex chamber due to surface waves near the head end, $\Pi_{k,sw}$ and response of the vortex chamber near the nozzle, $\Pi_{sn,sw}$.

Furthermore, the oscillations include circumferential "vorticity" waves. These disturbances are the result of periodic fluctuation of circumferential velocity at different radial layers of the fluid:

$$\Pi_{s,vw} = \frac{\Delta p'_{s,vw}}{2u'_{in}} = \int_0^1 \frac{e^{i\left\{\omega t - \frac{\omega R_{in} R_v^2 - a}{u_\Sigma \quad v} \bar{x}\, tan\left(\frac{\pi \bar{x}}{2}\right)\right\}}}{\left[1 - \left(R_v - \sqrt{a}\right)\frac{\bar{x}}{R_v}\right]^3} d\bar{x} \tag{2.97}$$

There is a factor of 2, while defining the response due to vorticity waves as it is assumed that the pressure drop in the vortex chamber is shared equally by both the surface waves and vorticity waves.

Finally, the surface waves travel through the nozzle with minimal losses as it is assumed to be short. The liquid thickness is considered constant, so any effect due to vorticity waves is negligible. There is only phase shift in the surface waves for a given nozzle length, having a response:

$$\Pi_n = \frac{\dot{m}'_n}{\dot{m}'_{sn}} = (1 - \Pi) e^{-i\phi_n} \tag{2.98}$$

The oscillation amplitude and phase shift of the wave patterns can be determined in principle by solving the Navier-Stokes equations written for circumferentially

symmetric motion. Auxiliary quantities, such as the nozzle impedance, may be extracted from the results. The system can be solved using a Laplace transform with respect to time, which converts the governing set of partial differential equations to a set of ordinary differential equations. Static pressure pulsation causes pressure oscillations across the inlet which induces a mass flow rate fluctuation and velocity fluctuation:

$$u_{in} = \Pi_{in} \Delta p_{in} \tag{2.99}$$

With the remaining pressure drop where it is shared equally among surface waves and vorticity waves:

$$\begin{aligned} \Delta p'_{k,sw} &= 2u'_{in} \Pi_{k,sw} \\ \Delta p'_{s,vw} &= 2u'_{in} \Pi_{s,sw} \end{aligned} \tag{2.100}$$

Total pressure drop can be summed up as

$$\Delta p = \Delta p_{in} + \Delta p_{s,sw} + \Delta p_{s,vw} \tag{2.101}$$

Substituting the transfer functions into the above pressure drop equation

$$\begin{aligned} \Delta p &= \Delta p_{in} \left(1 + 2\Pi_{in} \left(\Pi_{k,sw} + \Pi_{s,vw}\right)\right) \\ \Delta p'_{in} / \Delta p &= \Delta p' / \Delta p / \left(1 + 2\Pi_{in} \left(\Pi_{k,sw} + \Pi_{s,vw}\right)\right) \end{aligned} \tag{2.102}$$

The pressure drop across the tangential inlet can be approximated as

$$\Delta p_{in} = \Delta p \; a/R_v^2 \tag{2.103}$$

The equation then becomes

$$\frac{\Delta p'_{in}}{\Delta p_{in}} = \frac{R_v^2}{a} \frac{\frac{\Delta p'}{\Delta p}}{\left(1 + 2\Pi_{in}\left(\Pi_{k,sw} + \Pi_{s,vw}\right)\right)} \tag{2.104}$$

Mass flow rate can then be included

$$\dot{m}'_{in} = \Pi_{in} \Delta p_{in}$$

$$\frac{\dot{m}'_{in}}{\dot{m}_{in}} = \frac{R_v^2}{a} \frac{\Pi_{in} \frac{\Delta p'}{\Delta p}}{\left(1 + 2\Pi_{in}\left(\Pi_{k,sw} + \Pi_{s,vw}\right)\right)} \tag{2.105}$$

There is also the relationship

$$\frac{\dot{m}'_{in}}{\dot{m}_{in}} = \Pi_{in} \frac{\Delta p'}{\Delta p} \tag{2.106}$$

For the pulsating flow near the nozzle, the response can be written as

$$\frac{\dot{m}'_{sn}}{\dot{m}_{sn}} = \Pi_{sn,sw} \frac{\dot{m}'_{in}}{\dot{m}_{in}} \tag{2.107}$$

The mass flow rate through the tangential inlet, vortex chamber, and nozzle is conserved, so substitutions can be made and the response function of the injector may be expressed using normalized parameters

$$\Pi_{inj} = \frac{\frac{Q'_{inj}}{Q_{inj}}}{\frac{\Delta p'_{inj}}{\Delta p_{inj}}} = \frac{\bar{R}_{in}^2}{a} \frac{\Pi_{in}\Pi_n\Pi_{sn,sw}}{2\Pi_{in}(\Pi_{k,sw} + \Pi_{s,vw}) + 1} \tag{2.108}$$

Here the transfer functions are denoted by subscripts in, k, s, and n which represent the tangential inlet, head end, vortex chamber, and nozzle respectively, and $\bar{R}_{in} = r_{in}/R_n$.

In order to determine the dynamics, the auxiliary quantities previously mentioned must be calculated using the dimensions of the injector:

$$a = \frac{2(1-\varphi)^2}{2-\varphi}; b = \frac{2(1-\varphi)}{2-\varphi}$$
$$\mu = \frac{\varphi\sqrt{\varphi}}{\sqrt{2-\varphi}}; A = \frac{(1-\varphi)\sqrt{2}}{\phi\sqrt{\varphi}} \tag{2.109}$$

Then, the velocity of the disturbance propagation within the swirl chamber and nozzle can be calculated using

$$v_s = \omega_\Sigma \left[\sqrt{\bar{R}_k^2 - a} + \frac{\mu}{\bar{R}_k^2 - a}\right]$$
$$v_n = \omega_\Sigma * 2\sqrt{\frac{\varphi}{2-\varphi}} \tag{2.110}$$

where the injector "closing" degree is defined as $\bar{R}_k = R_k/R_n$. The phase angle for the tangential passage is determined from

$$\Phi_{in} = -\tan^{-1}\left(\frac{\omega L_{in}}{u_{in}}\right) \tag{2.111}$$

The phase angle for the swirl chamber, ignoring reflected waves, is defined as:

$$\Phi_k = -\frac{\omega L_k}{v_{s,k}} \tag{2.112}$$

And the phase angle for the nozzle is determined from:

$$\Phi_n = -\frac{\omega L_n}{v_n} \tag{2.113}$$

The dimensionless amplitude of liquid surface oscillation in an infinitely long swirl chamber is determined by:

$$K_{\Sigma II} = \left(\frac{\Omega}{r_m}\right) = \frac{1}{A\bar{R}_k\sqrt{2}} \tag{2.114}$$

The coefficient of wave reflection from the nozzle is determined from

$$\Pi = 1 - \frac{2\sqrt{\varphi}}{\sqrt{\bar{R}_k^2 - a}} \tag{2.115}$$

The Strouhal number for the tangential inlet is

$$Sh_{in} = \frac{\omega L_{in}}{u_{in}}, u_{in} = \sqrt{\frac{2\Delta p_{inj} a}{\rho \bar{R}_k^2}} \tag{2.116}$$

For the overall response of the tangential inlet, the following transfer function may be derived:

$$\Pi_{in} = \frac{1}{2}\frac{1 - \frac{i\omega L_{in}}{u_{in}}}{1 + \left(\frac{\omega L_{in}}{u_{in}}\right)^2} \tag{2.117}$$

which can be further split into its real and imaginary components

$$\mathrm{Re}\{\Pi_{in}\} = \frac{1}{2(1 + Sh_{in}^2)}, \qquad \mathrm{Im}\{\Pi_{in}\} = -\frac{Sh_{in}}{2(1 + Sh_{in}^2)} \tag{2.118}$$

Likewise, for the nozzle, it may be shown that

$$\Pi_n = (1 - \Pi)e^{i\omega L_n/v_n} \tag{2.119}$$

Separating the surface wave transfer function into real and imaginary components gives

$$\begin{aligned} \mathrm{Re}\{\Pi_{sn,sw}\} &= K_{\Sigma II}^* e^{-\frac{i\Phi_k}{2\pi}} \cos\Phi_k \\ \mathrm{Im}\{\Pi_{sn,sw}\} &= -K_{\Sigma II}^* e^{-i\Phi_k/2\pi} \sin\Phi_k \end{aligned} \tag{2.120}$$

The transfer function for the bottom section of the vortex chamber is also split into its real and imaginary components:

$$\mathrm{Re}\{\Pi_{k,sw}\} = K_{\Sigma II}^*, \quad \mathrm{Im}\{\Pi_{k,sw}\} = 0 \tag{2.121}$$

$$K_{\Sigma II}^{*} = K_{\Sigma II}\frac{\sqrt{(\bar{R}_k^2 - a)^3}}{\mu\sqrt{2a} + \sqrt{(\bar{R}_k^2 - a)^3}} = \frac{(\bar{R}_k^2 - a)}{A\sqrt{2}\left(\mu\sqrt{2a} + \sqrt{(\bar{R}_k^2 - a)^3}\right)} \tag{2.122}$$

and

$$\begin{aligned}
\mathrm{Re}\{\Pi_{s,vw}\} &= \frac{\bar{R}_k - a}{\bar{R}_k}\int_0^1 \cos f(\bar{x}) e^{-vf(\bar{x})}\frac{d\bar{x}}{\left(1 - \frac{\bar{R}_k - a}{\bar{R}_k}\bar{x}\right)^3} \\
\mathrm{Im}\{\Pi_{s,vw}\} &= \frac{\bar{R}_k - a}{\bar{R}_k}\int_0^1 \sin f(\bar{x}) e^{-vf(\bar{x})}\frac{d\bar{x}}{\left(1 - \frac{\bar{R}_k - a}{\bar{R}_k}\bar{x}\right)^3}
\end{aligned} \tag{2.123}$$

where the intermediate variables are

$$f(\bar{x}) = \frac{\omega R_{in}}{u_\Sigma}\,\frac{\bar{R}_k^2 - a}{\mu}\,\frac{\bar{R}_k(1-\bar{r})}{\bar{R}_k - \sqrt{a}}\tan\left(\frac{\pi\bar{R}_k(1-\bar{r})}{2(\bar{R}_k - \sqrt{a}}\right) \tag{2.124}$$

The effects of axial velocity in the vortex chamber are embedded into the second model of interaction between the tangential inlet and the vortex chamber, in which $K_{\Sigma II}^{*}$ incorporates the axial velocity effect in the vortex while $K_{\Sigma II}$ neglects it. These transfer coefficients make use of the previous results for the surface wave amplitude. For a long vortex chamber:

$$K_{\Sigma II} = \left(\frac{\Omega}{r_{mk}}\right) = \frac{1}{A\sqrt{2(\bar{R}_k - a)}} \tag{2.125}$$

$$K_{\Sigma II}^{*} = \left(\frac{\Omega^{*}}{r_{mk}}\right) = \bar{\Omega}\frac{\sqrt{(\bar{R}_k^2 - a)^3}}{\mu\sqrt{2a} + \sqrt{(\bar{R}_k^2 - a)^3}} = \frac{\bar{R}_k^2 - a}{A\sqrt{2}\left(\mu\sqrt{2a} + \sqrt{(\bar{R}_k^2 - a)^3}\right)} \tag{2.126}$$

By combining the transfer functions of different parts of the swirl injection element, the overall transfer function can be obtained. The transfer function of the tangential inlet, Eq. (2.117), along with the transfer function of direct and centrifugal pressure-drop fluctuations in the vortex chamber caused by the fluctuating inlet velocity, Eq. (2.121) and (2.123), can be rearranged and substituted into the total fluctuating pressure-drop across the entire injector to finally yield Eq. (2.108):

$$\Pi_{inj} = \frac{\frac{Q'_{inj}}{Q_{inj}}}{\frac{\Delta p'_{inj}}{\Delta p_{inj}}} = \frac{\Delta p_{inj}}{\Delta p_{in}} \frac{\Pi_{in}\Pi_n\Pi_s}{2\Pi_{in}\Pi_s + 1}$$

The magnitude of the response for the transfer function typically resembles Fig. 9 which corresponds to the LOx side of the RD-0110 injector. This is the information that can be used to tune the length of the injector.

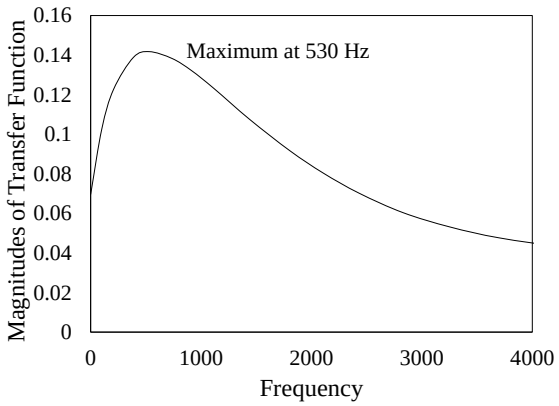

Figure 9. Magnitude of transfer function response for LOx side of RD-0110

This classical swirl injector theory has been verified numerically for the frequency range of interest. For higher frequencies outside this range, the surface and vorticity wave

treatment can be modified slightly for better results. Some questions with the classical treatment include the assumption of the radii of the vortex chamber and the film, wave speed based on infinitesimal disturbance propagation, sudden change of film thickness as the vortex chamber transitions to nozzle, and the inclusion of an artificial viscosity term even though the analysis is based on inviscid flow. Some studies have been done to verify the results of this formulation. The results show that up to a certain frequency, the analysis holds up well compared to numerical studies conducted for injector dynamics [33, 34].

There are several effects on injector dynamics that need to be considered for design. A geometric characteristic *A* increase causes a slight increase in the relative amplitude of flow rate oscillation in the tangential passage, decrease in the oscillation amplitude of flow rate and liquid surface in the vortex chamber and the nozzle channel [35]. With *A* increase the phase angle in the tangential passage increases slightly while phase angles in the vortex chamber and the nozzle channel increase substantially. Oscillation frequency rise leads to an increase in the phase angle and a decrease in oscillation amplitude of all parameters in all parts of the swirl injector except resonant frequencies of the vortex chamber, as angular momentum (consisting of surface and vorticity waves) needs to be conserved while accounting for the lower kinetic energy of the liquid jet displacing the liquid film. Average pressure drop increase and liquid density decrease lead to an increase in the relative amplitude of flow rate oscillation in the tangential passage and decrease in phase angles in all parts of the swirl injector.

Since the mechanisms of disturbance transfer from the combustion chamber to the feed system and from the feed system to the combustion chamber are different, the same factors exert different effects on damping and amplification of oscillations of pressure and

flow rate in various parts of the feed system and inside injector. Thus reflected waves in the vortex chamber are insignificant for the pressure disturbance passing from the combustion chamber to the feed system.

Swirl injectors have higher admittance for disturbance passing to the feed system compared to jet injectors. Swirl injectors can even amplify pressure oscillations due to integrating action of the liquid vortex, which uses a part of its kinetic energy for this. Therefore to reduce pressure oscillations in the manifold, "open" injectors and devices for oscillation damping or filtration should be used.

Other than the case when pressure oscillations trigger liquid flow rate disturbances, vortex chamber resonant properties are also essential and those properties can be used for flow rate waves damping. Flow rate disturbances propagate through the injector with a much lower velocity than pressure disturbances propagate through the feeding line. The velocity of disturbance propagation through the injector can be varied in a wide range by changing its design within commonly adopted geometry. All this provides a possibility to vary injector amplitude and phase characteristics without changing radically parameters of their stationary operation.

To affect oscillation damping through their viscous decay, it is necessary to increase the time of liquid residence in the injector, the surface area, over which the liquid flows, and liquid flow velocity. At specified operating parameters these conditions can be met with using long jet injectors or swirl injectors with long vortex chambers and nozzles and having large values of geometric characteristic and vortex chambers of large volume. The chief drawback of using viscous forces for pressure oscillation damping consists in their

simultaneous effect on injector mean parameters (spray cone angle, atomization degree, film thickness and so on). In any case if there is necessary to obtain intensive oscillation of liquid flow rate at the injector outlet, viscous losses should be reduced, wherever possible.

The amplitude of flow rate oscillation and the coefficient of oscillation transfer from the chamber to the feed system can be reduced by increasing liquid inertia forces. This is affected by using long jet injectors or swirl injectors with tangential passages extended to 40 diameters in length and with nozzles of a small "closing" extent.

It should be noted that neither viscous damping nor inertial forces can provide complete elimination of flow rate oscillations, especially at low frequencies. This can be achieved with injectors-filters, which include a resonator adjusted to a certain frequency (a vortex chamber in most cases) or two independent mechanisms of flow rate oscillation transfer, which are opposite in phase and have identical amplitude characteristics. Flow rate oscillations can be eliminated, among other ways, by using two-channel injectors and positioning the planes of liquid feed in such a way that flow rate waves, which arise in the vortex chamber, may have oscillations of equal amplitude and opposite phases at the nozzle inlet. Variation in design parameters causes variation of several dynamic parameters which affect flow rate oscillation in different ways. The effects of injector part design changing on injector dynamic characteristics are described below. The summarized data are based on theoretical analysis and experimental results.

1. Tangential passages length, increased up to 10-12 diameters reduces the amplitude of flow rate oscillation by a factor of 2-4 at ≈ 1000 Hz; this effect is stronger as oscillation frequency rises. The phase shift angle ψ_ϕ between the

flow rate oscillation and pressure drop oscillation increases only slightly. To make injectors more compact, it is appropriate to use extended passages of screw shape.

2. Injector geometric characteristics *A* increase results in liquid flow rate oscillation decrease due to decrease in the amplitude of liquid vortex surface oscillation in the vortex chamber.
3. The increase in the injector "closing" extent substantially increases flow rate oscillation amplitude.
4. Extension of injector nozzle substantially increases the phase angle ψ_ϕ and has no or little effect on oscillation amplitude.
5. The vortex chamber extension of "closed" injectors at first reduces sharply the amplitude of flow rate oscillation and increases the phase angle; at further chamber extension the variation of ψ_ϕ becomes slower while the amplitude of flow rate oscillation may somewhat increase.

Thus to damp pressure oscillation, "open" swirl injectors with a high geometric characteristic and extended tangential passages and vortex chamber should be used. To provide flow rate strong oscillation at nozzle exit, "closed" injectors with shortest possible vortex chamber and tangential passages should be used. Geometric characteristic A should be moderate. Nozzle and vortex chamber lengths, as well as injector "closing" extent, are most suitable design parameters that can used for controlling the phase angle between pressure oscillations and flow rate oscillations.

It has been shown that positioning of an additional row of tangential passage in the vortex chamber could prevent generation of flow rate oscillations under the effect of pressure drop oscillations [36]. In this case flow rate oscillations in the vortex chamber, which occur at flow velocity oscillations in each row, affect liquid discharge from another row of passages. However since the amplitude of oscillations of pressure onto vortex chamber wall is small compared to pressure drop oscillations and liquid flow rate oscillations, it can be approximately assumed that liquid surface perturbations from each passage row exist independently from each other and their vector addition is possible.

While designing injectors for damping flow rate high-frequency (f >600 Hz) oscillations, waves of swirl that propagate axially can be neglected because of their fast decay. In the low-frequency region the waves of swirl and their interaction with surface waves can be a new factor of flow rate oscillations possible damping or amplifying since those oscillations move from the row of tangential passages to injector nozzle by two different mechanisms which have substantially different response functions.

2.5 Main Combustion Chamber Injector Design

Gas centered liquid swirl injectors such as that of the ORSC MCC injectors have a different behavior because the hot gaseous oxygen (GOx) from the preburner is injected axially down the gas post. The fuel is injected tangentially behind a collar, which acts as a heat shield, to allow the liquid film to develop. The dynamics of the axial gaseous flow and of the liquid swirl injector must be characterized as separate processes. The transfer function of the liquid swirl injector is treated in the same manner as a monopropellant swirl injector.

As the GOx enters the recessed chamber, it comes into contact with the liquid film developing in the swirler. The shield should be filled by the liquid fuel to ensure a thermal barrier between the combustion zone and the injector wall and this is accomplished when the fuel annulus width is on the order of the tangential inlet diameter, accommodating conservation of mass. The dynamics of this liquid swirl injector in this confined region can be described by classical swirl dynamics theory, and are based on capturing the surface wave propagation. The filled annular region aligns the gas-liquid interface with itself. From a mathematical standpoint, this does not change the integration limits in previous analytical model. The derivation is based on the wave equation, which takes into account the disturbance propagation in the liquid with centrifugal force, and the controlling physics is still the balance between the radial pressure gradient and the centrifugal force, which is unaffected by the confinement due to the shield.

The momentum ratio between the gas phase at the liquid phase plays a pivotal role in determining the length of the film as the high velocity gaseous flow filaments and atomizes the swirling liquid film. This ratio is defined as:

$$MR = \frac{\rho_g u_g^2}{\rho_f u_{f,ax}^2} \tag{2.127}$$

where the $u_{f,ax}$ is the axial velocity component for the liquid propellant. As this ratio increases, the liquid film length decreases, with increased entrainment and stripping of the liquid film by the gaseous flow.

In terms of operating conditions, the momentum ratio, the temperature, and the density and viscosity of the propellants all have a significant impact upon injector

dynamics. The velocity ratios determine whether or not wave disturbances on the liquid surface, known as Kelvin-Helmholtz instabilities, will appear. These instabilities give rise to vortex formation, which promotes mixing and atomization. As previously mentioned, large momentum ratios indicate stronger gaseous entrainment and stripping. The intact liquid length of decreases as the momentum ratio increases and swirl strength decreases, displaying a power law dependency between the intact liquid length and the dynamic pressure ratio [37]. Similarly, higher temperatures decrease the density and increase velocities for a fixed mass flow rate, leading to higher momentum ratios, which create larger vortices for enhanced mixing. In addition, viscosity plays two roles: thickening the liquid film by increasing the shear stress, and resisting the disintegration of the sheet into droplets by delaying liquid film break up. For gas-centered liquid-swirl coaxial (GCLSC) injectors, performance and stability are often at odds. For example, higher momentum ratios allow for the gas phase to resist disturbances from the liquid phase, but the stronger entrainment reduces the liquid film spreading angle and hinders inter-element mixing conducive to combustion. This design trade-off is addressed in the last step of the proposed design methodology requiring a certain momentum ratio by adjusting the fuel annulus width, using the momentum ratio of the RD-170 engine injectors as a reference.

The shield length is typically long enough to ensure the swirling fuel is full developed, while taking into account for the recess with respect to the taper bore. The recess length not only controls the interaction between the gaseous oxidizer and the swirling liquid film, but also serves as an anchor point for the flame [38]. The post tip provides a physical location for the flame to stabilize due to the established recirculation zone. As a rule of thumb, the recess length is on the order of the integral length scale of the

vortices, which would be on the order of the nozzle radius. An alternative is simply using knowledge of the propellant autoignition delay as the residence time required. The post thickness also has a minimum thickness. If the post were a sharp thin edge instead of a blunt surface, the Kutta condition would mandate that there be stagnation point on the post, which leads to poor thermal loading. On the other hand, if the thickness were too thick, the vortex shedding frequency decreases and may cause low frequency instabilities.

In addition to hydrodynamic theory, acoustics can be used to determine the optimal orifice diameter and injector length. The orifice discharge coefficient, $C_{d,or}$, can range approximately from 0.60 – 0.70, assuming a sharp-edged inlet to the orifice. $C_{d,or}$ can increase more if the orifice inlet radius is increased; offering a reduced static pressure drop if needed. Choked flow relations gives the maximum flow achievable through the orifice given mass flow rate, assuming the flow remains subsonic as it passes through the orifice. For initial sizing calculations, the orifice should be assumed sharp so that $C_{d,or}$= 0.61.

$$\dot{m}_{g,choke} = C_{d,g} A_{in,g} \frac{P_g}{\sqrt{T_g}} \sqrt{\frac{\gamma_g}{R_g} \left(\frac{2}{\gamma_g + 1} \right)^{\frac{\gamma_g + 1}{\gamma_g - 1}}} \tag{2.128}$$

$$\dot{m}_g = C_{d,g} \left(\frac{\pi}{4} d_{in,g}^2 \right) \sqrt{2 \rho_g P_g \left(\frac{\gamma_g}{\gamma_g - 1} \right) \left[\left(\frac{P_{g,in}}{P_g} \right)^{\frac{2}{\gamma_g}} - \left(\frac{P_{g,in}}{P_g} \right)^{\frac{\gamma_g + 1}{\gamma_g}} \right]} \tag{2.129}$$

Using the propellant properties and operating conditions, the diameter of the gaseous post can be determined using the equations in the previous section. A geometry change causes

reflection and transmission of acoustic waves, which is further exacerbated by vortex shedding from the sudden expansion downstream of the GOx inlet orifice.

When the acoustic frequency that requires damping is known, the injectors should be tuned treated as a half-wave or quarter-wave resonators depending on boundary conditions. Since there is no distinct interface between the injected propellant and the gaseous core in a supercritical [39], the proper wave speed selected for the analysis needs to be carefully considered. For optimal damping of the acoustic energy, the area ratio between the inlet orifice and the post diameter should be about one half [15]. Moreover, the gaseous post can be treated as a half wave resonator to damp out the acoustic energy of the second tangential mode, the length can be calculated using the characteristic velocity of the incoming hot gas and the corresponding resonance frequency of the second tangential mode. The first tangential mode is tuned by the baffle injectors, verified by an eigenmode analysis that treats the baffle injectors with open-open boundary conditions. This decision was probably made by Russian designers to ensure a stability margin. This also reaffirms the existence of a limit cycle for transverse acoustics that becomes a design constraint. The necessary and sufficient condition for the existence of a limit cycle for two modes, one acoustic mode is linearly unstable, while the other mode is linearly stable [40]. Energy is supplied from the unstable mode and dissipated by the stable mode. The nonlinear coupling causes this transfer of energy and in this case, the stable mode is the second tangential mode of the combustion chamber which the main injectors are tuned to damp out. Although it has been stated that the coupling between the first tangential mode and the first radial mode is stronger, the second tangential mode can be treated as the target

because both modes oscillate at the same frequency, when three modes are considered for a limit cycle.

Simplifying the combustion chamber as a cylinder, the acoustic resonance frequencies can be estimated using Bessel functions with the speed of sound [41]. The injector length can be sized according to the target acoustic mode of interest. Although ensuring the injector is long enough to allow for flow reattachment, this length is usually much shorter than the length needed for injector tuning to mitigate combustion instabilities. An example would be treating the injector as a half-wave resonator tuned to the second tangential mode of the combustion chamber. The length can be calculated with Eq. (2.130) where R_c is the radius of the combustion chamber and $\alpha_{12} = 3.054$ is the second tangential mode eigenvalue:

$$L = \frac{\pi R_c}{\alpha_{12}} \tag{2.130}$$

For the unbaffled RD-170 chamber, the first tangential mode is 1980Hz. Further exploration through an eigenmode analysis shows that the damping constant of the second tangential mode of the MCC assembly is lower than that of the first tangential mode, and the scenario is reversed when mean flow is introduced. Vortex shedding, from the flow distributor and injector orifice, contributes to the acoustic damping of the first tangential mode. Another design consideration is the combustion zone, as having the combustion region reaching further downstream would increase the stability margin. One interesting note is that the 1L injector mode at 40% power is tuned for the 1T chamber mode, which does not vary significantly with pressure.

One of the most significant parameters is the chamber pressure. The chamber back pressure significantly affects the dynamics of the injector, especially because ideal operation of the engine dictates that the propellants reach supercritical conditions. At supercritical pressures, there is no longer a meaningful distinction between liquid and gas phases, such that phase changes do not occur. Thus the controlling physics of atomization and combustion are different under supercritical conditions. Increasing the chamber pressure has also been shown to lower the injector pressure drop. A decrease in pressure drop results in an increase in the discharge coefficient at a constant mass flow rate, implying an increase of the liquid film thickness. The increase in liquid film thickness can also be explained by the increased viscous stresses on the gas-liquid interface, resulting from the increased shear of the gas core due to the pressure increase [42, 43]. The increased axial flow retardation increases the liquid film thickness by continuity. Furthermore, the pressure increase also lowers the spreading angle. While this is correlated with the change of the internal film thickness, this can be attributed to the mechanical balance required for the increased pressure.

Geometric parameters may also have significant dynamical effects. In traditional monopropellant swirl injectors, the size of the vortex chamber greatly affects the development of the liquid film and its stability. The vortex chamber diameter and the vortex chamber length both play a role in the stability of the air core [44]. When the diameter is smaller, the liquid jets from the tangential inlets have a shorter moment arm. This causes the gas core to be nonaxisymmetric, or in extreme cases to break up. With an increased moment arm, the formation of the gas core becomes more stable. On the other hand, the length of the vortex chamber cannot be too large. The increased vortex length gives rise to

instabilities, and usually the ratio between this length and the diameter must be below a certain threshold to ensure gas core stability. Another factor is the length of the orifice after the vortex chamber. With increased length, the larger shear stress experienced causes the liquid film to thicken. The inviscid analysis starts to deviate from experimental and numerical results when the ratio of the injector length to the radius exceeds 20 [12].

The response function derived in the earlier section would be affected and design parameters should be specified such that the magnitude of the response is small. Classical swirl injectors have a vortex chamber, which can be elongated to dampen the fluctuations through viscosity and increase the phase difference of the response function. The geometric parameter A can be increased to decrease the mass flow rate fluctuation because the amplitude of the surface wave is decreased with the increased centrifugal force. The increase of pressure drop shows the opposite behavior. Vortex chamber configurations induce a resonance and promote instability due to the reflection of waves within the chamber, so the open-end swirl injectors are usually chosen in favor of the vortex chamber swirl injectors. Furthermore, when there are two rows for the tangential inlet, the fluctuations induced by the tangential inlets will influence each other, generating a reflected wave. The surface wave can be filtered by adjusting the distance between the two rows of tangential inlets [45]. The location of the tangential inlet is determined by the severity of the viscous loss caused by the walls and momentum loss from the liquid film filling up the area upstream of the entry point. There exists an optimum position for the tangential inlet to minimize the momentum loss [12], and the location was treated as a rule of thumb between one radius (tangential inlet radius) and five radii away from the headend of the annulus.

2.6 Conclusion

The previous sections can be summarized as a design procedure for the MCC injector for a given set of operating conditions. Although not detailed, the present results for the MCC injector dimensions match the actual dimensions of the RD-170 MCC injector fairly well. However, a few dimensions deviate from hardware specifications, as the design procedure is still only based off of theory and empirical relations. To fine-tune and finalize the injector design, further investigation is required, involving subscale testing or modeling/simulation.

Physical experiments on high-performance power generation and propulsion systems are extremely expensive, due to the harsh operating conditions and high level of system complexity. Furthermore, the operating conditions limit the use of many types of diagnostic techniques; optical diagnostics are typically the method of choice. These methods, however, offer limited insight into the underlying mechanisms of the physiochemical processes involved. Experimental information alone is not enough to fully analyze, design and optimize the propulsion system, so existing design practices rely on past experience, empirical calculations, and intuition.

On the other hand, simulations require long run times and optimization based on an inexpensive surrogate is necessary. For spatio-temporal simulations, a surrogate model needs to be formulated such that the essential flow physics are still captured. Surrogate-based optimization can enable efficient quantitative assessment of design trade-offs and facilitate global sensitivity evaluations of the design parameters.

CHAPTER 3. SURROGATE MODEL FRAMEWORK

Engineering design has been undergoing a paradigm shift from design for performance to design for affordability, operability and durability, seeking multi-objective optimization. Model-based system engineering (MBSE) is the formalized application of modeling to support system requirements, design, analysis, verification and validation activities, beginning in the conceptual design phase and continuing throughout development and later life cycle phases [46]. Furthermore, MBSE is expected to replace the document-centric approach that has been practiced by engineers in the past and influence future design methodologies by being fully integrated into the engineering process. An integrated database approach to MBSE maintains information throughout the product lifecycle – from concept of operations to design and to production, providing the ability for more effective performance and cost analyses.

There are several design stages depicted within Fig. 10: requirements definition, conceptual design, preliminary design, and detailed design. In the first stage, the requirements posed by the customer are defined. Conceptual design then starts based on experience and prior knowledge. Preliminary design involves transforming the concept so that the product can function properly and meet the customer/market demands. Further testing and fine-tuning is performed in the detailed-design stage. In today's design methodologies, as a program reaches the preliminary design phase, the amount of design freedom rapidly decreases, while the cost commitment and need for design knowledge drastically increase. Take F-1 rocket engine development in the Apollo lunar-landing project as example [17], more than 1300 component and engine tests were performed

during the detailed-design stage to mitigate combustion instabilities, accumulating a tremendous design cost. To remedy this situation, an innovative design process is needed which brings more knowledge to the earlier design phase, keeping design freedom open longer and redirecting cost commitment as depicted in Fig. 10.

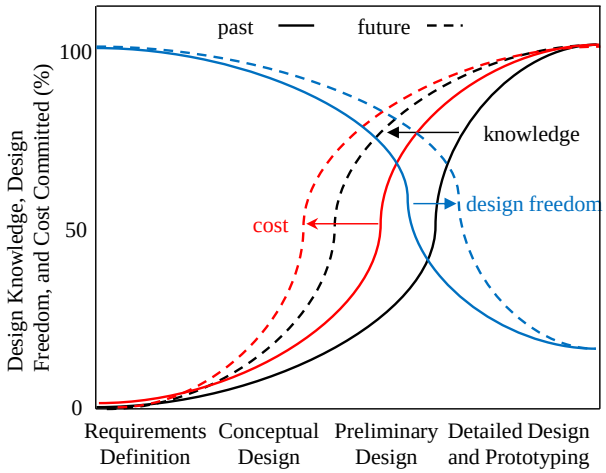

Figure 10. Life-cycle design stages [47].

Traditional, point-design philosophy is usually confined by fixed design requirements and technology assumptions, so the design space exploration is performed around a handful of concepts. As organizations strive to decrease costs, the need for more in-depth analysis at the conceptual and preliminary stages is increasing. As a result, a paradigm shift is required to reduce design cycle time, allowing for more iterations and better fidelity. In order to enable the transition, multi-disciplinary analysis, design and optimization needs to be incorporated. Furthermore, physics-based formulations and models play a vital role in design surveys, especially so for unconventional design concepts. The capability, to perform trade-off analysis and narrow down concept selections, should leverage physics-based models during the early design phases.

Within the context of multi-disciplinary system analysis and design, the life-cycle consideration is deemed essential for evaluating the emerging, all-encompassing system objective affordability [47]. As previously mentioned, engineering design has been undergoing a paradigm shift from design for performance to design for affordability, operability and durability, seeking multi-objective optimization.. Furthermore, there is a need to incorporate lower-fidelity, cheaper models (in addition to the main, high-fidelity calculations). In most cases, the fast and the slow objective values can be obtained independently, measuring the cheap functions on a large number of values. This process is referred to as multi-fidelity optimization [48]. The use of secondary, correlated quantities to enhance the model performance is not a new concept, with the established approach of model building using objectives resulting from computational simulations of varying fidelities and costs [49]. The methodology has been improved by incorporating flexible location and scale adjustments, using Bayesian hierarchical Gaussian process models [50].

Much of the early literature revolves around treating different meshes as various fidelities [51], which then evolved into treating the hierarchy of flow solvers as different fidelities. Global optimization (scalar metrics such as aerodynamic coefficients and wall temperatures) using neural-network- and polynomial-based response surface methodologies has been demonstrated for various applications, ranging from wing aerodynamics, turbulent diffuser flows, gas-gas injectors, to supersonic turbines [52]. Kriging, Gaussian process modeling, has been shown to perform better global approximations than response surface models, as it utilizes a “global” model and Gaussian correlation functions [53]. This model drastically reduces the computational time required for design space exploration and evaluating the objective function during the optimization

process [54]. Kriging, can also be employed to construct cheap surrogate models to integrate information from high-fidelity and low-fidelity models, while quantifying interpolation uncertainty of the model [55]. Techniques emphasizing reduction of high-dimensional design spaces, such as corrected space mapping for variable-parametrization design spaces [56] and imposing partial differential equations-constraints [57], can further reduce computational costs.

Since the introduction of modeling deterministic outputs as a realization of a stochastic process and formulating a statistical basis for designing experiments [58], statistical techniques have been used to build approximations (surrogate models) of expensive computer analysis codes to facilitate multidisciplinary, multi-objective optimization and concept exploration [59]. To iterate, the conceptual design/preliminary design of aerospace systems requires multi-disciplinary analysis tools, which are capable of providing adequate fidelity for efficient design space exploration. In the past, aerodynamic performance has been the focal point for multi-fidelity design procedures, where conceptual low-fidelity optimization tools are combined with a hierarchy of flow solvers of increasing fidelity [60, 61]. Relying on radial basis function interpolation error between a high-fidelity function and a low-fidelity function, maximum likelihood estimator models can be generated based on kriging variance estimates from radial basis function models, and prove convergence and robustness with respect to poor low-fidelity information in a trust region [62]. The term outer-loop application defines such computational applications that form outer loops around a model, where an input is received each iteration and the model output is then computed. The overall outer-loop result is obtained at the termination of the outer loop [63]. There are typically three

applications for multi-fidelity models: uncertainty propagation, statistical inference, and optimization. The construction of low-fidelity models for these functions can be split between simplified models, projection-based reduced models, and data-fit models. Simplified models arise derived from the high-fidelity model, through simplifying physics assumptions, linearization, or implementation. Projection-based models are computed by projecting the governing equations of the high-fidelity model onto a low-dimensional space. Data-fit models are formulated directly from the data, relying on black-box high-fidelity models and response surface approximations through regression analysis. The present work is a hybrid model relying on data-fit regression techniques coupled with physics-based basis functions.

In order to survey the design space, there is a need to identify the optimal range for design parameters and feasible starting points [26]. An integrated design process of combining design principles such as Taguchi methods and response surface methodology [27] into one mathematical framework can be used to address this multi-objective design concept problem. The critical component of the optimization problem is properly formulating the objective function. From a combustion dynamics perspective, quantifying the objective function is a great challenge as there is no clear metric for combustion stability. In most cases, a designer can only conclude relative stability margins with respect to the different configurations.

After developing the surrogate model framework, the optimization is performed by searching the through the design space for the minimum/maximum of the objective. When objectives are conflicting in nature, there may be an infinite number of possible solutions that provide possible good combinations of objectives, known as Pareto optimal solutions.

When two design are compared, the design are said to be non-dominated with respect to each other if neither design dominates the other. The functional space representation of the Pareto optimal set is the Pareto optimal front. When there are two objectives, the Pareto front forms a curve. When there are three objectives, the Pareto front is represented by a surface, and if there are more than three objectives, it is represented by a hyper-surface.

The simulations at hand require long run times and optimization based on an inexpensive surrogate is required. Surrogates are a means to speed up computations, protect proprietary codes, and overcome organizational barriers. For spatio-temporal simulations, a surrogate model needs to be formulated such that the essential flow physics are captured. Surrogate-based optimization can provide quantitative assessment of design trade-offs and facilitate global sensitivity evaluations of the design parameters. A major challenge to the successful full-scale development of aerospace systems is dealing with competing objectives such as vehicle performance, system stability, and manufacturing cost [28]. The surrogates constructed using data drawn from high-fidelity simulations can provide efficient approximations of the objectives at new design points, enabling feasible trade-off studies. As a sufficient number of different designs must be tested to build the surrogate model, the process of selecting different designs is DoE [27, 29].

The data required for formulating the surrogate model can be severely limited due to time and computational constraints of the high-fidelity simulations, which can be visualized using the aforementioned Pareto front concept. Figure 11 shows the Pareto frontier for computational modeling and simulation capability [64]. This illustrates the trade-off between the level of model fidelity and the extent which the designer and explore the design space. In some cases, this problem can be alleviated by performing a low-fidelity

model and translating the result to the higher-fidelity model. In other instances, low-fidelity data, employing corrections for improved accuracy, can be combined with the high-fidelity data to reduce the overall number of expensive runs. With the continuing progress of modeling capabilities, simulation-based optimization has proven to be a useful tool in the design process. However, complex design problems such as rocket engine components can still be a daunting task.

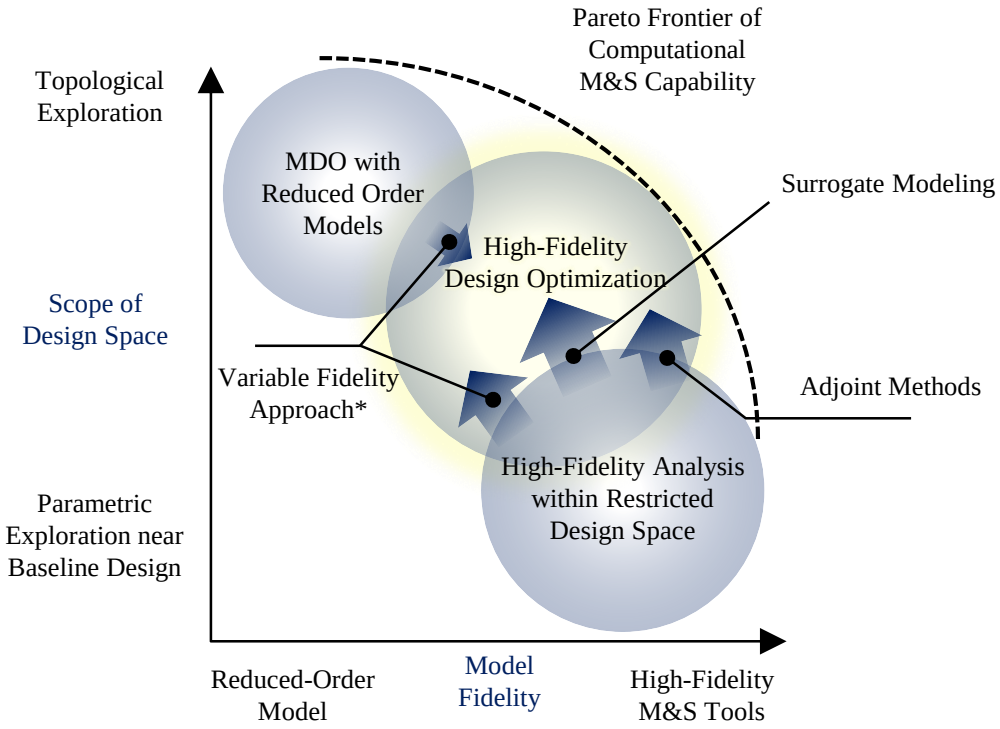

Figure 11. Pareto frontier of computational modeling and simulation capability [64].

3.1 Surrogate Modeling

There are many types of surrogate models to choose from. There are parametric models that include polynomial response surface approximations (RSA) and Kriging models, and there are non-parametric models such as radial basis neural networks (RBNN).

The parametric approaches assume the global functional form of the relationship between the response variable and the design variables is known, while the non-parametric ones use different types of simple, local models in different regions of the data that build up an overall model. Parametric techniques generally make predictions faster due to having functional forms, but tuning parameters are difficult to train. On the other hand, non-parametric ones are fast to train, but have slower predictions since each local basis function needs to be evaluated. Response surface approximations typically assume that the data is noisy and fits the data with a simple, smooth global function to minimize the root-mean-square (rms) error.

With the established performance of kriging for design optimization [53-55], the present study will use this approach for building the surrogate model. Kriging, a technique originating in the field of geostatistics [65], is a powerful machine-learning tool for interpolation and prediction. The key idea is to model unobserved responses using a Gaussian process (GP) governed by a preset covariance function. The response surface of the trained kriging model can then be obtained by applying data-tuned weights to radial basis functions centered at observed points. Thus kriging can use function values sampled at a set of input parameters and approximate well the entire function surface over its domain. With appropriately chosen parameters, the kriging model provides the best linear unbiased estimator of the responses at designs that have not been simulated [29]. Furthermore, the resulting posterior distribution of this prediction will also be Gaussian. For problems of modeling spatio-temporal flow evolution, the observed points over the entire design space are sparse, because the daunting computational costs limit the number of affordable simulation cases. Conventional machine-learning techniques relying on “big

data" over the design space would fail. Rather, the "big data" lies within the flowfield information, which encompasses a wide range of length and time scales. The proposed methodology combines machine-learning techniques with domain knowledge of the physical system to build an accurate emulator model [66]. The inclusion of flow physics allows the data-driven model to be physically interpretable with enhanced emulation performance.

The objective of the present study is to develop a kriging model capable of treating different spatial grids while capturing dynamic information [66]. The spatial and temporal resolution of all of the simulation cases is very fine, making direct use of the raw data for training a predictor computationally demanding. The kriging model must not only incorporate data generated from different spatial grids [67-69] and use data-reduction methods, but it must also be extended to multiple, functional outputs. A handful of studies have been published on multiple-output kriging [70, 71] and functional outputs, including wavelet decomposition [72] and knot-based GP models [73]. For data with fine spatio-temporal resolution, unfortunately, these types of methods are inappropriate because of the substantially increased computation time required [66].

Here, an emulation framework for a spatio-temporal surrogate model is presented using a simplex swirl injector for demonstration. A reduced-order model is developed and implemented to handle large scale spatio-temporal datasets with practical turn-around times for design iteration. Recent reduced-order model studies have not focused on modeling and predicting spatio-temporal flowfields, but rather focusing on closure terms [74-79]. Prior attempts at using Gaussian process models [80] and decomposition techniques with Galerkin projection leveraging radial basis functions have shown some

success for unsteady flowfields [81-85]. The proposed model is trained with datasets that have been classified based on established physics to reap the benefits of incorporating machine learning techniques into the framework. The model can accurately retain the rich set of physics from LES-based high-fidelity simulations and predict flow structures.

The present study develops an integrated framework that incorporates state-of-the-art statistical methods, machine learning algorithms, and a physics-driven data reduction method to obtain a surrogate model over a broad range of design space. The emulation framework relies on Proper Orthogonal Decomposition (POD) [86] (also known as the Karhunen-Loeve decomposition in the theory of stochastic processes [87]) to extract the flow physics and reduce the data by representing the flowfield with basis functions. This technique can be combined with kriging to build an efficient and physics-driven emulator. The Common POD (CPOD) analysis is introduced and conducted by means of a common grid generated from simulations of the geometries designated by a DoE. Although this approach is similar to that of Higdon et al. [88] for generalizing a POD expansion, the novel technique developed herein directly addresses the need for a set of common basis functions required for a kriging model. In our companion paper on basic theories [66], the statistical properties of a broader class of CPOD-based emulators are considered.

The current work applies machine-learning techniques and investigates the practical performance of the emulator with respect to flow physics. The emulated flowfield is validated against an LES simulated flowfield to demonstrate how the flow structures and injector characteristics are captured by the model. In addition, the model allows for spatio-temporal uncertainty quantification (UQ). This metric can be used to verify the model and quantify underlying flow properties.

The chapter is structured as follows. Section 3.2 and 3.3 provides the physical model, describing the baseline configurations, the design points designated by the DoE, the high-fidelity simulation technique, and the simulation results. Section 3.4 discusses the data-driven emulation framework proposed for the design methodology and surrogate model. Section 3.5 details the application of the framework, while assessing the surrogate model using performance metrics, root-mean-square errors, and PSD of simulated and predicted flowfields. Finally, this chapter concludes with a summary and directions for future work.

3.2 Physical Model

Figure 12 shows a schematic of a simplex swirl injector representative of those commonly used in applications like liquid-fueled propulsion engines [9, 10]. The five parameters that define the geometry are injector length, L, injector radius, R_n, inlet slot width, δ, tangential inlet angle, θ, and the distance between the inlet and headend, ΔL. These design parameters play an important role in determining the injector performance, including the thickness, h, and spreading angle, α, of the liquid film at the injector exit. The selection of these design parameters is dependent upon engine requirements. Table 2 shows the design space and the ranges of each parameter considered here. To generalize the emulator framework, a broad range of these parameters was chosen. The range of injector lengths was chosen to include those of small upper-stage rockets such as the RD-0110 [89], about 22.7 mm, and large first-stage engines like the RD-170 [15], about 93 mm.

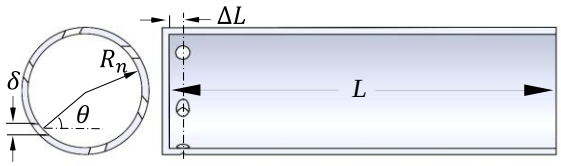

Figure 12. Schematic of swirl injector.

Table 2. Design space for injector geometric parameters.

L (mm)	R_n (mm)	θ (°)	δ (mm)	ΔL (mm)
20-100	2.0-5.0	45-75	0.5-2.0	1.0-4.0

LOx at a temperature of 120 K is delivered tangentially into the injector through inlets. The operating pressure is 100 atm, typical of contemporary liquid rocket engines. The ambient gas is oxygen at 300 K. The flow dynamics of this class of injectors have been systematically investigated in detail by Zong et al. [12] and Wang et al. [13]. Here we first conduct a set of high-fidelity simulations based on conditions in the design space described in Table 2, then extract the common flow structures for surrogate modeling.

3.3 High-fidelity Simulations

An integrated theoretical and numerical framework is implemented, to treat supercritical fluid flows and combustion over a broad range of fluid thermodynamic states [90-92]. Turbulence closure is achieved using LES. Thermodynamic properties are evaluated by fundamental thermodynamics theories in accordance with the modified Soave–Redlich–Kwong equation of state. Transport properties are estimated using extended corresponding-state principles [90]. The numerical scheme is a density-based,

finite-volume methodology, along with a dual-time-step integration technique. The overall algorithm is self-consistent and robust, with implementation of a preconditioning scheme and a detailed treatment of general fluid thermodynamics [91, 92].

Owing to the demanding computational requirements of three-dimensional simulations, only a cylindrical sector with periodic boundary conditions in the azimuthal direction is simulated. The previous studies have shown that the predicted injector characteristics, such as spreading angle and liquid film thickness using the present method, had good agreement with classical theory [12]. The objective is to ensure that the emulation captures these characteristics within and in the downstream region of the injector simulation. The azimuthal flow dynamics is not a major concern, as the focus is on developing a model that retains the physics of any spatio-temporal flowfield. The discrete injection orifices are converted into an axisymmetric slot through dynamic similarity. A multi-block domain decomposition technique, combined with a message passing interface for parallel computing, is applied to improve computational efficiency. A typical simulation takes about 30,000 CPU hours on a single Intel Xeon processor to obtain statistically significant data, with a total span of 30 ms physical time, after reaching a fully developed state (~24 ms). The simulated data are sampled every 30 computational time steps, with 1 μs between time steps. According to the Nyquist criterion, a temporal resolution of 16.5 kHz is achieved.

3.3.1 Design of Experiments

Given the design space in Table 2, if 10 variations are assigned for each design parameter, the total number of design points is 10^5 for a full factorial design. It is

impractical to perform so many simulations, due to the extensive computing resources required to acquire usable data. A DoE methodology is therefore required to reduce the number of design points and still capture the prominent features in the design space. To this end, the maximum projection (MaxPro) design proposed by Joseph et al. [93] is implemented for good space-filling properties and GP modeling predictions. Thirty points in the expected range of 5-10p (6p rule with p=5, the number of design parameters) points, commonly used in computer experiment literature as suggested by Loeppky et al. [94], are simulated over the entire design space. The accuracy of prediction should always be checked to determine whether additional simulations are needed (see Loeppky et. al. [94] for details). Figure 13 shows a two-dimensional projection of the 30 simulation runs by MaxPro design, which gives representative design points distributed to fill the two-dimensional projection of the design space. Good space-filling properties are observed for all parameters.

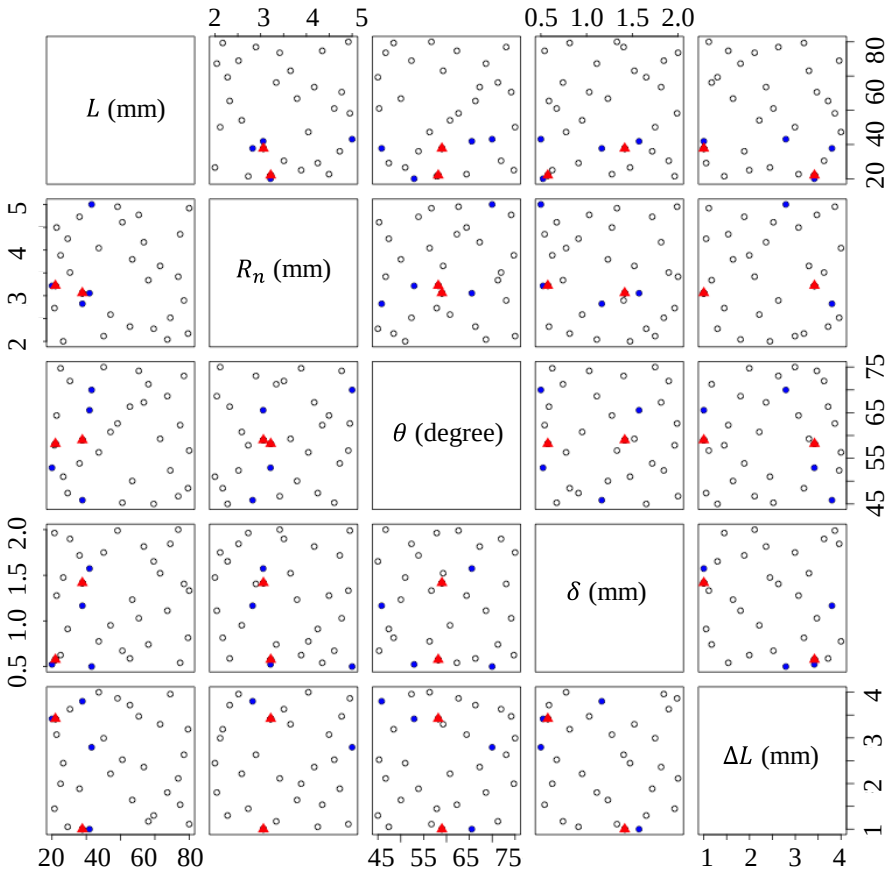

Figure 13. Two-dimensional projections of design points: benchmark points (▲), baseline and neighboring points (●).

3.3.2 Modelling and Simulation

The thirty high-fidelity simulations at design points defined by MaxPro were conducted. To isolate the effect of injector parameters, the mass flow rate for all runs is fixed at 0.15 kg/s. The first two design points designated by MaxPro are chosen as the baseline geometries, A and B in Table 3. The benchmark points used for assessing the accuracy of the emulator model are obtained by offsetting the design parameters of these two points.

Table 3. Injector geometrics at design points colored blue in Fig. 13

Design	L (mm)	R_n (mm)	θ (°)	δ (mm)	ΔL (mm)
A (swirl)	20.0	3.22	52.9	0.52	3.42
B (jet-like)	41.9	3.05	65.5	1.57	1.00
C (swirl)	43.1	5.00	70.0	0.50	2.79
D (jet-like)	37.7	2.82	45.8	1.17	3.80

Figures 14 and 15 show the instantaneous distributions of temperature and density for two neighboring design points, C and D in Table 3, selected to indicate different flow features in the design space. The key flow structures include the swirling liquid film along the wall due to centrifugal force, liquid accumulation near the injector headend and associated flow recirculation, and a conical liquid sheet spreading outward at the injector exit propelled by azimuthal momentum and a hollow gas core in the center region [12, 13].

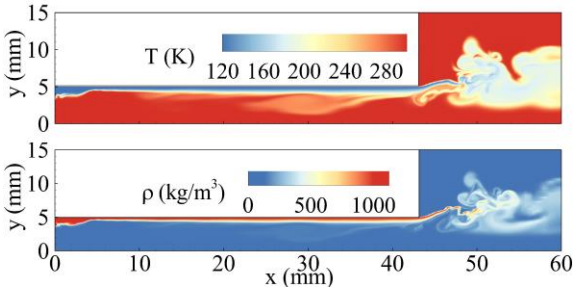

Figure 14. Instantaneous distributions of temperature and density for Design C

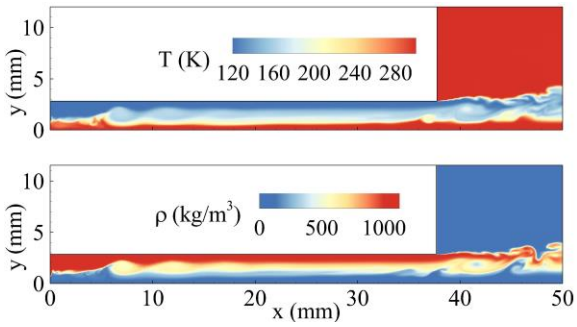

Figure 15. Instantaneous distributions of temperature and density for Design D.

Various flow physics are observed. The film thickness for Design C is much thinner than for Design D, with a larger spreading angle at the injector exit (34.6° compared to 29.2° for Design D). Among the 30 design points, some act like swirling flows, as in Design C, while others behave like jet flows, as in Design D. For convenience, the critical value of the spreading angle that separates swirling from jet-like flows is chosen to be 30°; this angle is considered to be an empirical indicator of whether the liquid stream has significant radial penetration in the downstream region. When this angle is not achieved, the liquid does not have enough radial momentum to spread outwards. The 30 simulation runs are thus divided into two subgroups, swirling (spreading angle above 30°) and jet-like (spreading angle below 30°) flows. In the next section, a machine-learning technique, decision tree, is introduced to identify the jet-swirl dichotomy. This directly influences the feature extraction and kriging processes described in the following sections, as it changes how the design space is partitioned between the identified flow behaviors. Implicitly, the extracted coherent structures will change slightly, depending on the established criteria separating swirling and jet-like flows.

3.4 Surrogate Model

Design points may display similar or significantly different flow structures. In this section, the collected dataset from all 30 high-fidelity simulations is used to perform a data-driven analysis of the design space using machine-learning tools. The work consists of two components: (a) a sensitivity analysis for identifying important design parameters with respect to the quantities of interest, where the Sobol' indices [95] are used, and (b) a decision-tree learning process with respect to the jet-swirl dichotomy, and the incorporation of this information into the emulator model. After the sensitivity analysis and decision tree learning, CPOD is then implemented to extract the flow characteristics over the design space. Lastly, the time-coefficients for the obtained basis functions are employed as training data for the kriging model. This methodology allows us to make accurate flow predictions at any new design setting. A flowchart of the overall data-driven emulator framework is provided in Fig. 16.

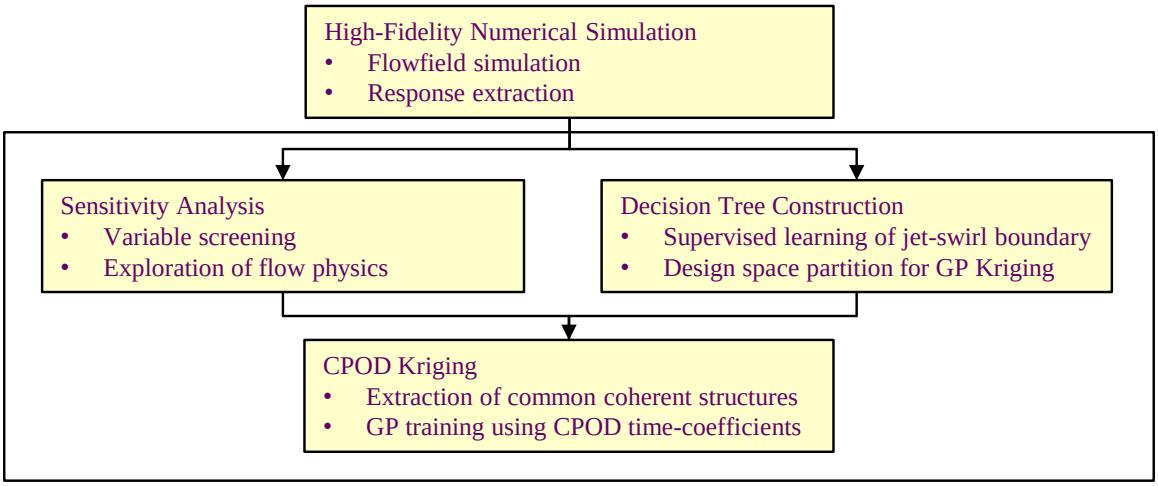

Figure 16. Flowchart for data-driven analysis and emulator construction.

3.4.1 Sensitivity Analysis

The first component of this emulator framework is a sensitivity analysis using Sobol' indices [95] to identify which design parameters contribute more to changes in responses of interest, such as liquid-film thickness or spreading angle. The analysis is also a valuable tool for parameter reduction. The idea is to decompose the variations of certain desired output variables into the partial variations attributable to each input parameter and the effects of interactions between parameters. Such a method of analyzing sensitivity has close connections to the classical analysis-of-variance employed in linear regression models [96].

To put it in mathematical terms, let $f(c)$ be the desired response output at design setting $\boldsymbol{c}$, where $\boldsymbol{c} = (c_1, c_2, \dots, c_p)$ corresponds to the input parameters over a unit hypercube $[0,1]^p$. Specifically, for the current study, $p = 5$ and $c_1 = L$, $c_2 = R_n$, $c_3 = \theta$, $c_4 = \delta$, and $c_5 = \Delta L$, with the design range for all parameters normalized to the interval $[0,1]$. Define the random variable $\boldsymbol{X}$ as a uniform distribution over $[0,1]^p$, and let $f_0 = \mathbb{E}[f(\boldsymbol{X})]$ be the response mean and $D = Var[f(\boldsymbol{X})]$ be the response variance over the design range. The goal is to decompose the response variance D into the contributions for each design parameter $c_1, \cdots, c_p$, as well as the effects of interactions between parameters. Consider the following decomposition:

$$f(\boldsymbol{c}) = f_0 + \sum_{i=1}^{p} f_i(c_i) + \sum_{1 \le i < j \le p} f_{i,j}(c_i, c_j) + \cdots + f_{1,2,\cdots,p}(c_1, \cdots, c_p), \qquad (3.1)$$

where each summand satisfies

$$\int_0^1 f_{i_1,\dots,i_t}(c_{i_1},\cdots,c_{i_t})\,dc_k = 0, \tag{3.2}$$

for any $k = i_1, \dots, i_t$ and has orthogonal components. In Eq. (3.1), the main effect index of input i is:

$$f_i(c_i) = \int (f(c) - f_0)\,dc_{-i}, \quad c_{-i} = \{c_1,\cdots,c_p\}\backslash\{c_i\}, \tag{3.3}$$

and the two-way interaction index of inputs i and j is:

$$\begin{aligned} f_{i,j}(c_i,c_j) = & \int \{f(c) - f_0 - f_i(c_i) - f_j(c_j)\}\,dc_{-i,j}, \\ & c_{-i,j} = \{c_1,\cdots,c_p\}\backslash\{c_i,c_j\} \end{aligned} \tag{3.4}$$

Squaring both sides of Eq. (3.1) and taking the integral over $[0,1]^p$, we get:

$$D = \sum_{i=1}^{p} D_i + \sum_{1\le i<j\le p} D_{ij} + \sum_{1\le i<j<l\le p} D_{ijl} + \cdots + D_{1,2,\dots,p}, \tag{3.5}$$

where D_u is the partial variance corresponding to a subset of parameters $u \subseteq \{1,\cdots,p\}$:

$$D_u = \int f_u^2(c_u)dc_u. \tag{3.6}$$

The Sobol' sensitivity indices for parameter subset u can be defined as [95]:

$$S_u = \frac{D_u}{D} \in [0,1], \tag{3.7}$$

with larger values of S_u indicating greater importance of the interaction effect for u.

In practice, Sobol' indices can be estimated as follows. First, a pseudo-random parameter sequence is generated using a low discrepancy Sobol' point set [97]. Second, this sequence is used to approximate the above integrals, which can then provide estimates for the corresponding Sobol' indices. The quantification of the response sensitivity for each parameter serves two purposes: (a) it provides a preliminary analysis of important effects in the system, which can guide further physical investigations, and (b) it allows for a reduction of the number of parameters that must be considered in the emulator, thereby providing a computationally efficient way to survey flow properties within the design space. A detailed discussion of the sensitivity analysis is presented in Section 3.5.1 for the current physical model.

3.4.2 Decision Tree

As mentioned previously, there exists a jet-like/swirling flow dichotomy within the design space. For simulated design points, it is easy to classify whether such a parameter combination results in a jet-like or swirling flow, because the flowfield data are readily available. For design settings that have not been simulated, a data-driven technique is needed to make such a classification. With this technique, first of all, a boundary between jet-like and swirling cases can be established over the design space of interest, which can then be used to gain physical insight into the design space and to guide additional experiments. Second, the classification information can be used to train separate surrogate

models within the jet-like and swirling domains. This partitioning of the emulator training dataset allows the model to extract different flow characteristics associated with jet-like and swirling behavior separately, and can thereby improve its predictive accuracy. The powerful machine-learning tool ‘decision tree’ is employed for the classification process.

A decision tree is a decision support tool that models decisions and their possible consequences and decision trees are one of the most popular predictive models in data mining and machine learning [98, 99]. Such methods are a part of a larger class of learning methods called supervised learning [100, 101], which aims to predict an objective function from labeled training data. A classification tree, a special type of decision tree, is used here. It specializes in predicting classification outcomes, such as whether a parameter set has a jet-like or swirling flow. The trained model can be summarized by a binary tree, separating the design space into two subgroups. Each node of this tree represents a parameter decision, and each leaf of the tree indicates the class of outcomes, following the chain of decisions made from the tree root.

A classification tree can be trained using the following algorithm (see [101] for details). First, the simulated flowfields of each sampled design point are examined and classified as either jet-like or swirling flow, depending on the radial penetration of the propellant in the downstream region. Next, a search is conducted over all the design parameters and possible split-points, finding the parameter constraints which minimize misclassification. A branch is then made in the classification tree corresponding to the parameter constraint. The same branching procedure is repeated for each of the resulting child nodes. For the analysis in Section 4, the Gini impurity index [101] is selected as the misclassification measure:

$$\hat{p}_j\left(1 - \hat{p}_j\right) + \hat{p}_s(1 - \hat{p}_s), \tag{3.8}$$

where $\hat{p}_j$ and $\hat{p}_s$ are the proportions of jet-like and swirl cases in a split. The index measures how often a randomly chosen sample is incorrectly labeled when such a label is randomly assigned from the dataset. Notice that a Gini index of 0 indicates that (a) $\hat{p}_j = 1$ and $\hat{p}_s = 0$, or (b) $\hat{p}_j = 0$ and $\hat{p}_s = 1$, both of which suggest perfect classification. When the Gini impurity index is around 0.5, jet-like and swirl cases are equally distributed. If more than two groups are considered in the injector dynamics, the Gini impurity index can be generalized for other number of groups, which can be seen in [101].

This decision tree learning technique not only provides a means for partitioning the training dataset for the model into jet-like and swirling flows, it also reveals physical insights into the important design parameter constraints causing the jet-swirl dichotomy. The quantification of this split is achieved through the calculation of the Gini impurity. The Gini index is a criterion to minimize for classification. 0.5 is the worst classification possible, but the optimization procedure aims to find the best classification possible (i.e., one with smallest Gini index). If this optimal classification with two categories is not good enough, then the approach should be generalized for classification trees with more than two categories. The interpretability of these constraints is elaborated in Section 3.5.

3.4.3 Kriging Surrogate Model

The primary objective of this work is to develop an emulator model that uses data from 30 simulation runs to predict the flowfield of a new design point within a practical turnaround time. With the tools described above – the sensitivity analysis for parameter

screening and the decision tree for partitioning the design space into jet-swirl cases – a surrogate model for flowfield emulation is proposed. The kriging surrogate model, also known as an emulator, combines machine-learning techniques, statistical modeling, and a physics-driven data reduction method. A brief explanation for each part of this model is provided, before discussion of the specific mathematical details. A complete description of the model development from the statistical perspective is given in [66].

First, the proposed model is constructed through a POD analysis of the simulation dataset used for training. For a given flow property, f, the POD analysis determines a set of orthogonal basis functions, ϕ_j , such that the projection of the property onto these basis functions has the smallest error, defined as $E\left(\left\|f-\hat{f}\right\|^2\right)$ where $E(\cdot)$ and $\|\cdot\|$ denote the time average and norm in the L^2 space, respectively [86]:

$$\hat{f}(\boldsymbol{x},t)=\sum_{j=0}^{n}\beta_j(t)\phi_j(\boldsymbol{x}) \tag{3.9}$$

The basis functions, or mode shapes, are spatial distributions of the fluctuating fields of flow properties, which can be closely linked to physical phenomena and coherent structures. The basis functions are ordered in such a way that the lowest modes have the highest "energy," as defined by the inner product of f. The flow properties for POD analysis include pressure, density, temperature, and velocity components. POD decomposition yields not only the eigenfunction modes, ϕ_j, and but also their corresponding time-varying coefficients, β_j, which are referred to as POD coefficients. It should be noted that this process is not completed for the entire dataset; physical variables

are processed separately. In order to treat the data together, scaling and dimensions need to be carefully formulated to obtain interpretable mode shapes.

While the usage of POD simplifies the complex nature of a spatio-temporal model, a common set of basis functions is required for the emulator, in order to accommodate different injector geometries. Physically, this means that a common set of coherent structures needs to be extracted over the design space. One option is to select a computational region of interest that is unaffected by any design changes [102]. Taking advantage of the basis functions generated by the POD analysis, an emulator can be obtained as long as a set of common basis functions exist. One of the challenges for the current study is the wide disparity of geometries in the design space, as illustrated in Fig. 17. The present work utilizes a common grid for the 30 grid systems to find a set of common basis functions. To achieve this, the densest grid system, which has the highest number of cells, among all cases is identified and split into four sections covering the effects of design parameters on the simulated grid. This partitioned grid is used for interpolation and rescaling of each simulated case to obtain a common grid. Then, an inverse distance weighting interpolation method with ten-nearest neighborhood points is used to map the original raw data onto the common grid [103]. Algorithmically, the CPOD expansion is obtained by first rescaling the different cases to the common grid, then

computing the POD expansion, and finally rescaling the resulting modes back to the original grid [66].

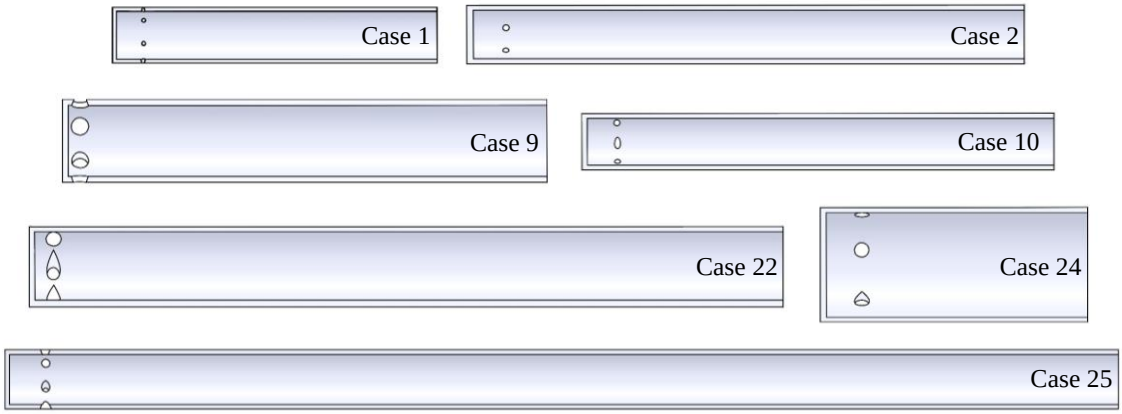

Figure 17. Schematics of different injector geometries in the design space.

Because of the limited variation of the Reynolds number among the different injector geometries, the scaling of the data to the common grid is appropriate in the present study. The smallest injector diameter of concern is 4 mm, with a corresponding exit velocity of 27.5 m/s. With the liquid oxygen density of 1000 kg/m^3 and viscosity of 0.114 cP, the Reynolds number based on the injector diameter is about 9.6×10^5. The largest injector diameter in the design space has a value of 10 mm, and the corresponding exit velocity is 11 m/s. At the same operating condition, the Reynolds number is about 9×10^5. For some geometries where the liquid film does not produce a noticeable spreading angle, the Reynolds number is reduced to about 9×10^5. Despite this difference, the model is capable of avoiding excessive smoothing, provided the correlation function is bounded correctly. Such scaling of POD modes to establish common basis functions is vital to the emulator. It should be noted that the scaling is only appropriate for flow simulations that do not exhibit distinctively different physical phenomena, such as those of reacting flow

simulations, where the mode shapes change drastically. Additional similarity parameters may be necessary when different physics and chemical reactions are incorporated, as reviewed by Dexter et al. [104].

The mathematical details for CPOD are provided below [66]. Suppose n simulations are conducted at various design geometries $\boldsymbol{c}_1, \dots, \boldsymbol{c}_n$ and let $f(\boldsymbol{x}, t; \boldsymbol{c}_i)$ be the simulated flowfield at design $\boldsymbol{c}_i$ for a given time t and spatial coordinate $\boldsymbol{x}$. The k-th CPOD mode is defined as

$$\begin{gathered}\phi_k(\boldsymbol{x}) = \underset{\psi:\|\psi\|_2=1}{\operatorname{argmax}} \sum_{i=1}^{n} \int \left[\int \mathcal{M}_i[\psi(\boldsymbol{x})] f(\boldsymbol{x}, t; \boldsymbol{c}_i) d\boldsymbol{x} \right]^2 dt\,, \\ s.t. \int \psi(\boldsymbol{x}) \phi_l(\boldsymbol{x}) d\boldsymbol{x} = 0, \forall\, l < k\end{gathered} \tag{3.10}$$

Here, the map $\mathcal{M}_i: \mathbb{R}^2 \to \mathbb{R}^2$ is the transformation which linearly scales spatial features from the common geometry $\boldsymbol{c}$ to the i-th geometry $\boldsymbol{c}_i$. The sequence of POD coefficients is defined as:

$$\beta_k(\boldsymbol{c}_i, t) = \int \mathcal{M}_i\{\phi_k(\boldsymbol{x})\} f(\boldsymbol{x}, t; \boldsymbol{c}_i) d\boldsymbol{x}, \tag{3.11}$$

with the corresponding POD expansion using K modes given by:

$$f^{(K)}(\boldsymbol{x}, t; \boldsymbol{c}_i) = \sum_{k=1}^{K} \beta_k(\boldsymbol{c}_i, t) \mathcal{M}_i\{\phi_k(\boldsymbol{x})\}. \tag{3.12}$$

The transformation allows for the extraction of common basis functions. In addition, the obtained modes can be used to identify key mechanisms of flow dynamics. It should be noted that reacting-flow simulations are characterized by additional dimensionless parameters, and linear mapping may not perform well when combustion is involved.

Two computational challenges need to be addressed to implement this methodology. As previously mentioned, to calculate the inner product of the snapshots from different simulation cases, a common set of spatial grid points is needed. Not only does the calculation of the inner product become a computational bottle-neck, as the covariance matrix consists of snapshots from each simulation, the number of modes required to capture a certain energy level is significantly increased relative to an individual simulation, which needs approximately six modes to capture more than 95% of the total energy [12]. The computation of CPOD modes and associated time-varying coefficients requires eigen-decomposition of a $nT \times nT$ matrix, where n is the number of simulation cases and T the number of snapshots. This usually requires $O(n^3T^3)$ computation work. A typical value for T is 1,000 snapshots spanning 10 ms, which achieves a frequency resolution of 100 Hz. An iterative method of eigen-decomposition based on periodic restarts of Arnoldi decompositions is then used to quickly calculate the first few eigenvectors with the largest eigenvalues. These eigenvalues can also be interpreted as the amount of the "energy" as defined by the inner product used to calculate the covariance matrix. For a particular reconstruction using a linear combination of POD modes and associated time-varying coefficients, there is reconstruction error, which decreases when more eigenvectors, the POD modes, are included.

Next, a kriging model is applied to the CPOD time-varying coefficients $\beta_k(\boldsymbol{c}_i, t)$. With the mean and variance computable in closed form, uncertainty quantification and confidence intervals can be calculated easily. Kriging (and more generally, GP-based learning) has been applied to great success in a variety of fields [105]. The mathematical approach of kriging is described here. For notational simplicity, let $\beta(\boldsymbol{c})$ denote $\beta_k(\boldsymbol{c}, t)$, the k-th CPOD coefficient at setting $\boldsymbol{c}$ and time-step t. As the temporal resolution is fine, there is no practical need to estimate temporal correlations, especially because predictions will not be made in between time-steps. This time-independent emulator uses independent kriging models at each instant of time, assuming the following GP model:

$$\beta(\boldsymbol{c}) = \mu + Z(\boldsymbol{c}), \qquad Z(\boldsymbol{c}) \sim N\{0, \sigma^2 R(\cdot,\cdot)\} \tag{3.13}$$

Here, μ is the mean, $Z(\boldsymbol{c})$ is a zero-mean GP with variance σ^2, and $R(\cdot,\cdot)$ is a pre-specified correlation function governed by unknown parameters $\eta's$. A typical choice for $R(\cdot,\cdot)$ is the so-called Gaussian correlation function:

$$R(\boldsymbol{c}_i, \boldsymbol{c}_j) = \exp\left[-\sum_{k=1}^{p} \eta_k \left(c_{ik} - c_{jk}\right)^2\right] \tag{3.14}$$

where p is the number of input parameters.

Now, suppose the function values $\boldsymbol{\beta}^{(n)} = [\beta(\boldsymbol{c}_i)]_{i=1}^n$ are observed at input settings $\{\boldsymbol{c}_i\}_{i=1}^n$, and let $\boldsymbol{c}_{new}$ be a new setting for which prediction is desired. Conditional on the observed values $\boldsymbol{\beta}^{(n)}$, the best linear unbiased estimator of $\beta(\boldsymbol{c}_{new})$ can be shown to be [29]:

$$\hat{\beta}(\boldsymbol{c}_{new}) = \mu + \boldsymbol{r}_{new}^{T}\boldsymbol{R}^{-1}(\boldsymbol{\beta}^{(n)} - \mu\mathbf{1}) \tag{3.15}$$

Here, $\mathbf{1}$ is the n x 1 vector of ones, $r_{new} = [R(\boldsymbol{c}_i, \boldsymbol{c}_{new})]_{i=1}^{n}$ is the n x 1 vector of correlations between the new point and sampled points, and $\boldsymbol{R} = \left[R\left(\boldsymbol{c}_i, \boldsymbol{c}_j\right)\right]_{i=1}^{n}{}_{j=1}^{n}$ is the covariance matrix for the sampled points. Such a predictor minimizes the mean-squared prediction error (MSPE), a commonly-used criterion for prediction error. In the context of flowfield prediction, employing this kriging estimator allows us to obtain accurate flow predictions from the CPOD coefficients. It can also be shown [29] that this best MSPE predictor is unbiased, matching the expected and true function value.

To close the formulations, the model parameters μ, σ^2 and η need to be trained using data. A technique called maximum likelihood estimation (MLE), a ubiquitous estimation technique in statistical literature [106], is employed. The key idea in MLE is to search for the optimal parameter setting that minimizes the likelihood function of the GP model. In the present work, optimization is achieved by means of the L-BFGS algorithm [107], a method employed for many training algorithms. A more detailed explanation can be found in Santner et al. [29].

The kriging models are trained independently over each time step, due to the inherent fine-scale temporal resolution of the simulation. This time-independence assumption is made for two reasons. First, the fully developed flow is treated as statistically stationary and has high frequency resolution, so there is no practical value for estimating temporal correlations. Second, as in the high-fidelity simulation procedure, the assumption of time-independence allows exploitation of parallel computation in training the emulator

model. Once the model is trained, the predictor is used with the CPOD expansion to predict the flow evolution at a new design point, that is,

$$\hat{f}(\boldsymbol{x}, t; \boldsymbol{c}_{new}) = \sum_{k=1}^{K} \hat{\beta}_k(\boldsymbol{c}_{new}, t)\mathcal{M}_i\{\phi_k(\boldsymbol{x})\} \tag{3.16}$$

It is worth noting that the computation time of the proposed model is orders of magnitude smaller than that of LES. Simulation data that typically takes a week, or around 30,000 CPU hours, to acquire, can be predicted by the model with an associated uncertainty in a manner of tens of minutes. The full emulator model and algorithm are provided in the statistical paper [66], which considers the statistical properties of a broader class of models. This work focuses on applying new machine-learning techniques and investigates the practical performance of the emulator with respect to flow physics.

3.5 Results and Discussion

3.5.1 Sensitivity of injector geometrical parameters

Liquid-film thickness and spreading angle are two important injector characteristics. An inviscid, incompressible-flow theory predicts the spreading angle as a function solely of the geometric constant [9, 10], and it increases with increasing geometric constant. For real fluids at supercritical conditions as treated in the present study, the fluid density varies continuously [12, 13]. The spreading angle can be determined based on the slope of the maximum density gradient near the injector exit in a time-averaged sense. As the maximum density gradient is utilized as the boundary for liquid film, the spreading

angle and film thickness have variances related to how prominent the maximum density peak appears in the radial direction.

To gauge the importance of each injector parameter on the liquid-film thickness and spreading angle, a sensitivity analysis using a Monte Carlo estimate of Sobol' indices was performed [95]. Figure 18 shows the primary effects from this sensitivity analysis. The points indicate the Sobol' index estimate for each design parameter, with lines indicating the Monte Carlo integration error for each index estimate. The lines were calculated based on a 95% confidence interval of the estimate. The significant parameters were circled with red solid lines, and attributes that had a minor effect were circled with dash lines. The slot width (δ) is found to be the parameter with the largest Sobol' index and thus the strongest influence on the spreading angle. Physically, this can be explained by how geometric parameters govern the inlet flow properties. Assuming a constant mass flow rate, the incoming velocity is inversely proportional to the slot width, and a decrease in slot width increases liquid-film momentum, increasing momentum of the liquid film.

Similarly, the tangential inlet angle (θ) and the slot width significantly affect the liquid-film thickness, while the length (L) and radius (R_n) of the injector have minor effects. The tangential inlet angle controls the direction of momentum. As the injector angle increases, more azimuthal momentum is imparted to the liquid film, thereby increasing the spreading angle at the injector exit. The length and radius can dictate how much viscous loss is experienced by the propellant, as it travels in both the axial and azimuthal directions. The present study, however, has shown viscous losses to be a minor effect. Referring to Eq. (3.7), larger values of S_u indicate greater importance of the interaction effect for u. When $|u| = 1$, the sensitivity is called the 'mean effect index'.

Another measure of sensitivity often considered is the 'total effect index', which measures the contribution to the output of a given input $\boldsymbol{X}_u$, including all interactions of $\boldsymbol{X}_u$ with other inputs. That is,

$$T_u = S_u + \sum_{l \in u^c} S_{l \cup u} \in [0,1], \tag{3.17}$$

where u^c is the complementary set of u. Similarly, larger values of T_u indicate greater importance of the effect for u.

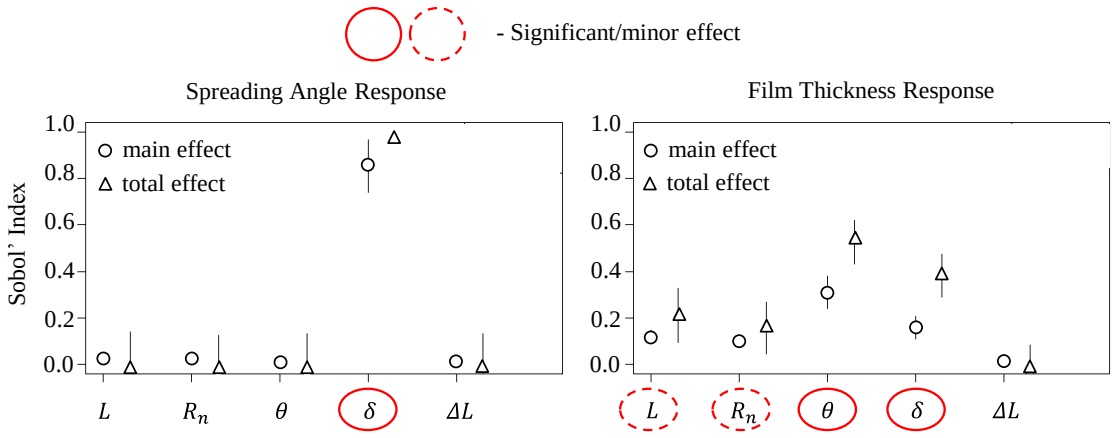

Figure 18. Sensitivity analysis of liquid-film thickness and spreading angle.

Figure 19 shows the two-factor interaction effects. It further demonstrates that the main design parameters are the slot width and the tangential inlet angle (interaction effects circled in blue), which couple to affect the liquid-film response. This is hardly surprising, as slot width and inlet angle govern flow area and direction of momentum, respectively. The mass and momentum conservation equations are inherently coupled to govern the flowfield.

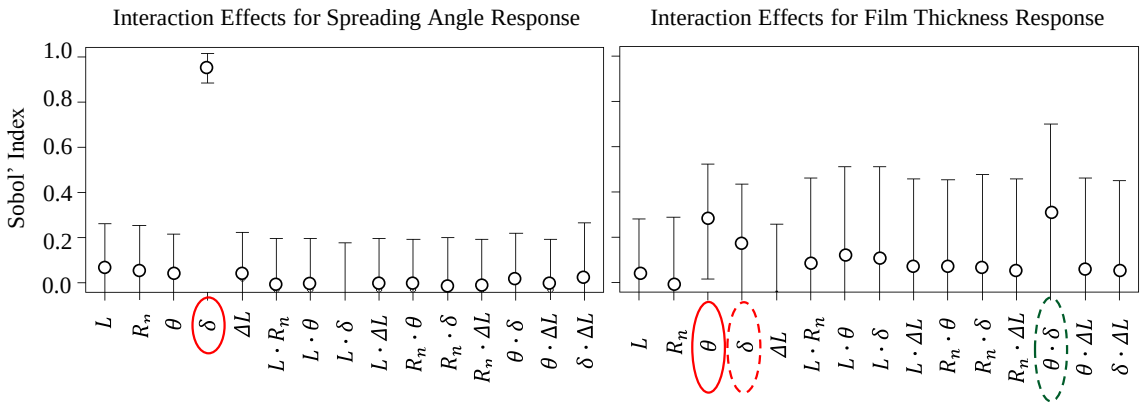

Figure 19. Two-factor interaction of liquid-film thickness and spreading angle.

As previously mentioned, the empirical geometric constant for a swirl injector can be employed to estimate the film thickness and spreading angle, using the hydrodynamics theories described by Bazarov and Yang [9, 10]. These theories, however, are based on the assumption of incompressible, inviscid flows and can only be used as a preliminary guide. In real injectors, viscous and compressibility effects must be considered. The liquid viscosity results in boundary layer formation along the walls, which causes spatially non-uniform velocity profiles. A primary effect of compressibility lies in the existence of acoustic waves [12, 13]. The supercritical conditions within high pressure systems make these effects even more pronounced. High-fidelity simulations taking into account real-fluid effects are required to address these issues [12, 13].

3.5.2 Decision tree exploration of injector design space

Further examination of simulated design points shows a clear distinction between two underlying physical phenomena. One is the expected swirling film that noticeably spreads radially upon exiting the injector. The other is a jet-like behavior of the liquid film where the radial spreading is weak. The DoE methodology utilizes space-filling properties,

such that design points in both regimes are simulated. This section explores how to efficiently incorporate this information into the CPOD methodology to refine prediction results.

Designs A and B (geometric parameters are listed in Table 3) are each arbitrarily chosen from among the simulated design points, as baseline geometry for determining off-design points. By offsetting injector parameters, we obtain two benchmark design points (denoted as red points in Fig. 13). Design A is classified with swirling behavior. Although Design B is classified with jet-like behavior in its developing stage, the flowfield transitions to a swirling flow in its stationary state. This trend may be an indicator that Design B is near the jet-swirl regime boundary. Its stationary state was used to classify this hybrid physics case.

A full design trade-off study requires quantifying how every parameter affects key performance metrics. Hence, all injector variables are retained for the first benchmark, E. The second benchmark, F, only varies design parameters with significant effects on the liquid-film response. The corresponding geometries are shown in Table 4. For Benchmark E, each design parameter deviates +10% from that of Design A. With normalized parameters, the distance traversed in the design space is estimated to be about 18.1%, as calculated in the L_2 linear sense.

Table 4. Injector geometries for benchmark cases.

Benchmark	L (mm)	R_n(mm)	θ (°)	δ (mm)	ΔL (mm)
E	22.0	3.22	58.2	0.576	3.42
F	37.7	3.06	59.0	1.417	1.00

The sensitivity study showed that the injector radius and the injection location have less effect than the slot width and tangential inlet angle on the film thickness and spreading angle. They are thus fixed, and the other three parameters are offset from Design B by -10% to explore the design space at Benchmark F. The closest two simulation points are Designs C and D. The neighboring points are provided because Design B seems to be near the jet-swirl dichotomy.

The second component of the data-driven framework for the design survey is a decision tree [100, 101]. Figure 20 shows the decision-tree splitting process, indicating how the algorithm decides the way an injector parameter dictates whether the flow is jet-like or swirling. The initial decision between the two behaviors is achieved by assessing the extent to which the liquid film spreads radially from the injector exit. The numeric outputs are essentially binary flags between the two subgroup classifications. For example, the first numeric output, $\theta < 60.02°$, splits the dataset into 11 jet-like and 19 swirl cases. The decision tree then further classifies the data according to the injector inlet and radius. Intuitively, when the tangential inlet angle, θ, is smaller, there is less azimuthal momentum in the liquid film to cause radial spreading. When the injector inlet, δ, becomes large, the decreased momentum results in jet-like behavior. The decision tree quantifies these effects and predicts a jet-like injector with $\theta < 60.02°$ and $\delta > 1.40$ mm. Following the previous two criteria, if the tangential inlet angle is large enough, that is, $\theta > 49.24°$, the injector retains swirling behavior.

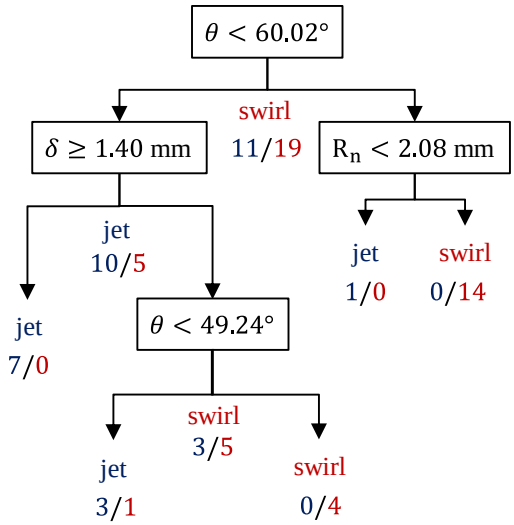

Figure 20. Decision tree splitting process with numeric classifiers.

The two benchmark cases are used to verify the decision tree. With such an algorithm, simulation results can be predicted using the model with proper training data. As the next section will further detail, the emulator relies upon the set of common basis functions extracted from the dataset. With two different types of underlying coherent structures, the two datasets should be trained separately to predict design parameter sets that lead to their corresponding flow behavior.

3.5.3 Surrogate Model

In order to train an emulator and make predictions, a set of common basis functions must be utilized, as previously mentioned. Figure 21 shows the process of generating the common grid. The red lines partition the axisymmetric domain for each case into five regions: injector headend region, injector interior, and three sub-regions downstream of the injector. The densest grid system among the 30 training cases is selected as the common grid, upon which the partitioned regions for all other cases are then scaled to the

corresponding regions in the common grid. This scaling is designed such that the ensuing model is able to leverage common basis functions, without significantly changing the flow features of interests. It should be noted the scaling has marginal impact upon liquid film development visualization within the injector, which has the broadest range among the design parameters. The original data is interpolated with an inverse distance weighting interpolation method using the ten nearest neighborhood points, to retain the fine points in regions of interest, specifically near the liquid film. The results on the common grid are used for POD analysis.

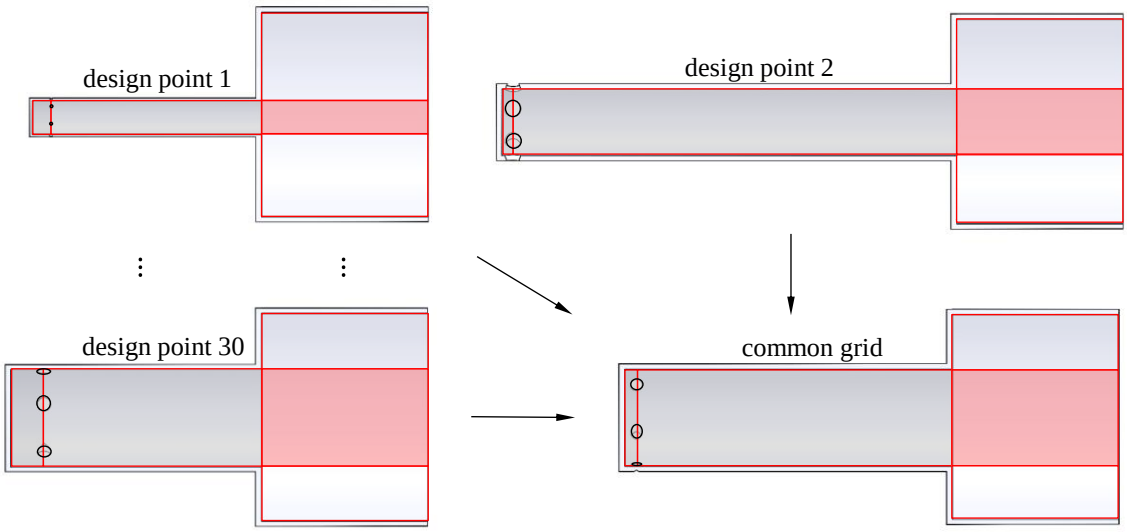

Figure 21. Schematic of common grid generation process.

Figure 22 shows the energy spectrum of the azimuthal velocity captured by the CPOD analysis. This spectrum is chosen as a demonstrative example, as the overall behavior is shared by all other physical variables. 45 CPOD modes are required to retain 99% of the energy and limit the corresponding truncation error for the reconstruction. The leading two modes are presented in Fig. 23, both indicating swirling flow structures with

dominant fluctuations near the injector wall. The flow evolution within the injector and subsequent liquid-film development downstream of the exit are clearly observed.

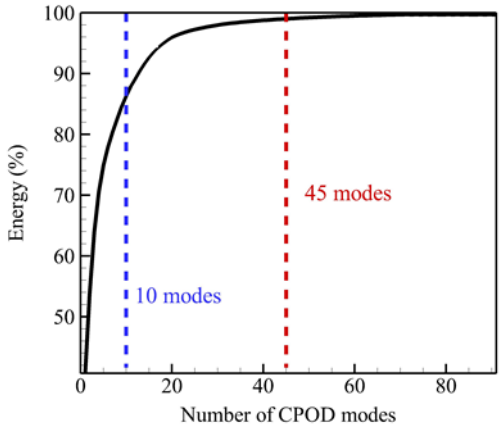

Figure 22. Energy spectrum of CPOD modes for azimuthal velocity component for Benchmark E.

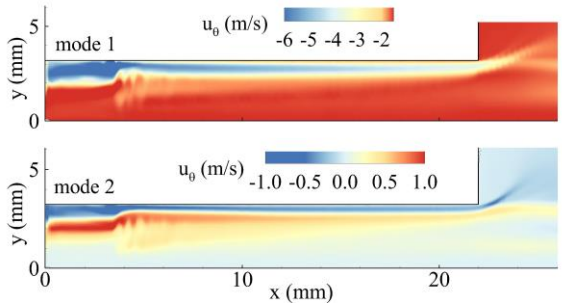

Figure 23. First two CPOD modes of azimuthal velocity for Benchmark E.

The kriging of time-varying coefficients combined with the CPOD modes allows for emulation of the spatio-temporal evolving flow at a new design point. The CPOD modes represent the common physics extracted from the training dataset. A new injector geometry is assumed to produce similar flow physics, including a hollow gas core, a swirling liquid film attached to the wall, and a conical liquid sheet spreading outward at

the injector exit. Figure 24 shows snapshots of the temperature field for the simulation and emulations of Benchmark E ($L = 22.0\,mm,\ R_n = 3.22\,mm, \theta = 58.2°, \delta = 0.576\,mm,$ and $\Delta L = 3.42\,mm$). For the temperature CPOD analysis, 2000 modes, out of the 30,000 modes that can be extracted, are required to capture 90% of the energy, and are used for the prediction. Good agreement is obtained, illustrating the same qualitative trends for the flow structures, with a liquid film along the injector wall and a center recirculating flow downstream of injector.

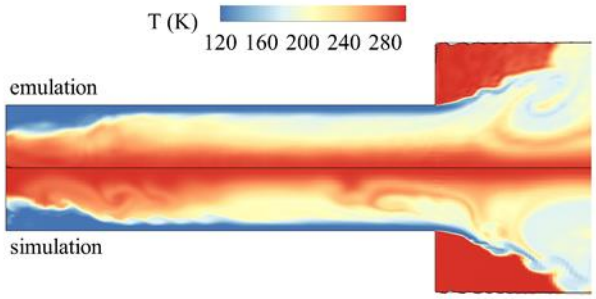

Figure 24. Comparison of instantaneous temperature distribution for Benchmark E.

POD analysis can be interpreted as a spatial averaging technique using the covariance matrix of the flow variable of interest. Some flow details, such as the surface wave propagation of the liquid film, may be smoothed out due to averaging. This concern can be addressed effectively using the aforementioned statistical and optimization algorithms to tune GP model parameters. The resultant emulator model thus mitigates the smoothing effects and captures the flow structures well.

3.5.3.1 Response Performance Metrics

As a preliminary comparison, a kriging surrogate model was applied to the extracted liquid-film thickness and spreading angle at the injector exit. The training process was implemented for the 30-case dataset. The following discussion is based on benchmark E: a swirl case. The liquid-film thickness is estimated, based on hydrodynamic theories, to be 0.618 mm, and the spreading angle 91.8°. The single-point emulator predicts a liquid-film thickness of 0.520 mm and a spreading angle of 99.0°. The data are compared with the simulation results of 0.430 mm and 103°, respectively. The surrogate model can also be used to find the design geometry for a specified performance measurement, such as a specific liquid film thickness and spreading angle. With the trained regression model, the corresponding response can be predicted for a set of given parameters. On the other hand, for a specific response, an inference can be made about the new set of parameters. The relationship is determined from a calibration dataset, and the new parameter set can be solved for through the regression model, similar to identifying a set of input rate configurations acceptable for a network queueing system [108]. The chosen initial points for the solver lead to convergence to the candidate injector configuration that would produce the desired responses. This provides an array of design geometries that can be further narrowed with more performance measurements or analysis of flow dynamics. With specified constraints, an optimal configuration can be acquired. For example, if a liquid film thickness of 0.60 mm and spreading angle of 42.5° was desired for a first-stage engine injector longer than 50 mm and tangential inlet less than 1.50 mm, the best candidate injector would have the dimensions $L = 80.21$, $R_n = 2.52$, $\theta = 62.43°$, $\delta = 1.16\,mm$, and $\Delta L = 1.88\,mm$.

Figure 25 shows the variation of the film thickness along the injector wall.

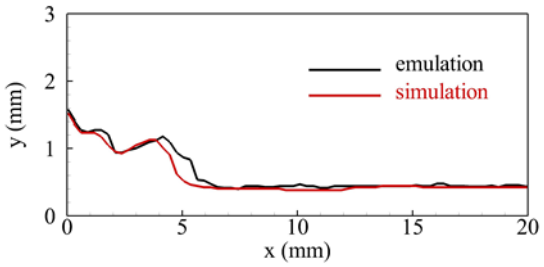

Figure 25. Comparison of mean liquid-film thickness along axial distance.

At the injector exit, the time-averaged film thickness and spreading angle predicted by the kriging surrogate model are 0.420 mm and 107°, corresponding to percentage errors of 2.38% and 3.88% respectively. The model matches the simulation in terms of key features such as the liquid-film distribution and spreading angle, performance measures needed for assessing injector design.

For Benchmark F, the baseline case (Design B) develops from jet-like to swirling behavior, as shown in Fig. 26. The design parameters are near a critical hyperplane separating different flow features.

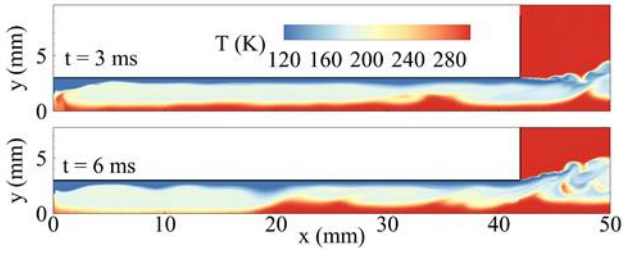

Figure 26. Time evolution of the temperature for baseline case for Benchmark F.

Figure 27 shows the time-mean temperature distributions for the two benchmark cases. The accumulation of liquid propellant at the injector headend is observed in both results. The liquid-film thickness and spreading angle match well. For benchmark case F, which produces a jet-like flow, a standing wave appears in the upstream portion of the injector. The emulation result captures the wavy structure only to some extent. In the downstream region, the liquid-film thickness and spreading angle are better predicted. In the region where the film breaks apart, less propellant appears in the simulation result.

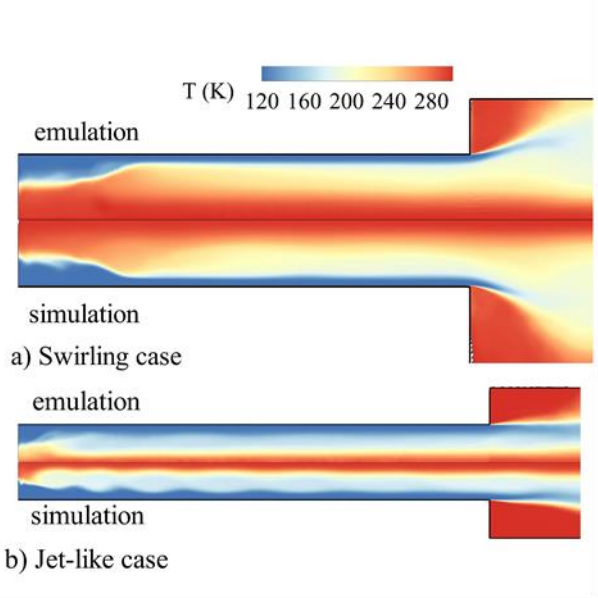

Figure 27. Mean temperature distributions for benchmark cases a) swirl-like case and b) jet-like case.

3.5.3.2 Root-mean-square Relative Error

The root-mean-square-relative error (RMSRE) is defined by

$$RMSRE(t;S) = \frac{[\int_S \{f(\boldsymbol{x},t;\boldsymbol{c}_{new}) - \hat{f}(\boldsymbol{x},t;\boldsymbol{c}_{new})\}^2 d\boldsymbol{x}/|S|\,]^{1/2}}{\max\big(f(\boldsymbol{x},t;\boldsymbol{c}_{new})\big) - \min(f(\boldsymbol{x},t;\boldsymbol{c}_{new}))} \times 100\% \quad (3.18)$$

where S is the desired region, $|S|$ the number of gridpoints under S, $f(\boldsymbol{x}, t; \boldsymbol{c}_{new})$ the simulated flowfield at geometry $\boldsymbol{c}_{new}$, $\hat{f}(\boldsymbol{x}, t; \boldsymbol{c}_{new})$ the emulated flowfield, and $\max\big(f(\boldsymbol{x}, t; \boldsymbol{c}_{new})\big)$ and $\min\big(f(\boldsymbol{x}, t; \boldsymbol{c}_{new})\big)$ the maximum and minimum values of $f(\boldsymbol{x}, t; \boldsymbol{c}_{new})$ over $\boldsymbol{x}$, respectively.

Table 5 lists the RMSRE for the two benchmark cases. This quantitatively compares the simulation and emulation shown in Fig. 27, illustrating minor discrepancies near the injector wall. For the jet-like case, the error is reduced if only the upstream results (that is, upstream of the injector exit) are considered.

Table 5. RMSRE of temperature distribution.

Benchmark	Overall	Upstream	Downstream
E (swirl)	5.18%	6.62%	3.10%
F (jet-like)	8.65%	8.30%	9.03%

Figure 28 shows the time-mean temperature distribution in the radial direction at various axial locations for Benchmark E. The high gradient region represents the transition between the liquid film and the gas core. There is a slight deviation in this transition region, where the simulated temperature gradient is sharper than that of the emulation. Similar results, not shown, are also obtained for Benchmark F.

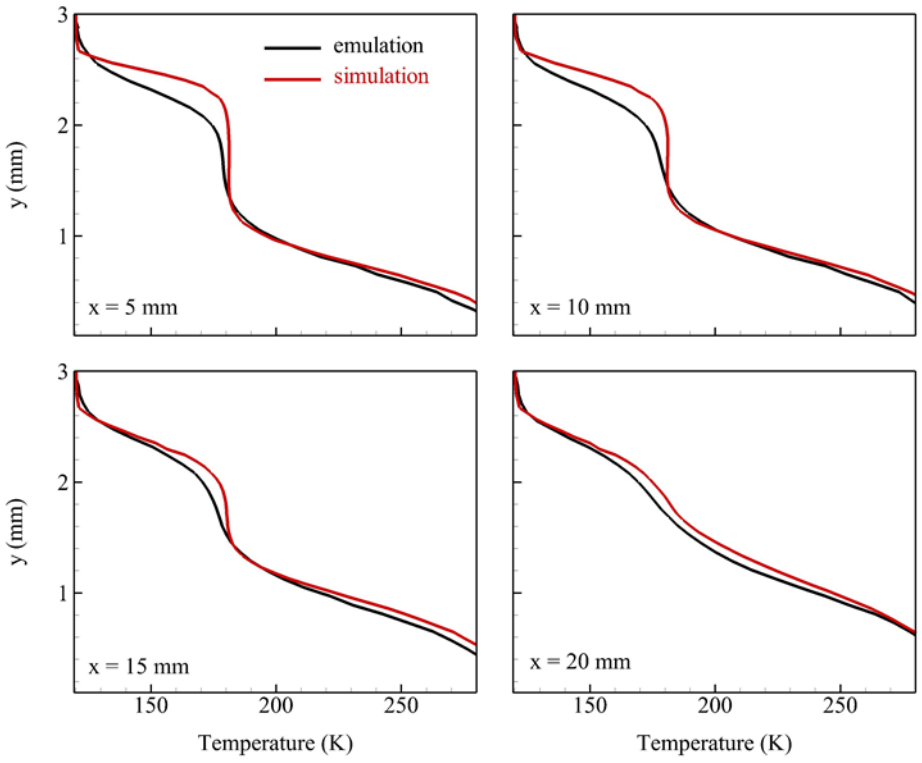

Figure 28. Mean temperature distribution in radial direction for Benchmark E.

To illustrate the importance of incorporating the decision tree within the framework, a comparison is made with a prediction from an emulator without dataset classification [66]. Table 6 lists the RMSRE for the two benchmark cases using the emulator trained with the entire dataset. The Benchmark E results are slightly worse, and Benchmark F's prediction is significantly off.

Table 6. RMSRE temperature distribution results (without dataset classification)

Benchmark	Overall	Upstream	Downstream
E (swirl)	5.93%	6.70%	5.09%
F (jet)	13.2%	7.43%	17.7%

Next, axial velocity is used as training data, demonstrating the capability of modeling other flowfield variables. Figure 29 shows the time-mean distribution comparison between the simulation and emulation for Benchmark E. The key flow features, such as the gaseous core and swirling film, are predicted well. The RMSRE listed in Table 7 numerically outperforms temperature results. This improvement can be explained by the broader range, which leads to higher errors.

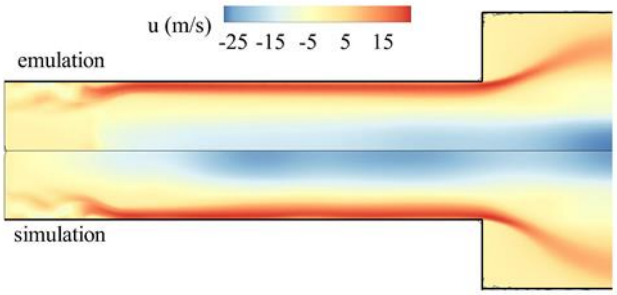

Figure 29. Mean axial velocity distribution for Benchmark E.

Table 7. RMSRE velocity distribution results.

Benchmark	Overall	Upstream	Downstream
E (swirl)	4.12%	4.58%	3.64%
F (jet)	3.97%	4.71%	2.85%

Figure 30 shows the time-mean axial velocity distribution in the radial direction for various axial locations in the injector for Benchmark E. The transition region is matched, although there is a deviation near the injector centerline, where the gradient is smoother in the emulator prediction. Similar results, not shown, were seen for Benchmark F.

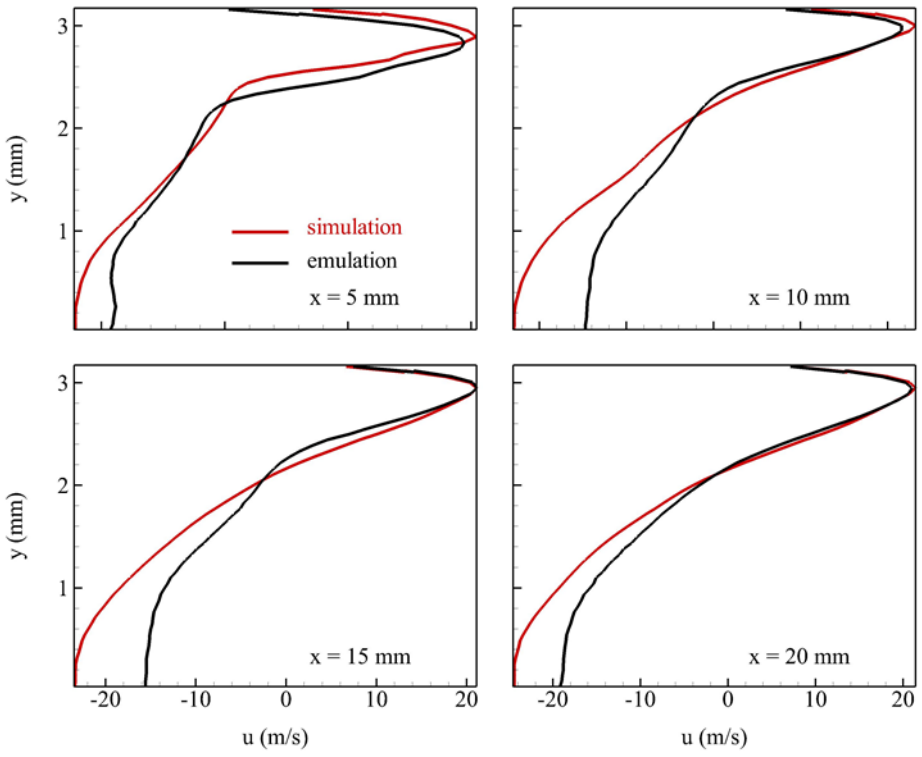

Figure 30. Mean axial variation of velocity distribution in the radial direction for Benchmark E.

3.5.3.3 Injector Dynamics

Injector dynamics involve downstream pressure fluctuations causing pressure drop oscillations across the liquid film. These changes in turn trigger mass flow rate variations across the tangential inlets [9, 10], over a wide range of time scales. A spectral analysis can quantify these oscillations and capture the periodicity of flow features. Mathematically, the PSD can be interpreted as the Fourier transform of the autocorrelation function for a signal.

Figure 31 shows the position of pressure probes in the fluid transition region. The probes are located near the film surface to measure pressure fluctuations.

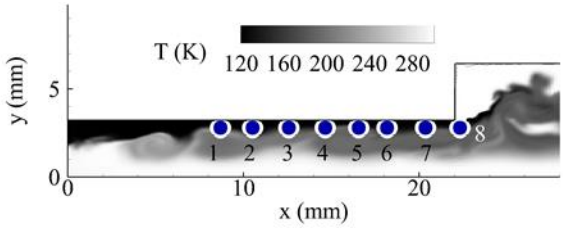

Figure 31. Probe positions along liquid film surface.

The pressure PSDs are calculated for both the simulation and emulation results. Figure 32 shows the PSD of probes 1, 3, 5, and 7; the frequency content is observed to be well quantified.

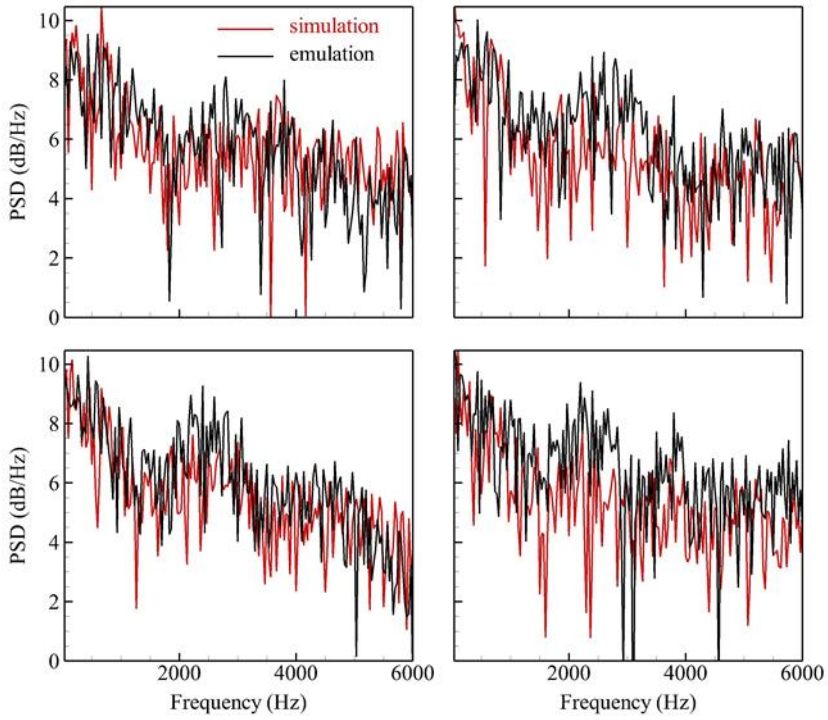

Figure 32. PSD results of pressure fluctuations for probes 1, 3, 5, and 7.

The high-frequency oscillations that are typically present in swirl injectors with a vortex chamber are not prominent. Most of the signal is comprised of low-frequency content, representing surface wave propagation along the film. In addition, acoustic waves propagate, couple and interact with hydrodynamic waves, appearing as several different frequencies. The simulated and emulated probes show similar dynamics, such that the peak frequencies of the simulation and emulation results match. However, the emulator amplifies the dominant frequencies, as the kriging model may be overfitting slightly due to insufficient data. Despite this signal strengthening phenomenon, the analysis displays an ability to model flow dynamics, properly capturing the simulated periodic oscillations. Downstream of the injector exit, the dynamics become more broadband and no dominant oscillations appear, because there exist strong interactions between the shear layer and recirculation zone generated from vortex breakdown.

3.5.3.4 Uncertainty Quantification

In addition to the aforementioned validation methods, the emulator model also allows for quantification of predictive uncertainty, which can be used to define confidence intervals for model fit. Moreover, these uncertainties can be linked to dynamic flow physics. As an example, the spatial uncertainty quantification (UQ) is shown in Fig. 33, displaying the one-sided width of the 80% confidence interval (CI) for pressure and temperature (a derivation of this interval is found in [66]). The uncertain areas, in the time-mean temperature distribution, correspond to the most dynamic sections of the liquid transition region. The downstream uncertainty is caused by the recirculation induced through vortex breakdown.

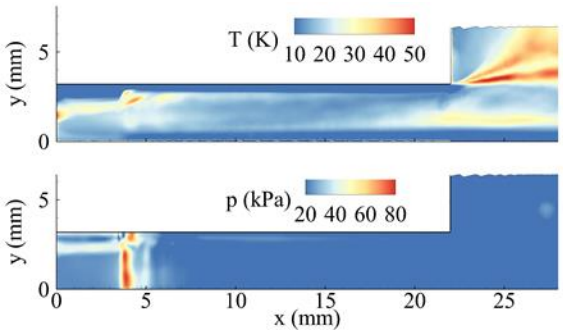

Figure 33. One-sided width of the 80% confidence interval for Benchmark E: temperature and pressure predictions.

3.5.3.5 Computation Time

Figure 34 presents the simulation and emulation timeline. The computation times are calculated based on performance for a parallelized system of 200 Intel Xeon E5-2603 1.80 GHz processors. A total of 900,000 CPU hours is required for the 30 GB dataset. CPOD extraction and parameter estimation for the model takes about 45 minutes.

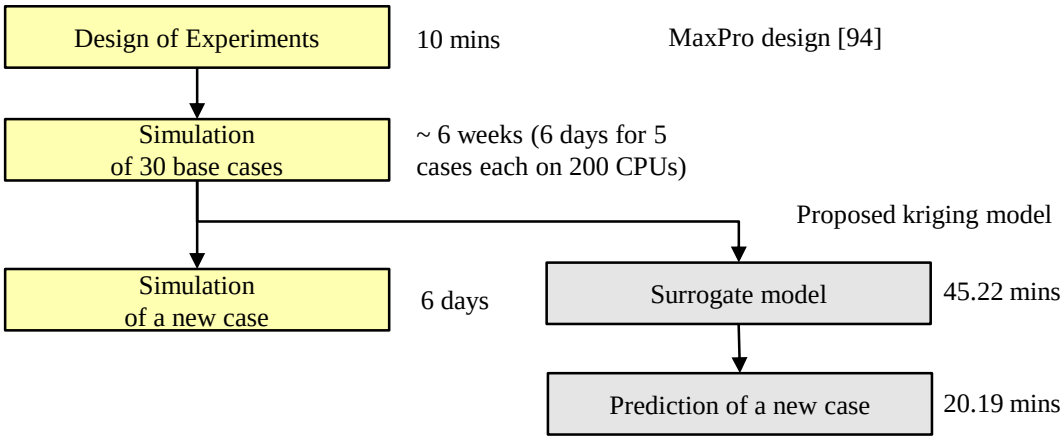

Figure 34. Simulation and emulation timeline.

The parallelized predictions from the developed model only need around 30 CPU hours, significantly reducing the turn-around time as compared with LES simulations requiring

30,000 CPU hours. This improved computational efficiency is crucial, as it enables quick design iterations. The existing spatio-temporal emulators mentioned in the introduction require much more computation time to fit the underlying statistical model, because the training dataset of each simulation is too large to directly manipulate [71]. By carefully using physical knowledge to make informed model assumptions, state-of-the-art machine learning techniques have been leveraged to develop a methodology offering an efficient strategy to survey the design space.

3.6 Conclusion

The present work develops an integrated framework that incorporates state-of-the-art statistical methods, machine learning algorithms, and a physics-driven data reduction method to obtain a surrogate model for a broad-range design space. Taking a swirl injector as an example, the CPOD-based emulation framework is used to extract the flow physics, reduce the data, and build an efficient, physics-driven emulator.

The key contributions are two-fold: the use of statistical and machine learning techniques to quantify the impact of design parameters on important flow physics, and the incorporation of such methods with physics-guided model assumptions to build an efficient surrogate model for flowfield prediction. A vital model assumption is that the CPOD, the common basis, accurately retains the rich set of physics over varying geometries. This model successfully captured the simulation results and fared better than analytical estimations for performance measures. The emulated flowfield is validated against the LES-simulated flowfield to demonstrate how the flow features and injector characteristics are preserved by the model. Moreover, this methodology significantly reduces the

computational time required for assessing a design based on spatio-temporal information. While the focus of the present study is on a data-driven analysis and emulation of flow physics, the principle of applying machine learning techniques with physics-guided assumptions can be applied to any type of engineering application.

CHAPTER 4. COMBUSTION RESPONSE

Combustion instability is of utmost importance in all combustion devices because of its destructive potential, but especially in high-pressure combustion chambers of rocket engines. There is a need to characterize the complex nature of combustion dynamics to advance engine design methodologies. Traditional strategies of mitigating combustion instabilities focus on increasing the damping of the system and/or reducing the coupling between unsteady combustion responses and periodic flow oscillations [17]. Instabilities can develop from small perturbations in the combustion process, which interact with acoustic modes of the chamber [109], as illustrated in Fig. 35.

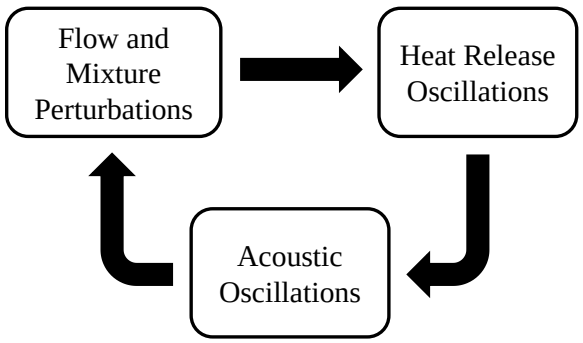

Figure 35. Combustion instability feedback process [109].

If the unsteady heat release oscillations are in phase with the acoustic oscillations, the fluctuations typically grow toward a limit cycle amplitude. Rayleigh [110] indicated that the sign of the product of the pressure fluctuations and unsteady heat release rate, integrated over a period of oscillations, can define the stability of the system. Understanding the relationship between pressure and heat release established the fundamental understanding of combustion dynamics. The instability increases the

structural and thermal loading within a combustor, shortening the engine lifespan. Major stability issues were, for example, encountered in the F-1 engine development program, as reviewed by Oefelein and Yang [17]. Project First tackled the major undertaking of eliminating these issues in the F-1 engine; over 2000 full-scale tests (62.5% of all F-1 full-scale development tests) were conducted during that program, to evaluate injector designs and baffle arrangements aimed at mitigating harmful combustion dynamics.

Comprehensive combustion stability analysis has long been sought after, as *a priori* understanding of the coupling mechanisms would greatly reduce the number of tests and capital required for developing new engines. A key component of the stability analysis is the quantification of the combustion response. Instability is linked with time delays inherent to the combustion process, which led to the rise of the sensitive time lag theory, most notably established by Crocco [111, 112]. In this theoretical framework, the dependence of the unsteady heat release rate is quantified with an interaction index n and time delay τ upon the state variables involved. Unfortunately, these two parameters are not known *a priori*, so the model only provides a global description of the underlying physical processes driving unstable combustion. NASA report SP-194 edited by Harrje [113] documents key parameters that influence the onset of combustion instabilities in liquid rocket engines, such as the geometry of the thrust chamber, the evaporation rate of propellant droplets [114], and the pressure loss through the injectors, which governs the coupling with the feed system [115]. The prediction of combustion instability is also sensitive to changes such as injector geometry and variations in operating conditions [116], increasing the need for a robust methodology to quantify the underlying physical mechanisms.

To reiterate, there is a necessity to identify and quantify the physical mechanisms occurring over multiple time and length scales involved in combustion dynamics. The proposed methodology leverages high-fidelity large eddy simulation in combination with machine-learning techniques to quantify the distributed combustion response. The outcome is intended to serve as an acoustic source term in the generalized wave equation, which can analyze the stability of complex propulsion systems. This chapter is organized as follows: Section 1 summarizes the high-fidelity theoretical formulation and numerical methods, and presents the injector configuration and subject dataset; Section 2 summarizes the stability analysis framework based on the generalized wave equation; Section 3 introduces combustion response data analysis methodology; Section 4 presents the results and discussions for the extracted combustion response; Section 5 draws conclusions about the machine-learning-based data analysis of combustion response, and discusses future work.

4.1 High-fidelity Simulations

LES codes have long been used to investigate combustion dynamics [117-119]. In order to properly quantify a combustion response, the underlying flow and mixing behaviors at supercritical conditions must be captured before any data analysis can be performed. The present work utilizes data generated from GCLSC injectors [120-122] similar to those of the RD-170 engine. The RD-170 ORSC engine [30] was precursor to the RD-180, which is used for the Atlas V launch vehicle.

4.1.1 Theoretical Formulation and Numerical Method

An integrated theoretical and numerical framework is established and implemented, to treat supercritical fluid flows and combustion over a broad range of fluid thermodynamic

states [91, 92, 118]. Turbulence closure is achieved using LES. Thermodynamic properties are evaluated by fundamental thermodynamics theories in accordance with the modified Soave–Redlich–Kwong equation of state. Transport properties are estimated using extended corresponding-state principles [118]. The numerical scheme is a density-based, finite-volume methodology, along with a dual-time-step integration technique. The overall algorithm is self-consistent and robust, with implementation of a preconditioning scheme and a detailed treatment of general fluid thermodynamics [91, 92].

Owing to the demanding computational requirements of three-dimensional simulations, only a cylindrical sector with periodic boundary conditions in the azimuthal direction is simulated. As the simulation data is limited to a single injector, the analysis focus is the behavior within and in the downstream region of the injector simulation. The azimuthal flow dynamics and inter-element interaction is not the primary concern, as the emphasis is on developing a data-driven methodology that captures the distributed response. A multi-block domain decomposition technique, combined with a message passing interface for parallel computing, is applied to improve computational efficiency.

4.1.2 Configuration and Dataset

Figure 36 shows the GCLSC injector of concern, reproduced from patent filed by Vasin et al. [31]. The injector consists of four parts: gas jet, liquid swirler, recess region, and taper region. GOx is injected axially into the inner jet, while liquid kerosene is introduced tangentially through the coaxial swirler. The mixing of GOx and kerosene is initiated just downstream of the GOx post and intensifies in the taper and downstream regions. The dimensions of the injector are listed in Table 8. The recess length has been

shown in previous studies [22, 23, 37, 120-122] to have significant effects on the mixing characteristics for injectors. In the current work, three cases with different recess lengths (L_r) are considered in a range of 0-16 mm, that is, 16.0, 10.5, and 0.0 mm, to explore combustion response. As the total axial length of the annulus upper surface is fixed at 16 mm, the length of the annulus lower surface changes (shielding, L_s) accordingly with the recess length. The case with a recess length of 10.5 mm is the baseline, while the other two provide the extremes of no recess region and full recession.

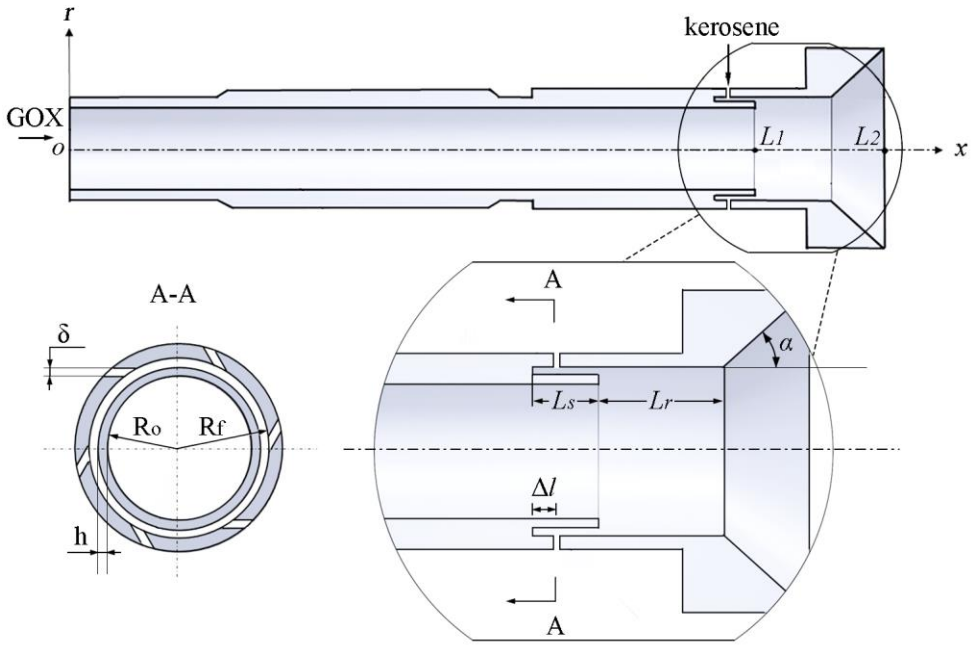

Figure 36. GCLSC injector schematic.

Table 8. Dimensions

δ	h	R_O	R_f	L_1	L_2	L_f	L_r	Δl	α
0.66mm	5.76mm	5.62mm	7.03mm	93mm	113.1mm	5.5mm	10.5mm	2mm	42°

In order to isolate the effect of recess length, the operating conditions for all cases are identical, as listed in Table 9. It should be noted that these operating conditions reflect those of the RD-170 engine [30]. $\dot{m}_o$ and $\dot{m}_f$ represent the injection mass flow rates of oxidizer and fuel, respectively. $T_{in,o}$, $T_{in,f}$, and p_a denote the oxidizer injection temperature, fuel injection temperature, and ambient pressure, respectively.

Table 9. Operating conditions.

$\dot{m}_o$ (kg/s)	$\dot{m}_f$ (kg/s)	$T_{in,o}$ (K)	$T_{in,f}$ (K)	p_a (bar)
1.33	0.477	687.7	492.2	252.96

The computational domain consists of the injector interior ($18R_g$ in axial direction) and a downstream region ($25R_g$ and $7R_g$ in the axial and radial directions, respectively). No-slip and adiabatic boundary conditions are applied at the injector walls. An acoustically non-reflecting boundary condition [123] is implemented at the inlet of the inner jet. The downstream boundary in both axial and azimuthal directions is treated by a sponge-layer method [124]. A reference pressure is applied to preserve the average pressure in the computational domain. Figure 37 shows the unsteady heat release distribution and pressure flowfield in an instantaneous snapshot of the baseline case. The flame is stabilized at the GOx post tip and the shear flow produced from the mixing of swirling liquid and hot gas distorts the flame. The difference in scale of unsteady heat release and pressure should be noted, as this impacts the data analysis below.

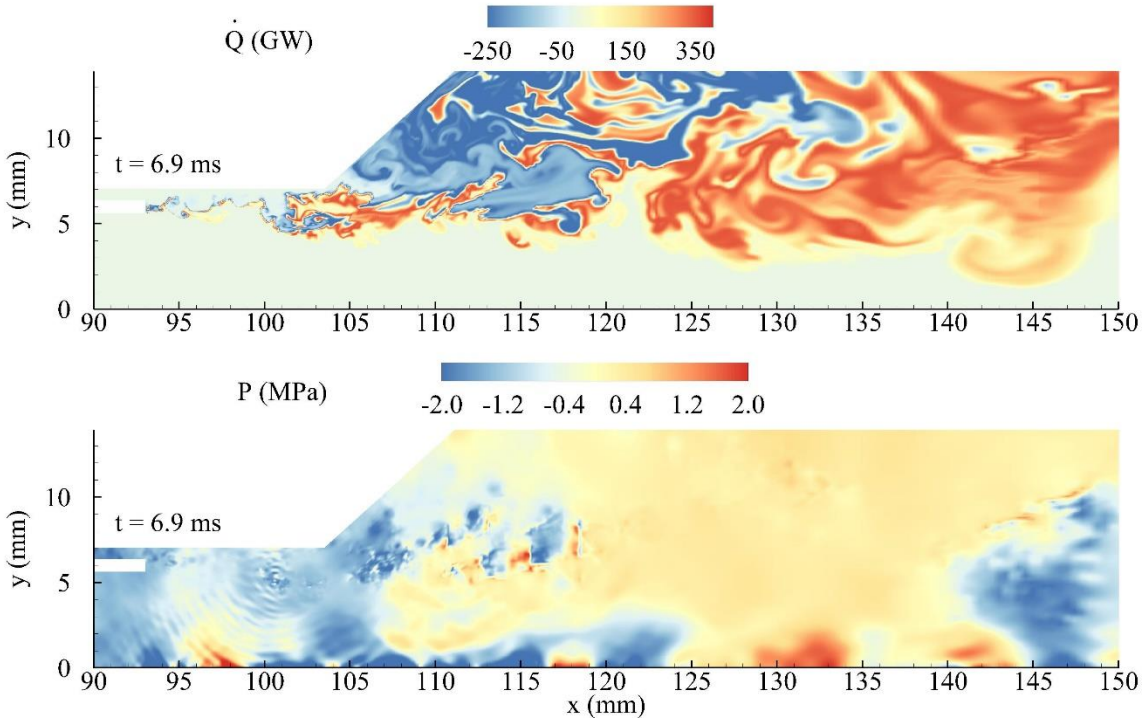

Figure 37. Instantaneous snapshot of baseline case in region of interest at 6.9 ms: (top) heat release, (bottom) pressure

4.2 Thermoacoustic Stability Analysis Framework

4.2.1 System Stability and Eigenmode Analysis

Several authors have proposed different approaches to modeling the thermoacoustic interaction between acoustic pressure oscillations and flame heat release fluctuations. Low-order models [119, 125-128] define the combustor system as a series of subsystems using mathematical transfer function matrices to connect these lumped acoustic elements. The main drawback of this approach is that the geometric details of the combustor cannot be entirely accounted for, and only the first "equivalent" longitudinal or orthoradial modes are extracted and analyzed.

In comparison, an analysis of the entire combustion chamber and injector head assembly can be conducted using LES and an acoustics solver [129-134]. Giauque et al. [132] demonstrated the potential of LES simulations, and obtained a mapping of combustion phase and response amplitude. Nicoud et al. [134] analyzed the combustion chamber using LES-extracted local fields of interaction index and time delay. With the extracted flame model, an eigenmode analysis evaluates and determines the eigenfrequencies (also known as natural frequencies) and the mode shapes of the system. The mode shapes play a pivotal role in determining combustion stability. In the past, the acoustic mode shapes in a baffled combustor were studied [18], and various damping enhancement control methodologies were investigated to mitigate system-level combustion instabilities. The main acoustic modes of concern in the main combustion chamber are typically the first and second tangential modes (1T and 2T), which were heavily investigated during the RD-170 injector head development [15]. When the combustion process excites the acoustic modes of the combustor, the system can become unstable, leading to hardware failure.

Recently, a reduced-scale rocket engine operated by Deutsches Zentrum für Luft (DLR) was investigated through a similar framework [135]. A 3D Fourier analysis was conducted on a configuration with 42 coaxial injectors, and the first transverse and radial acoustic modes of chamber were identified based on the dominant frequencies. Although the combustion response was mapped through a volume integrated Rayleigh index based on the extracted modes, the combustion response information was not incorporated back into an acoustic analysis to close the formulation.

The mathematical framework for acoustics analysis developed by Culick and Yang [136] is reviewed in the Appendix. The solution is suited for an iterative procedure constructed by introducing a Green's function, where the unperturbed problem defines the normal modes. With proper interpretation and appropriate modeling of the sources, this representation of the combustion dynamics can be applicable to all propulsion systems. The techniques used for the analyses are normal mode expansion, spatial averaging, and boundary matching. This framework is capable of including the unsteady combustion response, a vital acoustic source term, into the stability analysis for the entire combustion chamber. A common method of incorporating this effect is a Flame Transfer Function (FTF), which describes the ratio of the magnitude of unsteady heat release to incident flow perturbations as a function of frequency. For example:

$$F_p(\omega) = \frac{\dot{Q}'(\omega)/\bar{\dot{Q}}}{p'(\omega)/\bar{p}} \tag{4.1}$$

Fluctuations of unsteady heat release, $\dot{Q}'$, act as a monopole acoustic source term [137], and the resulting acoustic waves, p', are reflected by the combustor, which in turn modulates flow conditions at the flame. Some such models may be derived analytically, under the assumption that combustion takes place in the wrinkled flamelet regime, such that the flame is continuous and locally resembles a laminar flame that is merely convected by the flowfield. Indeed, such models now exist for premixed flames [138-140].

While these models may qualitatively capture much of the flame dynamics, their quantitative predictive power is limited in several ways; explicit solutions are typically only available for weakly wrinkled, laminar flames, and real flame effects such as gas

expansion are sometimes difficult or impossible to include. A typical explicit method is analyzing flame dynamics based on level-set approaches with the G-equation and inferring whether disturbances constructively or destructively interfere [140]. Experimental efforts have focused on characterizing the FTF, its gain and phase, according to the input amplitude level [141]. An underlying assumption for the flame describing function (FDF) is that the power contained in the other components of the spectrum of light emission and velocity fluctuation signals is not taken into account, because it is assumed that harmonics do not effectively determine the self-sustained oscillation mechanism [142]. The designation FDF can be interpreted as the collection of FTFs for various input levels and frequencies. Through this approach, the net combustion response from axial acoustic perturbations and azimuthal velocity perturbations has been investigated, quantifying the effects of shedding vortices and unsteady flame stabilization [143, 144]. It should be noted that these studies only quantified the global combustion response behavior, as the FTF relationship was developed with respect to volumetric heat release.

The current study proposes a comprehensive distributed FTF capable of being incorporated into an acoustic model, a Green's function extracted from numerical simulations. The mathematical development of a simplified $n-\tau$ combustion response model [119, 145] is described to illustrate the formulation of the combustion stability analysis next.

Following the same approach as given in Culick et al. [136], the formulation begins with the two-phase flow conservation equations in conservative form. The conservation equations are transformed into a single-phase form that includes the effects of condensed species. Then, the nonlinear wave equation can be derived, by manipulating the outcome

results when the dependent variables are split into mean and fluctuating components. Appealing to the definitions for the source term group $\mathcal{P}'$ from the Appendix and Culick and Yang [136], the wave equation may be expressed solely in terms of the unsteady heat release $\dot{Q}'$

$$\frac{1}{\bar{a}^2}\frac{\partial^2 p'}{\partial t^2} - \nabla^2 p' = -\frac{\bar{\gamma}-1}{\bar{a}^2}\frac{\partial \dot{Q}'}{\partial t} \tag{4.2}$$

where $\dot{Q}'$ refers to unsteady heat release per unit volume. Assuming that the pressure and heat release oscillate harmonically as $e^{i\omega t}$, this equation may be expressed in the frequency domain as

$$\frac{-\omega^2}{\bar{a}^2}\hat{p} - \nabla^2 \hat{p} = -i\omega\frac{\bar{\gamma}-1}{\bar{a}^2}\hat{\dot{Q}} \tag{4.3}$$

In general the unsteady heat release may be due to any number of perturbations incident on the combustion zone, such as pressure, velocity, and/or local reactant composition. Consider a simple velocity-coupled $n-\tau$ model,

$$\frac{\dot{Q}'(t)}{\bar{\dot{Q}}} = n\frac{u'(t-\tau)}{\bar{a}} \qquad \Rightarrow \qquad \frac{\hat{\dot{Q}}}{\bar{\dot{Q}}} = ne^{-i\omega\tau}\frac{\hat{u}}{\bar{a}} \tag{4.4}$$

where the speed of sound has been used as the reference speed instead of the mean flow velocity to avoid the singularity when there is no mean flow. Now, the acoustic velocity may be related to the acoustic pressure by the linearized momentum equation:

$$\boldsymbol{u}' = -\int \nabla p' \, dt \qquad \Rightarrow \qquad \hat{\boldsymbol{u}} = -\frac{1}{i\omega}\nabla\hat{p} \tag{4.5}$$

where the velocity has been left as a vector quantity. The scalar pressure Eq. (4.3) cannot take vector source terms; to remedy this it is assumed that the combustion is sensitive only to the axial fluctuation in acoustic velocity, so that Eq. (4.3) becomes finally

$$\frac{-\omega^2}{\bar{a}^2}\hat{p} - \nabla^2\hat{p} = n\frac{\bar{\gamma}-1}{\bar{\rho}\bar{a}^2}\frac{\bar{\dot{Q}}}{\bar{a}}e^{-i\omega\tau}\frac{\partial\hat{p}}{\partial x} \tag{4.6}$$

Similarly, for a purely pressure-coupled response there ultimately results

$$\frac{-\omega^2}{\bar{a}^2}\hat{p} - \nabla^2\hat{p} = -ni\omega\frac{\bar{\gamma}-1}{\bar{a}^2}\frac{\bar{\dot{Q}}}{\bar{p}}e^{-i\omega\tau}\hat{p} \tag{4.7}$$

The right hand side of the foregoing equations may be treated as a forcing term defined over some volume. Taking a step back from this example, the key component of this solution procedure is quantifying the acoustic source term and constructing the Green's function for the simplified form of wave equation:

$$(k^2 - \nabla^2)\hat{p} = h(x,\hat{p}) \tag{4.8}$$

where $h(x,\hat{p})$ represents fluctuations in energy release and gasdynamic effects that drive pressure waves [136]. Green's function relates the source term on the right hand side to the acoustic pressure distribution governed by the inhomogeneous wave equation. This is, in fact, the FTF. For a single-input single-output (SISO) system, signal processing and control

theory typically generates the transfer function, H, from the cross-correlation and autocorrelation information [146]:

$$H(\omega) = S_{xy}(\omega)/S_{xx}(\omega) \tag{4.9}$$

where S_{xy} represents the cross-spectral density between the input and output signal and and S_{xx} represents the autospectral density of the input signal. Keeping in mind these represent the Fourier transform of the cross-correlation and autocorrelation of the signals, it is evident that the transfer function relies on data correlation analysis. While this is a powerful tool, it should be noted this correlation analysis is restricted by the data quality; a generalized model approach taking into account of sparsity and multicollinearity may yield better results.

In reality, the combustion zone will consist of numerous flames, possibly interacting with one another, and the combustion zone in the aggregate will be spatially nonuniform. Thus, it is important to incorporate the spatial distribution of combustion response. For a diffusion flame, such as that formed between the fuel and oxidizer streams of most rocket injectors, the high temperature regions begin near the origin of the shear layer, because this is where the flame stabilizes [122]. The unsteady heat release is follows a similar distribution. If the time delay is identified with a characteristic convection time, then it should be expected to scale roughly as $\tau \sim x/U$. Practical experience in the design of combustion chambers [15, 113] suggests that increasing the axial distribution of combustion tends to make the system more stable, and this implies that an increasing convective time lag also stabilizes the system. However, this time scale is not the only

relevant time scale affecting the combustion response, and a more generalized approach is the objective of the current study.

4.2.2 Identification and Quantification of Combustion Response

The previous section highlighted a critical ingredient in quantifying combustion dynamics, the necessity of incorporating multiple time scales into the data analysis. The usage of system identification (SI) in state-feedback control techniques has been well established to account for different time scales within a system. Typical active control employed in combustion chambers monitors instantaneous combustion chamber conditions and provides inputs, such as injecting secondary fuel to damp pressure oscillations [145, 147]. Efforts have been made to design controllers that relied as little as possible on a particular combustion model, and an adaptive controller is employed to continuously update control parameters based on the engine conditions [148, 149]. It is important to note that these algorithms take into account a number of time delays in the system, such as actuator time delay, the spatial distribution of fuel injection, data acquisition times, signal processing times, or the dynamic response of the fuel injection mechanism. The time varying output of the SI, the controller output, is dependent not only on past and present values of key variables, but also past values of itself. The state-space representation of such data has proved useful in examining limit-cycle oscillations in a system, characterizing time series data through time-delay embedded methods [150]. The proposed model takes this technique one step further, identifying significant autoregressive processes and pinpointing the noise model. The model selection is a data-driven method of exploring the intrinsic dynamics within the system.

The application of numerically based SI was introduced by Polifke et al. for estimation of acoustic transfer matrices [151]. The approach demonstrates how a single time lag model can only yield correct stability predictions if the unstable eigenfrequency is known *a priori,* and displays a much richer description of the entire combustion response, as all characteristic timescales are reflected within the model. This study employs rational function approximations, with parameters estimated in terms of a nonlinear least squares problem. The identification process employs the Wiener-Hopf filter, a correlation-based methodology. Premixed flames were treated with this technique as a multiple-input, single-output (MISO) model, and a detailed analysis and physical interpretation of the response function was carried out [152, 153]. The identified FTF was for a swirl stabilized premixed burner with an axial swirl generator that had broadband excitation at the upstream inlet. These studies displayed the limitations of Wiener-Hopf inversion in the presence of noise. This data-driven approach can be treated as a "black box" method with a given set of inputs and outputs. Polifke describes the linear, time-invariant system identification process in detail, and explains the development of the framework from an impulse response to correlation-based response [154]. It should be noted that there is no model selection process for model parameters and the time lags are not obtained from the data. Instead, a few time lags are *a priori* specified according to convective transport and low frequency flame dynamics associated with recirculation.

Similar to the present work, numerically-based SI methodology has been applied to direct numerical simulation (DNS) data, and the extracted FTF was then utilized within a network model to characterize the intrinsic thermoacoustic instability, showing that laminar premixed flames responded predominantly to velocity perturbations [155]. This

approach was further improved to model the noise and forego the necessity for external excitation of the system. Parametric SI based on the Box-Jenkins model was employed in lieu of Wiener-Hopf and modeled the noise along with the acoustic transfer matrices [156]. This study found that the same noise model was captured for both the LES simulation with external acoustic excitation and without external acoustic excitation, increasing confidence of the transfer function capturing the intrinsic physical mechanisms driving unstable combustion.

The present study further extends this numerically-based SI framework with 1) incorporation of the spatial distribution utilizing POD, and 2) model selection based on multicollinearity and sparsity of the data, which provides a data-driven approach for exploring the intrinsic dynamics within the system.

4.3 Combustion Response Data Analysis

4.3.1 Proper Orthogonal Decomposition

POD [86, 87], which is also known as the Karhunen-Loeve decomposition or principle component analysis (PCA) [157], is a well-established technique for data reduction and feature extraction. For a given flow property $f(\boldsymbol{x}, t)$, the POD analysis can determine a set of orthogonal functions φ_j, such that the projection of f onto the first n functions,

$$\hat{f}(\boldsymbol{x}, t) = \bar{f}(\boldsymbol{x}) + \sum_{j=1}^{n} a_j(t)\varphi_j(x) \tag{4.10}$$

has the smallest error, defined as $E\left(\left\|f-\hat{f}\right\|^2\right)$. Here, $a_j(t)$ represents the temporal variation of the jth mode, and $E(\cdot)$ and $\|\cdot\|$ denote the time average and norm in the L^2 space, respectively. The mode shapes, φ_j, are ordered in such a way that the lowest modes have the highest energy as defined by the inner product on f. Due to the nature of FTF as a relationship between variables with different scales and units, a normalization procedure is necessary in this data analysis step. A slight variation of the method of snapshots [158] is implemented on the database described earlier. From a data processing point of view, different dimensions of the unsteady heat release, velocity, and pressure data are heterogeneous with respect to their variance. Thus, the data is normalized by subtracting the mean and then dividing by the square root of the variance at each point, so that each point is now standardized with zero mean and unit variance. This normalized data is then used as the input to the traditional method of snapshots.

4.3.2 Autoregressive Moving Average

From a statistical modeling standpoint, the objective of a data-driven relationship between unsteady release and flowfield variables relies on correlation data analysis. As previously mentioned, a typical approach is to use the cross-correlation and autocorrelation information to obtain the relationship, which can be incorporated into the classical $n-\tau$ model for a single time lag. This can be interpreted physically as representation of a single dominant physical process that governs the gain of unsteady of heat release. In order to generalize this relationship for multiple time lags, as it is evident that the combustion process has a range of relevant time scales, the following statistical transfer function model can be considered for quantifying the effect of velocity on unsteady heat release:

$$\dot{Q}_j'(t) = \sum_{k=1}^{K_u} \sum_{\tau=0}^{L} \beta_{k\to j}(\tau)\, u_k'(t-\tau) + \epsilon_j(t), \qquad j = 1, \cdots, K_{\dot{Q}}, \tag{4.11}$$

where $\dot{Q}_j'(t)$ and $u_j'(t)$ are the time-varying coefficients of the j-th mode of $\dot{Q}$ and u, up to a maximum of $K_{\dot{Q}}$ and K_u modes, respectively, $\beta_{k\to j}(\tau)$ is the transfer weight from the k-th mode of u to the j-th mode of $\dot{Q}$, at a time lag of τ up to a maximum of L time lags , and $\epsilon_j(t)$ are zero-mean noise processes. The SISO transfer function, also known as the classical $n-\tau$ model, can be recovered as an instance of the framework in Eq. (4.11), for the modeling of a single time lag, τ, or frequency. For this fixed lag, set the cross-mode weights $\beta_{k\to j}(\tau)$ as 0, and assume that the same-mode transfer weights $\beta_{k\to j}(\tau)$ equals some constant $\beta(\tau)$. The model then becomes

$$\dot{Q}_j'(t) = \beta(\tau) u_j'(t-\tau) \tag{4.12}$$

Further assuming that the spatial modes for $\dot{Q}'$, u' and ρ' are equal, we get

$$\sum_{j=1}^{\infty} \dot{Q}_j'(t)\phi_j(x) = \sum_{j=1}^{\infty} \beta(\tau) u_k'(t-\tau)\phi_j(x) \quad \Rightarrow \quad \dot{Q}'(t) = \beta(\tau) u'(t), \tag{4.13}$$

which is precisely the $n-\tau$ model.

In this sense, the training of the proposed model can be seen as a data-driven method for learning the multiple feedback patterns of the flow oscillations extracted from POD. This procedure involves using the cross-correlation function and various autocorrelation functions based on the specified number of discrete time lags to obtain the transfer weights.

From the above derivation, this provides three advantages over the $n-\tau$ model: 1) it provides the framework for incorporating multiple feedback time lags, 2) it allows for the selection of significant cross-mode transfer weights, 3) it enables the estimation of transfer weights using simulation data. The estimation of the zero-mean noise process $\epsilon_j(t)$ can also provide valuable insights on the adequacy of the fitted function and flow variable selection, as identification of dominant frequencies in the noise process $\epsilon_j(t)$ suggests that there are influential flow variables which are unaccounted for in the transfer function. Conversely, if $\epsilon_j(t)$ has little auto-correlation (that is, it is almost white noise), it is possible that the fitted transfer function adequately captures feedback behavior. Furthermore, the non-stationarity of $\epsilon_j(t)$ suggests that the noise process may have increasing variation over simulation time. From a design perspective, this non-stationarity calls for additional investigation, since it suggests that the combustion process becomes increasingly unstable over time.

The framework can be constructed such that Eq. (4.11) and the reconstruction formula for POD are combined:

$$\dot{Q}(x,t) = \sum_{j=1}^{K_{\dot{Q}}} \left\{ \sum_{k=1}^{K_u} \sum_{\tau=0}^{L} \beta_{k\to j}(\tau) \int u'(x',t-\tau)\psi_k(x')\,dx' \right\} \phi_j(x), \tag{4.14}$$

where $\phi_j(x)$ and $\psi_j(x)$ are the j-th spatial mode for $\dot{Q}$ and u, respectively. In the frequency domain, this becomes:

$$
\begin{aligned}
\hat{\dot{Q}}(x,\omega) &= \mathcal{F}\{\dot{Q}(x,t)\} \\
&= \mathcal{F}\left\{\sum_{j=1}^{K_{\dot{Q}}}\left\{\sum_{k=1}^{K_u}\sum_{\tau=0}^{L}\beta_{k\to j}(\tau)\int u'(\tilde{x},t-\tau)\psi_k(\tilde{x})\,d\tilde{x}\right\}\phi_j(x)\right\} \\
&= \sum_{j=1}^{K_{\dot{Q}}}\left\{\sum_{k=1}^{K_u}\sum_{\tau=0}^{L}\beta_{k\to j}(\tau)\int \mathcal{F}\{u'(\tilde{x},t-\tau)\}\psi_k(\tilde{x})\,d\tilde{x}\right\}\phi_j(x) \\
&= \sum_{j=1}^{K_{\dot{Q}}}\left\{\sum_{k=1}^{K_u}\sum_{\tau=0}^{L}\beta_{k\to j}(\tau)e^{-i\omega\tau}\int \hat{u}(\tilde{x},\omega)\psi_k(\tilde{x})\,d\tilde{x}\right\}\phi_j(x).
\end{aligned}
\tag{4.15}
$$

As a statistical model, the formulation in Eq. (4.11) can be viewed as a large-scale, coupled system of sparse Box-Jenkins transfer models [159] with multiple inputs. One approach for estimating parameters in such a model is to recast the model as the following regression problem (for simplicity, we only consider u as input below):

$$
\begin{bmatrix} \dot{Q}_j'(T) \\ \dot{Q}_j'(T-1) \\ \vdots \\ \dot{Q}_j'(L) \end{bmatrix} = \sum_{k=1}^{K_u} \begin{pmatrix} u_k'(T) & u_k'(T-1) & \cdots & u_k'(T-L) \\ u_k'(T-1) & u_k'(T-2) & \cdots & u_k'(T-L-1) \\ \vdots & \vdots & \ddots & \vdots \\ u_k'(L) & u_k'(L-1) & \cdots & u_k'(1) \end{pmatrix} \begin{bmatrix} \beta_{k\to j}(0) \\ \beta_{k\to j}(1) \\ \vdots \\ \beta_{k\to j}(L) \end{bmatrix} + \begin{bmatrix} \epsilon_j(T) \\ \epsilon_j(T-1) \\ \vdots \\ \epsilon_j(L) \end{bmatrix}, \tag{4.16}
$$

where T is the total number of time-steps simulated. This can be expressed in the more compact matrix notation:

$$
\dot{\boldsymbol{q}} = \sum_{k=1}^{K_u} \boldsymbol{U}_k \boldsymbol{\beta}_k + \boldsymbol{\epsilon} \tag{4.17}
$$

A naïve way to estimate the transfer weights is to use standard regression techniques (which involve solving a very large linear system), but this is inappropriate for two reasons: multicollinearity and sparsity. Multicollinearity here refers to a common

problem in regression where the regression covariates in $\boldsymbol{U}_k$ are highly correlated with one other. This is certainly true for the time-series data here, since the columns of $\boldsymbol{U}_k$ are constructed from snapshots of the same dynamic system $u_k'(t)$, and are therefore highly correlated as a result. The presence of multicollinearity can present challenges in the estimation of regression coefficients, since it is difficult to quantify the effect of a covariate when it is highly correlated with other covariates [160]. Moreover, there is sparsity in the selection of significant transfer weights in Eq. (4.18). From a flow physics perspective, several key feedback mechanisms are present in the system. In terms of the proposed model, this means that only the transfer weights corresponding to important feedback mechanisms are non-zero, and the remaining weights are equal to zero. The selection of these non-zero transfer weights using simulation data thereby allows for the identification of important flow physics and mechanisms in the system, which can be further investigated with respect to combustion instability. It is worth noting that selection cannot be performed simply by taking the largest estimated coefficients from regression, since the signals for active and inert covariates can be rendered quite similar through multicollinearity [161].

In light of these challenges, state-of-the-art variable selection techniques in machine learning should be incorporated. The following optimization formulation is proposed for selecting and estimating the transfer weight parameters:

$$\min_{\boldsymbol{\beta}} \frac{1}{2}\left\|\dot{\boldsymbol{q}} - \left(\sum_{k=1}^{K_u} \boldsymbol{U}_k \boldsymbol{\beta}_k\right)\right\|_{\mathbf{2}}^{\mathbf{2}} + \lambda \sum_{k=1}^{K_u}\sum_{\tau=1}^{P} P(\beta_{k\to j}(\tau); \lambda, \gamma), \tag{4.18}$$

where $\boldsymbol{\beta} = \left[\boldsymbol{\beta_1}, \cdots, \boldsymbol{\beta_{K_u}}\right]^{\boldsymbol{T}}$. Here,

$$P(\beta;\lambda,\gamma) = \lambda \int_0^{|\beta|} \max\left(1 - \frac{x}{\gamma\lambda}, 0\right) dx \tag{4.19}$$

is the minimax concave penalty function [162]. This particular choice of non-convex penalty is appealing because the tuning parameters λ and γ address both the need for reliable parameter estimation under sparsity and the multicollinearity outlined earlier. Specifically, a larger choice of $\lambda > 0$ provides a sparser selection of weights, meaning that fewer feedback mechanisms are chosen to be significant. Likewise, a smaller choice of $\gamma > 1$ allows the selection criterion in Eq. (4.18) to handle data with higher multicollinearity. For fixed λ and γ, the optimization in Eq. (4.18) can be solved using the algorithm in Mazumder et al. [163], which is available in the R package SparseNet. As is typical in statistical learning algorithms, the parameters λ and γ are tuned using cross-validation techniques [161].

4.4 Results and Discussion

4.4.1 POD Analysis

As previously mentioned, the data is first normalized and the method of snapshots is implemented to compute the POD modes. The database contains 300 snapshots of the flowfield. The time interval between snapshots is 10 μs. The data available yield a Nyquist frequency of 50 kHz and a frequency resolution of $\Delta f = 333$ Hz. This level of resolution is considered sufficient for a demonstration of the methodology, as most chamber mode frequencies of interest lie between 1.6 kHz and 3.5 kHz [15]. Figure 38 presents the energy distribution of the POD modes for the unsteady heat release and pressure oscillations. This

illustrates just how dynamic the combustion process is, with unsteady heat release requiring nearly 150 modes to capture more than 80% of the total energy in the oscillatory flowfield. The pressure modes are able to achieve 80% of the energy with around 50 POD modes. Figure 39 compares the first four POD coefficients, a_j, for unsteady heat release and pressure. These time varying coefficients serve as the time series for correlation analysis. As previously mentioned, the combustion process is treated as an autoregressive process. The time varying output of the system is dependent upon internal feedback mechanisms present in the system, characterized through time-delay embedded methods [150]. With an appropriate number of time delays corresponding to a specified frequency resolution, the proposed methodology models the mechanisms and "transfer weights" between the POD modes of unsteady heat release and pressure.

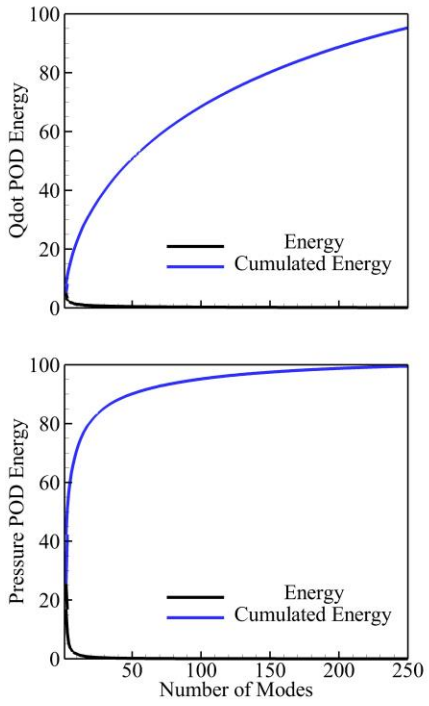

Figure 38. Energy distribution of POD modes for unsteady heat release and pressure oscillations

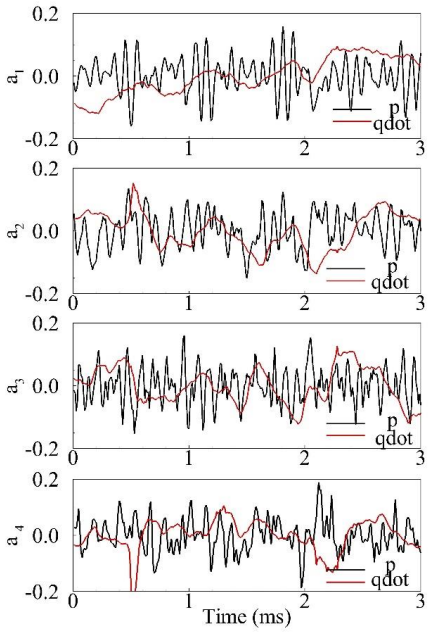

Figure 39. First four POD coefficients, a_j, for unsteady heat release and pressure.

The transfer weights quantify the effects that each of the POD modes has upon the unsteady heat release POD modes. Figure 40 shows the first POD mode of unsteady heat release and the first four POD modes of pressure. The POD mode of unsteady heat release is difficult to interpret from a physical point of view and its functionality lies in providing a spatial distribution for the data analysis. The first four pressure POD modes are provided as a demonstration of how this methodology is physics-based. All four modes demonstrate an acoustic standing mode within the GOX post. Considering only the GOX post region, the first three modes resemble each other and show the existence of a 3/2-wave mode, with the full acoustic wavelength occupying the GOX post. This resembles the results obtained from the 1T triggering studies conducted by Urbano et al [164]. The fourth mode shows a similar effect, but the amplitude of the standing wave is mitigated. Looking past the post tip, the pressure fluctuation provides downstream shear flow information. The coherent

structures extracted by the POD represent the hydrodynamic effects of the mixing layer generated from the gas-liquid mixing. The positive regions indicate the presence of convecting vortical structures and Kelvin-Helmholtz shear layer instability. These structures then develop into a recirculation zone, as the taper region induces an expansion, which causes the flow to diverge. The recirculation zone in the taper region provides a heat pool to preheat propellant and acts as a secondary flame stabilization mechanism [122].

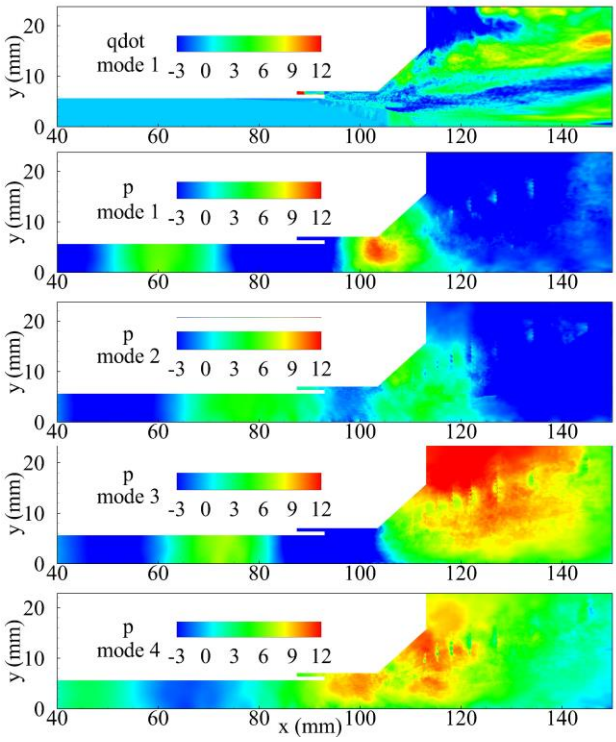

Figure 40. POD modes: first mode of unsteady heat release and first three modes of pressure

A key obstacle is the quality of the signals, which affects the confidence in the establishing correlation between signals, i.e. coherence. For a system having multiple inputs and outputs, the partial coherence is the coherence computed between any individual input and the output when the effect of all other inputs is removed from the output by a

linear least squares prediction. This coherence obeys the usual inequality, and will reveal the existence of a linear relationship between a particular residual input (forcing modes) and the output (heat release modes) even when the relationship is not apparent from the ordinary coherence function. Figure 41 shows the partial coherence for the unsteady release modes with respect to the pressure POD modes. The partial coherence remains above a minimum of 0.85 for the unsteady heat release information, implying good correlations can be established. The noise model accounts for around 0.10 of the time series signal. There are a frequencies where the coherence is lower than the average, and this can be improved by gather better data that has a forcing signal.

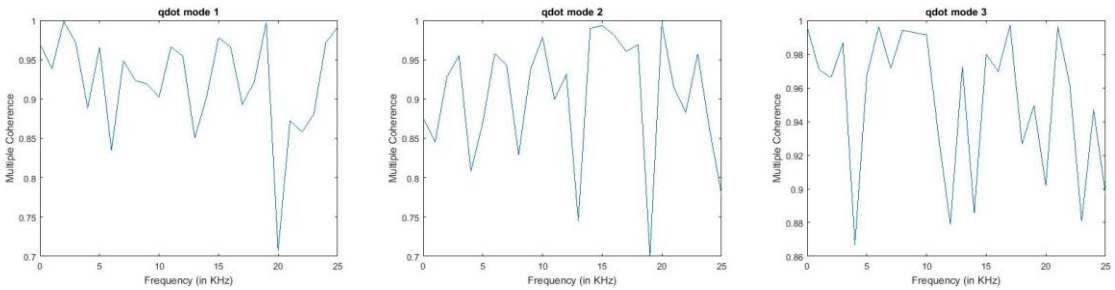

Figure 41. Partial coherence of unsteady heat release modes.

4.4.2 ARMA System Identification and Selection

It is should be noted that this analysis shows oscillations composed of both hydrodynamic and acoustic components. The associated time lags for these two phenomena are not the same, or even of the same scale, so it is necessary to differentiate the acoustic from the hydrodynamic fluctuations of pressure and velocity. Under the assumption that the turbulent noise is taken into account by the noise model, and hydrodynamic effects induce acoustic responses that are proportional to the unsteady heat

release, system identification yields a dynamic flame response model that takes into account the time lags associated with the pressure oscillations.

Figure 42 shows the transfer weights for the POD modes shown in Fig. 40. This plot shows the contributions to the transfer between each of the first four pressure POD modes and the first mode of the unsteady heat release. The key mechanisms have been identified as primarily hydrodynamic, as the standing wave within the GOx post does not directly affect the heat release downstream. With 250 time lags, a time lag being the 10 μs time interval between snapshots, the results can be interpreted in the frequency domain by treating the modeled transfers as oscillatory processes with a specific frequency. The corresponding frequency resolution is 400 Hz, as that is the maximum time period involved in the correlation analysis. For the first pressure mode, there exists a periodic mechanism with its first harmonic being around 520 Hz. The amplitude increases for its 3/2 harmonic, which has a frequency of 780 Hz. This low-frequency feedback mechanism should be attributed to a phenomenon with a time scale around 1.9 ms, as illustrated by the transfer weight analysis. This mechanism is the 3/2 wave structure extracted from the POD previously mentioned. It should be noted these frequency values are not fully integer harmonics, possibly caused by the nonlinear nature of the combustion flowfield.

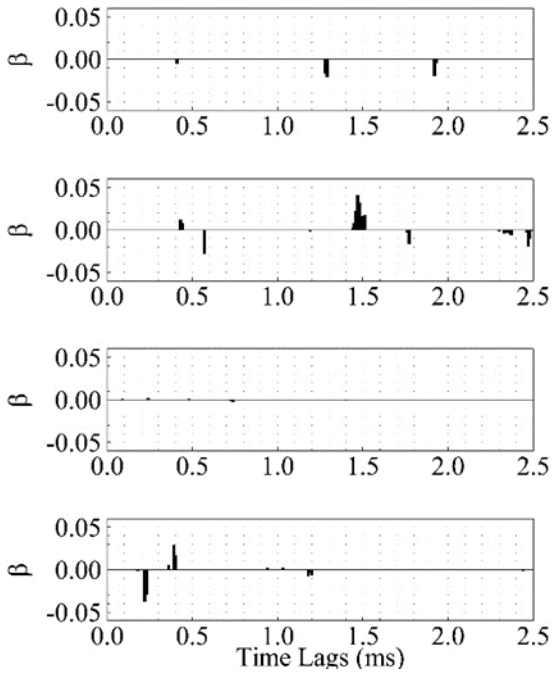

Figure 42. Transfer weights for first mode of unsteady heat release

The periodicity observed in these results is similar to oscillations in circulation in a premixed swirling flame [165]. Komarek and Polifke used a model to explain the physics of how a disturbance modulates the heat release as it is transported through the flame, providing additional mixture to be burnt. Their model also described how the fluctuation of circulation causes both radial and axial velocity fluctuation downstream of the flame, broadening the flame surface area. This increase in heat release is followed by a decrease due to more rapid combustion of the mixture. The key time scales their model accounts for are those of acoustic waves and fluctuations in circulation. A similar process is at play in the present study, as the recirculation in the taper region acts as a secondary stabilization mechanism [122]. This stabilization mechanism was also reported in the findings of experimental studies on nonlinear flame transfer function characteristics in a swirl-

stabilized combustor [166]. The driving frequency for where the flame response saturates has a similar frequency to the oscillatory process identified here.

POD not only serves as a filter to extract physical features from the original signal, but is also used here in order to incorporate the spatial distribution of flowfield variables into the FTF. Kim et al. [167] concluded that when the flame is not acoustically compact, the local flame transfer function, which included spatially resolved measurements, yielded more accurate predictions. Using Eq.(4.15), a local FTF can be deduced using a probe at a particular point. Traditional FTF's have used mechanisms such as inlet forcing to represent the input for the combustion response, but this approach leads to an ill-defined problem when the reference point is not close enough to the chamber [168]. This "compactness" limit is quantified here in terms of distance between the reference point, the inlet forcing, and the combustion chamber. One solution is to incorporate local unsteady pressure in addition to the velocity upstream of the flame to predict the heat release oscillations. For high-frequency oscillations of interest, such as the tangential modes of typical rocket combustors, the "compactness" assumption fails, as disturbances are on the same scale as the geometry. Thus, a local FTF is developed based on a single probe, quantifying intrinsic processes through autoregressive correlation analysis on that particular point. An example probe is shown in Fig. 43, relative to the axial velocity field, as this is indicative of the shear flow and recirculation region that splits the flow.

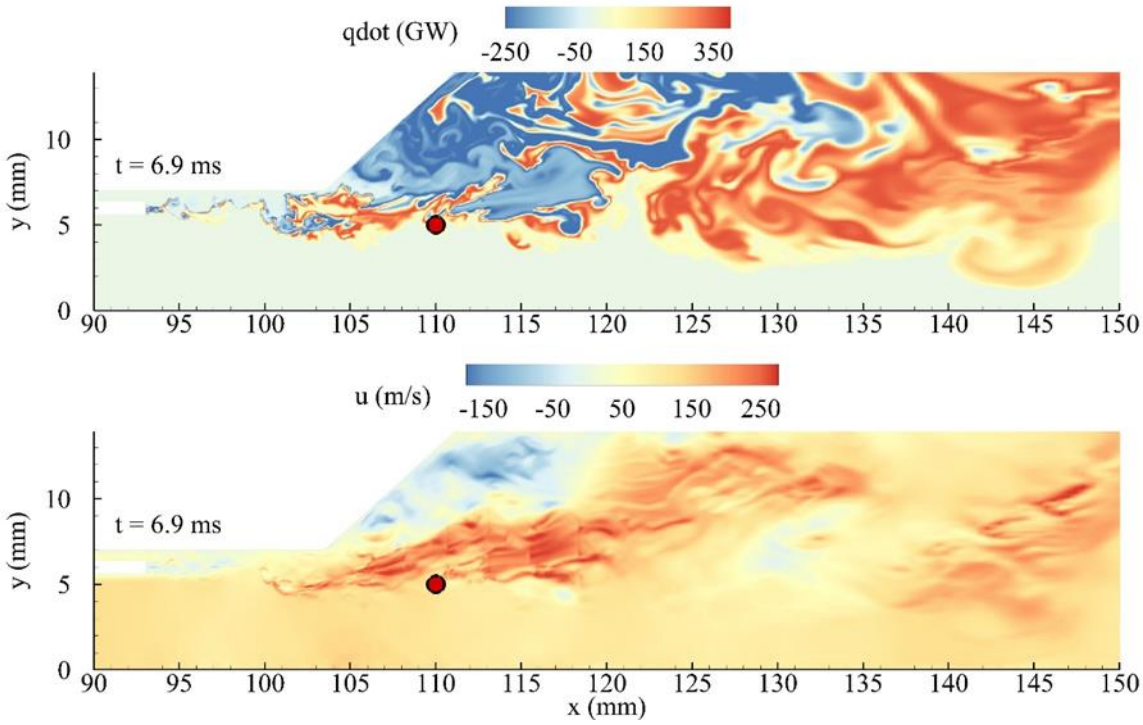

Figure 43. Example probe location at x=110 mm and y=5 mm

With the example point, Eq. (4.15) can be used to calculate the FTF, in terms of gain and phase information. Figure 44 shows the FTF results following the 4-mode analysis. The gain increases to a maximum near 3.3 kHz. It increases again after an inflection point around 6.2 kHz. For lower frequencies, the pressure leads the combustion response, as illustrated by the negative phase. It is known that high frequencies attenuate and absorb sound better than low frequencies, through thermal and viscous absorption. Interestingly, this is not the case here, as the gain actually increases in the higher frequency region, implying the presence of a dominant mechanism that instigates a combustion response. It should be noted that 4 POD modes captures only about 10% of the unsteady heat release flowfield energy and the higher frequency results require more modes for interpretation.

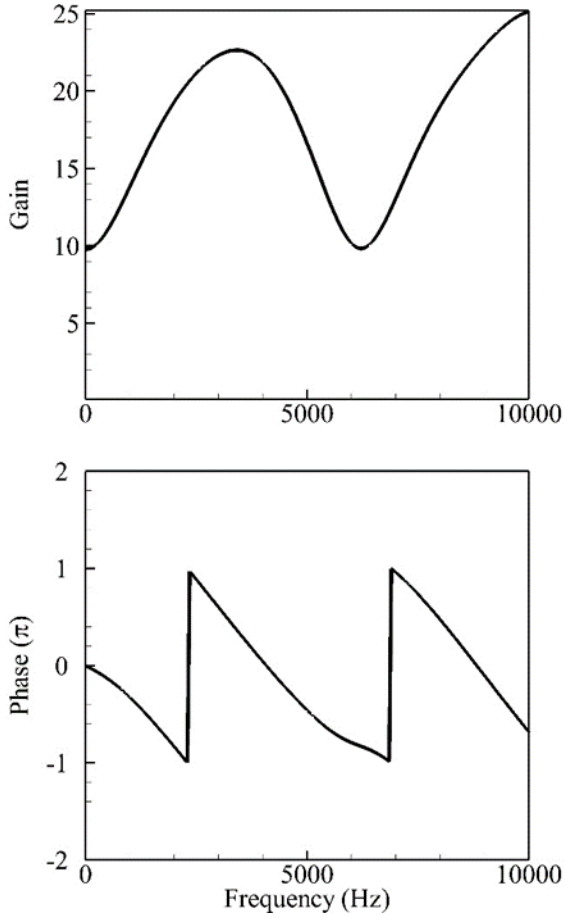

Figure 44. FTF gain and phase information for 4-mode analysis.

In order to better capture the information from the original flowfield, more modes should be incorporated into the analysis. Intuition suggests that the reconstruction should yield a better combustion response with the fully reconstructed flowfield. With 150 POD modes, 95% of the energy within the unsteady heat release flowfield is captured. 150 was therefore chosen as the proper mode number for the remaining data analysis. Figure 45 shows the FTF extracted at the same point as before. The spectrum has shifted to the left, with the maxima appearing at lower frequencies than the 4-mode analysis shown in Fig. 44. In addition, two peaks appear at 0 kHz and 3.6 kHz. The maximum gain also increases

to 12 for 6.8 kHz. Further analysis and possible experimental efforts are required to validate these values. For now, these will be interpreted as physical mechanisms having an impact on the combustion response.

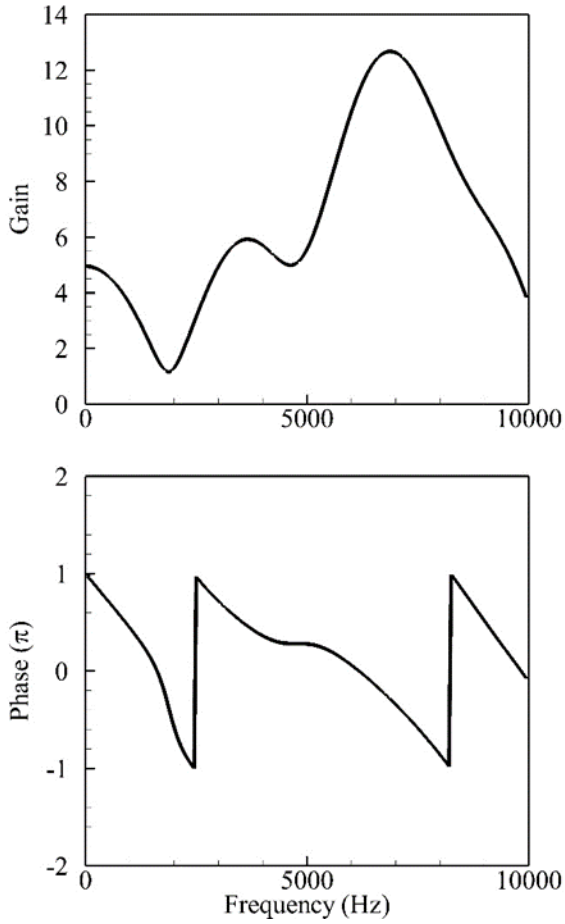

Figure 45. FTF gain and phase information for 150-mode analysis.

It should be noted that this analysis yields different results for traditional premixed flame analysis. For flames perturbed by acoustic and vortical disturbances [169], the key physical process is the distortion of the flame surface by perturbations, leading to fluctuations in burning area. At low frequencies, the flame speed remains essentially constant, rendering the heat release oscillations directly proportional to the oscillating

flame area. As hydrodynamic straining and stretching grow in importance with frequency, fluctuations in flame speed change the combustion response [170]. The diffusion flame in the present study depends on the mixing process, which is directly affected by the convecting vortices that are formed after the GOX post. The zero frequency gain can be interpreted as steady state combustion, implying the existence of intrinsic combustion response. The source of this mechanism may be better identified with spatial distribution of the gain, as discussed later.

With the present methodology, frequency spectrum information can also be plotted spatially for a given frequency. The dominant mechanisms of the system have been identified as acoustic standing waves within the GOx post, vortex shedding after the post tip [120, 121], and recirculation in the taper region [122]. The effect these mechanisms have upon unsteady heat release can then be quantified.

As current injectors are designed to damp combustion chamber oscillations and mitigate combustion instability, the frequencies of interest can be estimated for cylindrical chambers based on Bessel functions [41] or by conducting an eigenmode analysis [18, 116]. Using Bessel functions to yield a first cut approximation of frequencies:

$$f_c = \alpha_{nm} \frac{c}{2\pi R} \tag{4.20}$$

For a typical ORSC chamber radius, $R = 0.19$ m, the first and second tangential modes (α_{11} =1.841 and α_{12} =3.054) of interest are about 1.9 kHz and 3.1 kHz respectively. A typical approach is to treat the injector as an acoustic resonator and tune its length based on the frequency, f_c, to be damped [15]. As discussed in previous studies

[120-122], vortex shedding and recirculation play a pivotal role in the system combustion dynamics, as large-scale wrinkling is associated with the shear layer mixing and vortex rollup. These motions lead to significant combustion response because the flame is stabilized in these regions, where it is dominated by shear layer and vortex dynamics. This convectively unstable shear layer has responded to acoustic forcing in a transversely excited swirl flow configuration [171]. The combustion response is a result of the motion in the shear layer and can be estimated using vortex shedding theory to explain the coupling between vortical and acoustic motions [121, 172]. For the configuration under consideration here, these calculated frequencies can be used to identify the combustion response spatially. For the 1T mode, 1.9 kHz, the gain and phase information of the obtained FTF is shown in Fig. 46.

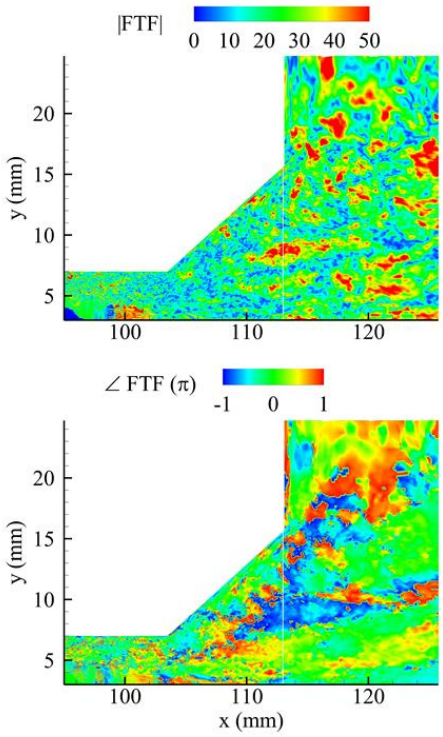

Figure 46. Gain and phase for 1.9 kHz.

There are regions in the recess area that are numeric artifacts from the interpolation process needed for visualization. Figure 47 shows the gain and phase information for 3.1 kHz, which is the approximated 2T mode. As in the previous figure, there appears to be a high gain region after the taper recirculation region. It should be noted most of the high gain region is in phase with the pressure oscillations, invoking the classical theory that high combustion response is achieved when signals are in phase [110]. The shear layer region separates the flow into two branches of high response, reciprocating the phenomenon in Fig. 46. The high response region in the taper region is of great interest, as this reflects the secondary stabilization mechanism and the direct effect of the 2T mode.

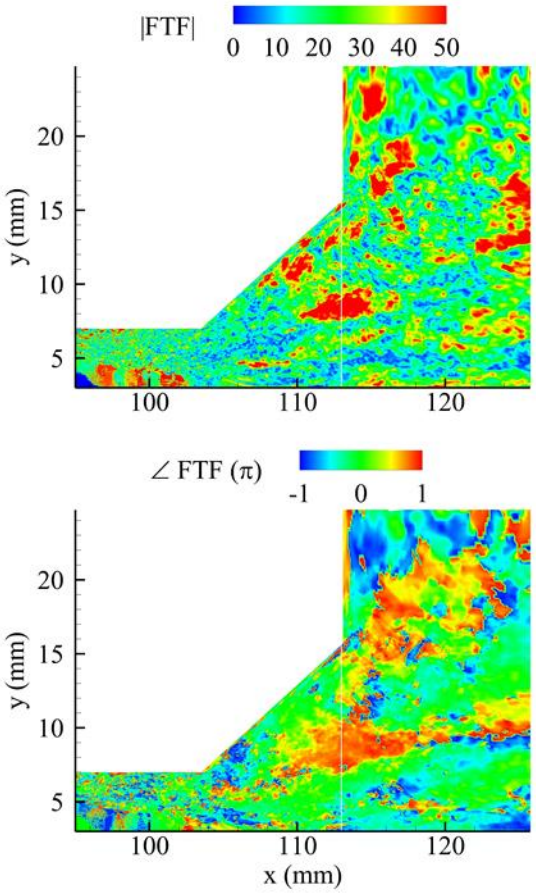

Figure 47. Gain and phase for 3.1 kHz.

If the GOx post is treated as a half-wave resonator, the resonance frequency is estimated to be 2.3 kHz [120, 121]. This harmonic oscillation interacts with hydrodynamics and combustion process downstream. As previously mentioned, a key process controlling the mixing and combustion is the vortex shedding phenomenon. The combustion response for this frequency is plotted in Fig. 48.

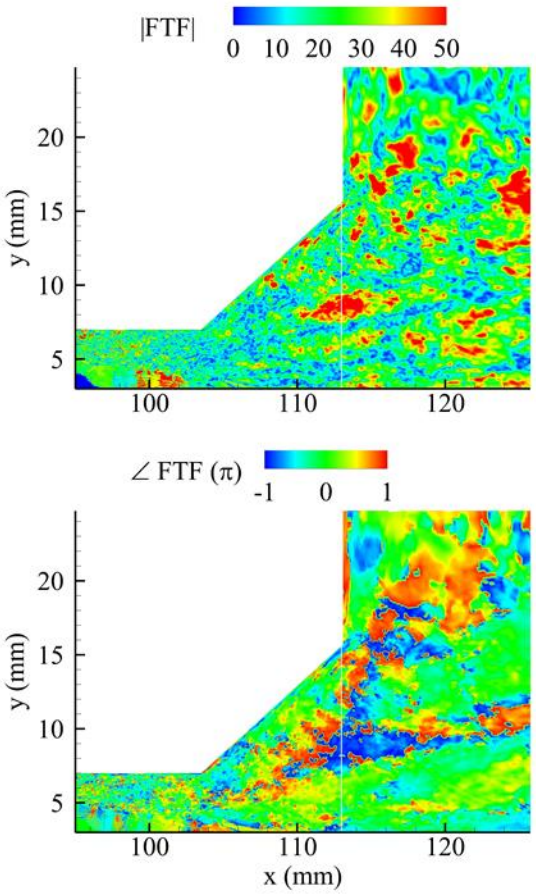

Figure 48. Gain and phase for 2.3 kHz.

Figure 49 compares the response for the extreme cases. The plots show that the spatial combustion response for this frequency range is similar, implying that a dominant mechanism controls this process. The time scale ranges from 0.3 – 0.5 ms and the spatial

distribution of the response is concentrated in the region where convecting vortices appear. To compare how the recess length affects this distribution, the same figure is reproduced for the two extreme cases, no recess and full recess. The top figure shows the response for the no-recess configuration. The extended mixing time reduces the tangential momentum, which in turn reduces the strength of the recirculation zone that acts as a secondary stabilization mechanism. The combustion process instead relies on the backward step after the taper region, and this is the region of high response. For the opposite reason, a similar situation arises the fully recessed configuration. As there is minimal mixing between the propellants, the swirling fuel is able to radially and tangentially project itself after the taper region. The backward step acts as the secondary mechanism and shows a high response for the entire region. In addition, the taper itself is strongly affected by the combustion process, because the flame is anchored near the taper region, where there is a recirculation zone, rather than in the recess region.

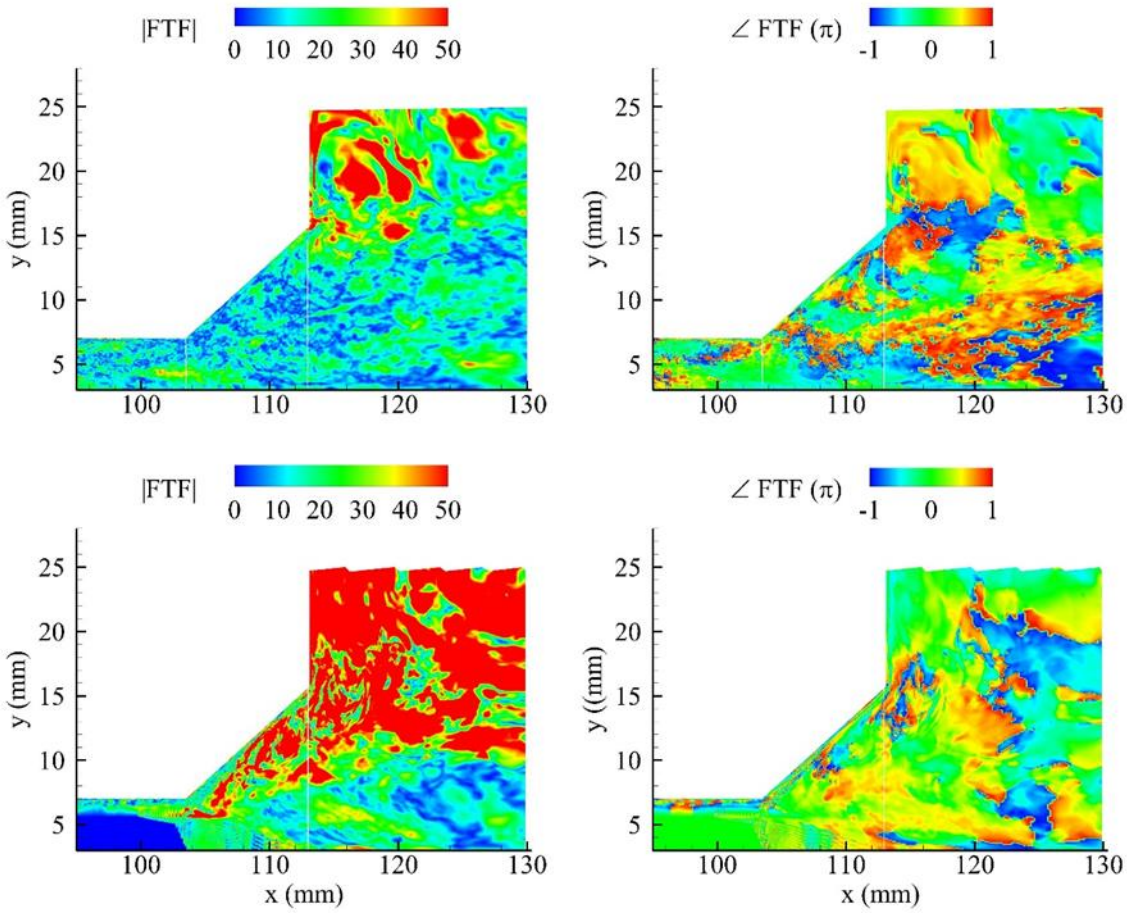

Figure 49. Comparison of 2.3 kHz response for extreme cases: (top) no recess (bottom) fully recessed

The combustion responses for these configurations show that the baseline case has a favorable response compared to the two extreme configurations. With the appropriate recess length, the combustion process has enough time to commence, anchor, and develop, before reaching the recirculation zone, where convecting vortices are dominant.

4.5 Conclusion

Combustion stability is of utmost importance in all combustion devices, and especially in rocket engines, because of their high chamber pressures and resultant destructive potential. This study proposes a data analytic methodology to characterize the highly complex and nonlinear nature of combustion dynamics. A key component of comprehensive combustion stability analysis will be the quantification of the combustion response and its incorporation into thermoacoustic stability analysis. As high fidelity simulations are necessary to characterize the supercritical flowfield and capture the combustion dynamics, the methodology leverages LES in combination with machine-learning data analysis techniques to quantify the distributed combustion response.

The acoustic stability analysis framework based on the generalized wave equation has long been established, but proper presentation of the combustion response is the main contribution of this study. Treating the extracted coherent structures as time series signals, the combustion response can be deduced through autoregressive model selection, accounting for data sparsity, multicollinearity, and noise. The results show that acoustic-vortical dynamics is the dominant mechanism, as it directly affects the flame stabilization. This data-driven methodology is able to quantify the gain and phase relationship between flowfield variables and unsteady heat release.

Further investigation into the model selection process is still needed to validate the results, as past studies have primarily focused on the Rayleigh index, a correlation parameter on a single time scale. The proposed methodology not only accounts for the distributed combustion response through the incorporation of POD analysis, but also uses

the data to identify relevant time scales, replacing the need for forcing and focusing on intrinsic dynamics. Another interesting direction is the reduced-order modeling of the proposed flame transfer function over a design space of interest. Such a task may require a combination of state-of-the-art statistical methods for emulation and correlation extraction as well as sophisticated signal processing algorithms.

CHAPTER 5. SYSTEM-LEVEL MODEL

Combustion dynamics involves large-amplitude self-excited oscillations that have negative effects on engine performance and life. Combustion instabilities hinder engine development, and in extreme cases cause catastrophic failure. The phenomenon results from a resonant coupling between a heat release and flow motions within a chamber. Once the instability is established, an energy feedback loop between the oscillations and the combustion response can result in a limit cycle behavior. A critical issue affecting liquid rocket engines is the occurrence of high-frequency instabilities, while low-frequency oscillations can result in longitudinal structural oscillations of the rocket. Mitigation strategies historically involve performing testing at various (i.e., component, subsystem, and system) scales and making ad-hoc adjustments to the engine design, such as adding acoustic dampers and redesigning injectors. Prior attempts at model combustion stability behaviors typically employ a wave equation governing unsteady motions in a chamber [136], with all gas-dynamic and combustion effects treated either rudimentarily or empirically.

Methodologies for analyzing and predicting system stability varies on a spectrum from purely analytical to numerical approaches. Several linear stability analyses have been developed and will be the focus of this work. In this framework, the unsteady pressure and velocity fields are approximated as a Fourier synthesis of the chamber normal modes, weighted with time-varying coefficients [136, 173]. A spatial averaging procedure is applied to extract a set of coupled ordinary differential equations governing the time evolution of the modal amplitudes. The analysis yields a complex growth constant

associated with various physical processes, in the form of surface or volume integrals of the unperturbed chamber modes, typically for simple geometries and flowfields. The governing equations can be numerically solved over the domain as well, requiring significant computational resources. A more practical approach is to compute the acoustic field within a chamber by solving linearized perturbation equations in the form of Helmholtz equation [174]. The eigenmode analysis can be conducted on the general acoustic wave equation, accounting for geometric details and incorporating volumetric and boundary effects through source terms.

The present work will use the RD-170 engine as a demonstrative example. Figure 50 shows the internal components of the RD-170 main injector. There are a total of 331 gas-centered liquid-swirl coaxial injectors: 271 main injectors that are recessed into the injector face, and 60 baffle injectors. The oxidizing gas in the manifold entered axially through the inlet orifices, and the fuel flows into the injector through the tangential inlets. At the entrance to the oxidizing gas manifold is a distributor plate perforated with flow orifices, which acts as an acoustic liner that damps acoustic waves. The mechanism of sound absorption revolves around vortex shedding [175], as acoustic waves incident on an orifice cause periodic shedding from the orifice rim. Some portion of the energy is reflected, some transmitted, and the rest is converted to kinetic energy of the vortices. If the orifices are spaced apart that their shear layers do not interact, then the liner can be treated as a homogeneous compliant surface whose impedance can be built up from the each individual orifice. The injectors can provide acoustic damping a variety of mechanisms: vortex shedding, viscous dissipation, and wave cancellation due to coupling of acoustic modes between the injector and the combustor.

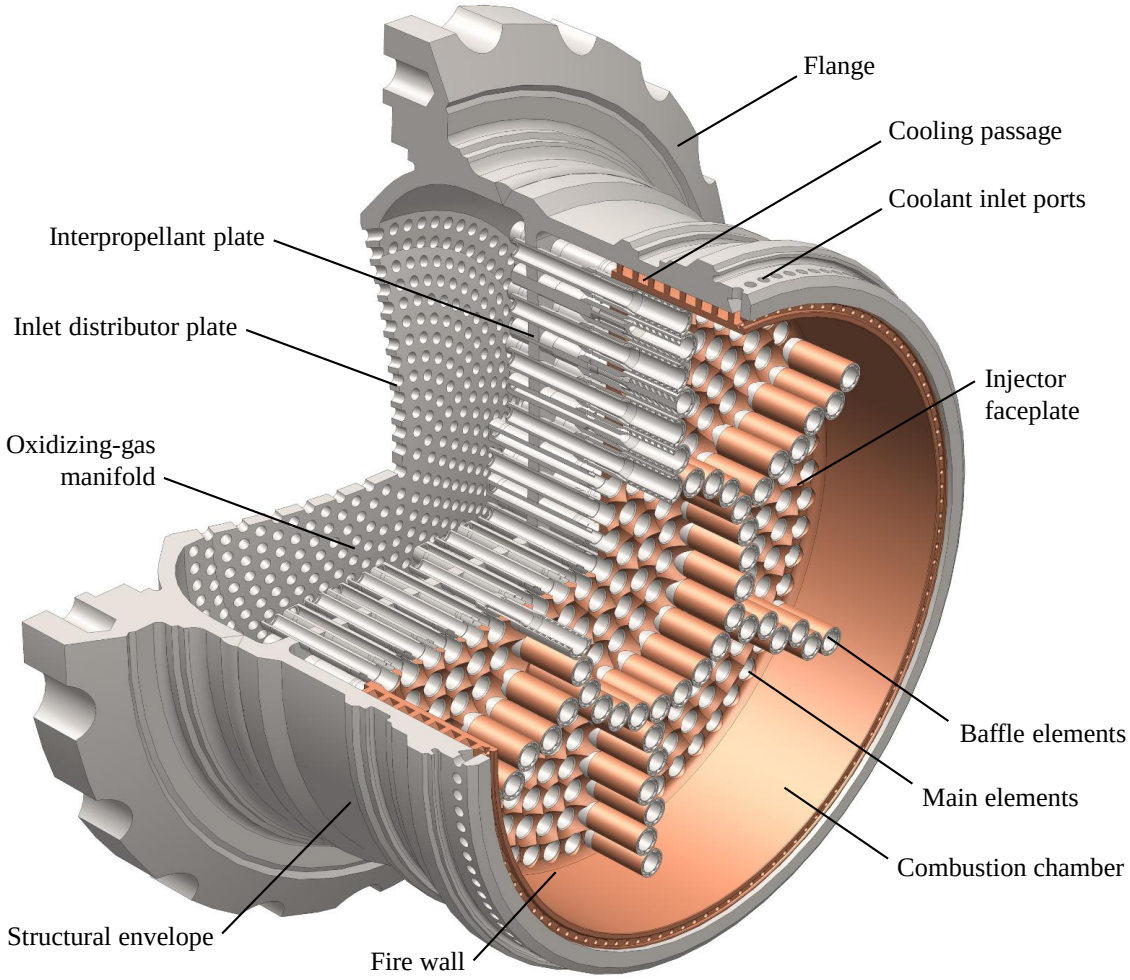

Figure 50. Overview of RD-170 main injector head.

5.1 System-level Thermoacoustic Stability

This is last component of the MBSE study, which involves the linear stability analysis for the full combustor and incorporating the source terms extracted from component-level flowfields. The wave equation in its most general form is given below, where $\mathcal{M}$ contains the monopole source terms such as mean flow effects and $\mathcal{D}$ the dipole source terms such as vortical effects. The unsteady heat release source term (boxed red) is contained within the monopole sources.

$$\frac{1}{\bar{\rho}\bar{a}^2}\frac{\partial^2 p'}{\partial t^2} - \frac{1}{\bar{\rho}}\nabla^2 p' = \mathcal{M} - \frac{1}{\bar{\rho}}\nabla\cdot\mathcal{D}$$

$$\mathcal{M} = \frac{1}{\bar{\rho}\bar{a}^2}\left(\bar{u}\cdot\nabla\frac{\partial p'}{\partial t} + \frac{\partial}{\partial t}(u'\cdot\nabla p') + \bar{\gamma}\frac{\partial p'}{\partial t}\nabla\cdot\bar{u} + \bar{\gamma}\frac{\partial}{\partial t}(p'\nabla\cdot u') - \frac{\partial \mathcal{P}'}{\partial t}\right) \qquad (5.1)$$

$$\mathcal{P} = \frac{\bar{R}}{\bar{C}_v}[\dot{Q} + \delta Q + \delta u_\ell \cdot F_\ell + (e_{\ell 0} - e_0)w_\ell + u\cdot\sigma - \bar{C}_v\nabla\cdot(\rho_\ell \delta u_\ell)]$$

The governing equations, subject to appropriate boundary conditions, will be solved by a finite-element code (e.g., COMSOL, ANSYS, etc.) for assessing system-level stability behaviors in terms of oscillation frequency and growth constant. The effect of each of the known processes, including boundary and distributed source terms, on the stability characteristics will be quantitatively assessed, either individually or collectively. The finite-element based acoustic solver allows for swift treatment of complex geometry, a feature that conventional stability analysis codes fail to possess. The source terms in the wave equation, especially the combustion response, will be acquired from the high-fidelity model and data analytics. It is key to note that the source terms have been computed from component-level domains simulated/predicted by the LES or surrogate model. The protocol for how these source terms populate the entire combustor computation domain allows for specifying how the injectors are distributed within the system.

The combustor is treated as a gas volume. The manifold and injectors contain only oxidizer, while the combustion chamber is assumed to have equilibrium products. Dodecane is used as a surrogate fuel for kerosene [176]. Impedance conditions are applied close the formulation. The converging nozzle is treated as an acoustically rigid boundary.

As mentioned previously, the flow distributor impedance is obtained by assuming the GOx flow is relatively uniform, and each orifice is separated by enough distance to avoid interaction. An equivalent impedance derived for the injector faceplate by taking into account of viscous dissipation and vortex shedding. In addition, the effects of mean flow can be incorporated as a monopole source term.

With the gas properties and impedance conditions applied, a finite-element acoustic solver is employed to evaluate and determine the eigen-mode frequencies and corresponding mode shapes of the system. As the first tangential (1T) and the second tangential (2T) modes are known to dominate [15], they will be the focus of this study. When the combustion process excites these acoustic modes, the system-level model will assess the stability characteristics. Figure 51 shows the first tangential mode for the unbaffled and baffled configurations, when no source terms are considered. The second tangential (2T) is shown in Fig. 52 for various axial cross sections in the combustor.

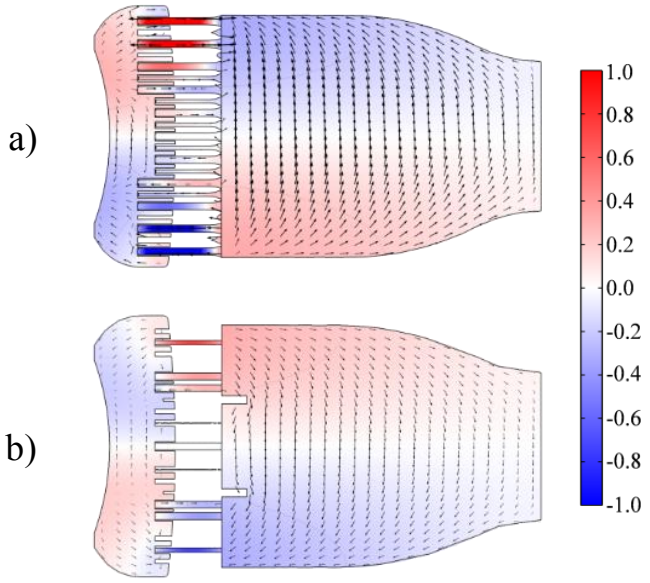

Figure 51. Pressure fields of 1T modes for a) unbaffled and b) baffled configuration

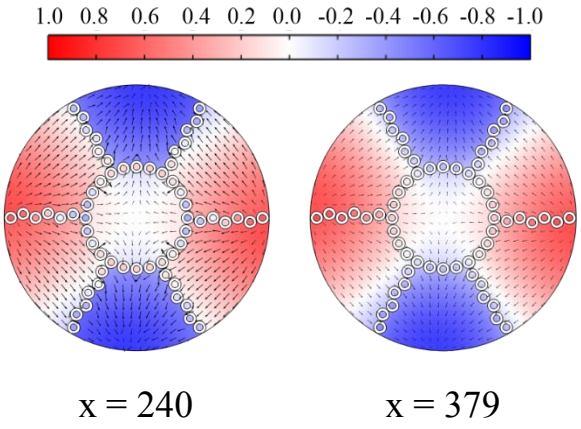

Figure 52. Axial cross sections of pressure and velocity fields for second tangential (2T) mode)

The addition of baffles decreases the frequency of oscillation, as consistent with previous studies [15]. As seen in the figure, the acoustic waves are longitudinal within the injectors. The tangential waves are longitudinalized within the injector components, as the geometry confinement forces the disturbances to change directions. As previously mentioned, there

are multiple damping mechanisms involved. It can be shown that the flow distributor and the injector themselves provide damping through vortex shedding and viscous dissipation [177]. Mean flow leads to convective losses of acoustic energy, as acoustic energy essentially flows out of the system. The eigenmode analysis not only gives the resonant frequencies and mode shapes of interest within the combustor, but also the stability margin in the form of the associated growth rate. This allows the engineer to compare how stable the designs are relative to each other, having the growth rate of the oscillations as the key stability margin indicator.

5.2 Distributed Combustion Response

The main cause of acoustic oscillations in combustion chambers is the heat release rate fluctuations. For an acoustic stability analysis to be useful, it must be supplemented with a model for this quantity. Due to the complexity of turbulent combustion processes, this modeling task represents one of the key challenges in the development of an accurate stability analysis.

The nature of the combustion in any device is highly dependent on the flowfield within the injectors. Due to the large range of physical regimes in which combustion can take place, it is difficult to establish a completely general theoretical model for combustion response. As previously mentioned, most existing theoretical models lack the ability to describe the spatial distribution of heat release without assumed parameters. The FTFs obtained from these models are global quantities, based on volumetric heat release within a specified combustion zone. In reality, the spatial distribution of heat release may have a profound effect on the acoustic stability of a combustor [125, 167]. A flame is said to be

acoustically (convectively) compact if the length scale of the flame is small relative to a typical acoustic (convective) wavelength. If so, then it may be possible to treat the heat release as occurring in a single plane for modeling purposes [125]. However, there is a significant gap in understanding of the stability behaviors of combustion systems in which the flame is acoustically compact but convectively noncompact. In such cases, the spatial distribution of the unsteady heat release and its interaction with the unsteady flowfield must be taken into account. Figure 53 shows the 1T mode FTF gain and phase obtained from the previous chapter. The maximum gain values occur just downstream of the injector faceplate. This distribution is used to populate all of the 331 MCC injectors present, and there is a certain degree of artificial inter-element interaction as the injector computation domains slightly overlap. Figure 54 shows the gain and phase for the 2T mode. The maximum is once again near the third slice shown, and corresponds to the location for the secondary flame stabilization mechanism. From the figures, it is evident that the recirculation zone in the taper region of the injectors serves as a critical design consideration.

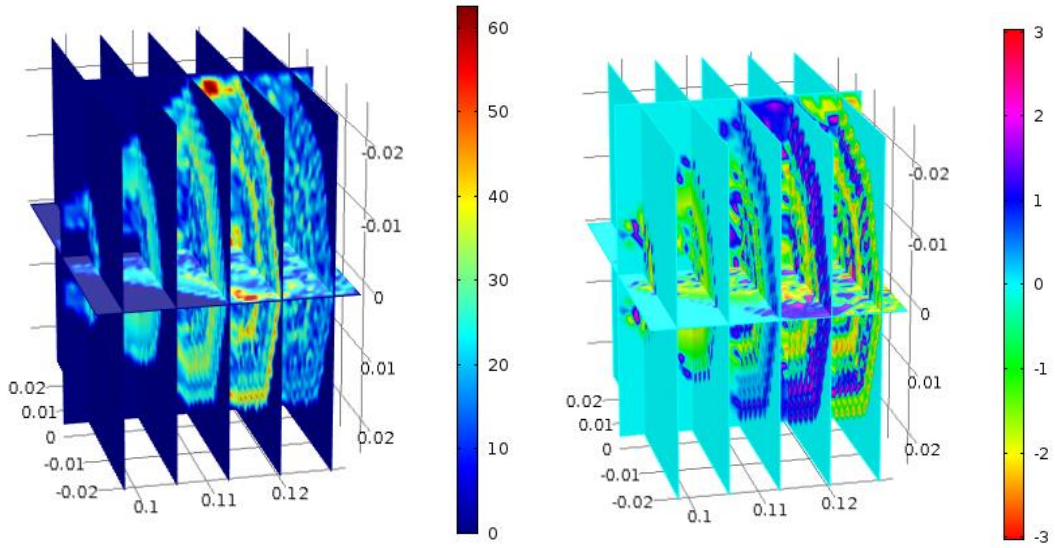

Figure 53. 1T mode FTF gain (left) and phase (right)

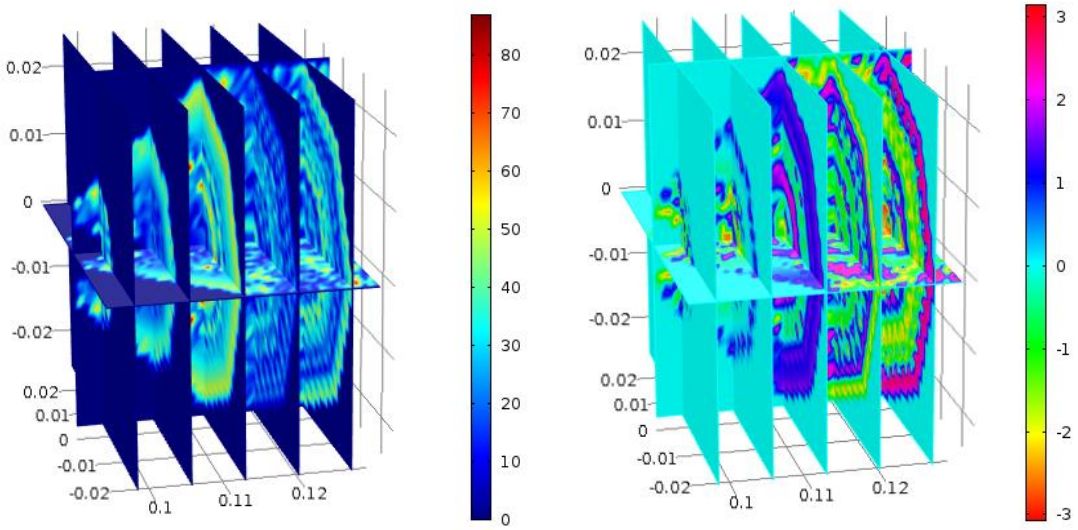

Figure 54. 2T mode FTF gain (left) and phase (right)

The level of detail made available by the combustion response extracted from LES is generous; however, there is still significant uncertainty associated with the FTF used in

the acoustic analysis. This is likely to be the most significant source of error for the acoustic eigenvalues and mode shapes, and a robust quantification of the sensitivities to FTF parameters should be undertaken. The spatially integrated combustion response functions that they employ may be characterized by as few as two scalar parameters – namely the gain and phase – which constitute a two-dimensional input space. If only a single acoustic mode is considered at a time, the frequency and growth rate also constitute a two-dimensional output space. An immediate difficulty arises when generalizing to a spatially distributed heat release. Considering that the gain and phase may take on values at any point in a continuum, the input space becomes in principle infinite-dimensional. For a sensitivity analysis of this new system to be sensible, a finite set of parameters which characterize the field must be chosen.

5.3 Conclusion

A linear acoustic analysis has been developed and applied to the main combustion chamber of an oxygen-rich staged-combustion engine. The work allows for the incorporation of acoustic source terms such as the combustion response. As a specific example, a combustion chamber similar to that of the RD-170 engine was considered, including the upstream oxidizer plenum, flow distributor, and injector assembly. A theoretical model for acoustic impedance based on unsteady vortex shedding at flow orifice rims was specified as a boundary condition at the flow distributor plate. An impedance model was also derived for viscous damping of acoustic waves within the injector assembly and incorporated into the model. The baseline results for the acoustic field indicate that communication between the main chamber and oxidizer plenum affected by the injectors is significant. Acoustic waves excited in the main chamber propagate upstream through the

injectors and interact with the oxidizer dome, where they are damped by the flow distributor.

Combustion response becomes the largest contributor to the stability margin of the system. Although the mode shapes and frequencies of interest are not drastically altered, the growth rates are amplified. The 1T mode is of greatest concern, seeing the largest gain. This must have been discovered during RD-170 development, as the baffle injectors are specifically designed to mitigate 1T oscillations. The 2T mode is then treated with injector tuning by adjusting the length of the MCC injectors.

CHAPTER 6. CONCLUSION

For high-performance power generation and propulsion systems, such as those of airbreathing and rocket engines, physical experiments are expensive due to the harsh requirements of operating conditions. High-fidelity simulations can be employed to capture more salient features of the flow and combustion dynamics in engines. Although these computations aid decision making during the development process, they are often too expensive and time-consuming for design and development purposes.

To enable usage of modeling/simulation in the design workflow, this thesis proposes a data-driven framework for modeling and analysis to facilitate decision making for combustor designs. Its core is a surrogate model employing a machine-learning technique called kriging, which is combined with data-driven basis functions to extract and model the underlying coherent structures from high-fidelity simulation results. This emulation framework encompasses key design parameter sensitivity analysis, physics-guided classification of design parameter sets, and flow evolution modeling for efficient design survey. A sensitivity analysis using Sobol' indices and a decision tree are incorporated into the framework to better inform the model. This information improves the surrogate model training process, which employs basis functions as regression functions over the design space for the kriging model. The novelty of the proposed approach is the construction of the model through Common Proper Orthogonal Decomposition, allowing for data-reduction and extraction of common coherent structures. The accuracy of prediction of mean flow features for new swirl injector designs is assessed and the dynamic flowfield is captured in the form of power spectrum densities. A key contribution is the

fact that dynamic information is retained and used for design, and the surrogate model is not simply attempting to optimize a single global metric. This data-driven framework also demonstrates the uncertainty quantification of predictions, providing a metric for model fit. The significantly reduced computation time required for evaluating new design points enables efficient survey of the design space.

To further utilize simulation results, a data analytic methodology to characterize the complex nature of turbulent combustion is used to analyze the system dynamics. Comprehensive combustion stability analysis has long been sought after, as a good understanding of the coupling process would reduce the amount of testing and level of capital required for engine development. A vital component is the quantification of the distributed combustion response. The proposed methodology leverages high-fidelity large eddy simulation (LES) of combustor components in combination with machine-learning techniques to quantify the spatial combustion response. This response is intended to serve as an acoustic source term in the generalized wave equation, which can be used to analyze the stability of complex propulsion systems. The extracted response provides the link between component-level and system-level analysis. The MBSE framework utilizing linear stability analysis. The results show that acoustic-vortical dynamics is the dominant mechanism determining flame stabilization. This data-driven methodology quantifies the gain and phase relationship between flowfield variables and unsteady heat release. The methodology not only accounts for the distributed combustion response through incorporation of proper orthogonal decomposition (POD) analysis, but also uses the data to identify relevant time scales, replacing the need for forcing and focusing on intrinsic dynamics.

The framework highlights the possibility of identifying a system-level analysis using component-level dynamic information. The rocket engine acoustic analysis is simply a demonstration, and the methodology can be applied to other propulsion systems. Moreover, if there is a type of system-level analysis that can use component-level dynamic simulations, the surrogate model and data analytics approach can translate over.

For future work, additional investigation should be carried out in dynamic regions of the flowfield, where the surrogate model had higher predictive uncertainties. One potential cause is the extreme range of the design points; this can be addressed by setting a smaller range. The uncertainty quantification and propagation of underlying flow couplings are also important research directions, and can perhaps be tackled using techniques such as support points. Another interesting path would be to improve the MaxPro methodology with minimax coverage. Although the smoothing effect from CPOD-based emulation appears to be mitigated with proper parameter tuning, the extension of the decision tree to automatically determine the optimal basis functions for a prediction, such as hierarchical clustering, could significantly improve the methodology's capability of surveying large design spaces. From an implementation point of view, another hurdle is computational efficiency, where the use of local Gaussian Process models appear to be an attractive option.

With respect to the distributed combustion response, the models derived analytically, under the assumption that combustion takes place in the wrinkled flamelet regime, can account for the spatial convolution of the combustion response. In premixed works, equivalence ration perturbations can cause fluctuations in the local flame speed and heat of reaction along the flame surface, which in turn cause local heat release oscillations.

Direct routes of influence include how flame speed and mixture heat of reaction fluctuations cause the local heat release to fluctuate. The resulting flame speed changes also excite flame wrinkles that propagate along the flame, which leads to variations in the burning area, again affecting the heat release rate. This indirect route of influence is non-local, and the flame area fluctuations are a convolution of the flame surface oscillations at all upstream locations at earlier times. The current methodology treats the POD time-varying coefficients as an autoregressive process, including the temporal convolution. The integral to relate any single downstream point to all points upstream to account for the "memory" of the flowfield was not implemented due to computational constraints. A local coordinate methodology to map out and quantify all propagating disturbances and their subsequent effects can be explored as a potential solution.

APPENDIX A. EIGENMODE ANALYSIS FRAMEWORK

The derivation follows the same approach as given in Culick et al. [136]. The formulation begins with the two-phase flow conservation equations in conservative form:

- Conservation of mass (gas phase)

$$\frac{\partial \rho_g}{\partial t} + \nabla \cdot \left(\rho_g \boldsymbol{u}\right) = w_\ell \tag{1}$$

- Conservation of mass (condensed phase)

$$\frac{\partial \rho_\ell}{\partial t} + \nabla \cdot \left(\rho_\ell \boldsymbol{u}_\ell\right) = -w_\ell \tag{2}$$

- Conservation of momentum

$$\frac{\partial}{\partial t}\left(\rho_g \boldsymbol{u} + \rho_\ell \boldsymbol{u}_\ell\right) + \nabla \cdot \left(\rho_g \boldsymbol{u}\boldsymbol{u} + \rho_\ell \boldsymbol{u}_\ell \boldsymbol{u}_\ell\right) + \nabla p = 0 \tag{3}$$

- Conservation of energy

$$\frac{\partial}{\partial t}\left(\rho_g e_0 + \rho_\ell e_{\ell 0}\right) + \nabla \cdot \left(\rho_g \boldsymbol{u} e_0 + \rho_\ell \boldsymbol{u}_\ell e_{\ell 0}\right) + \nabla \cdot \left(p\boldsymbol{u}\right) = Q \tag{4}$$

Here, the subscript g and subscript ℓ represents the gas phase and the condensed phase respectively; w_ℓ is the conversion of condensed mass to gas; and Q is the energy released in homogeneous reactions. The total specific energy of the gas phase and liquid phase are, respectively,

$$e_0 = C_v T + \frac{1}{2}\boldsymbol{u}\cdot\boldsymbol{u}$$

$$e_{\ell 0} = CT_\ell + \frac{1}{2}\boldsymbol{u}_\ell\cdot\boldsymbol{u}_\ell$$

The constant volume specific heat C_v pertains to the gaseous material and specific heat C to the liquid substance. The first step is to transform the conservation equations into a single-phase form that includes the effects of condensed species. Manipulation of Eqs. (3) and (4) results in

$$\rho_g \frac{\partial \boldsymbol{u}}{\partial t} + \rho_g \boldsymbol{u}\cdot\nabla\boldsymbol{u} + \nabla p = \boldsymbol{F}_\ell - \boldsymbol{\sigma}$$

$$\rho_g C_v \frac{\partial T}{\partial t} + \rho_g C_v \boldsymbol{u}\cdot\nabla T + p\nabla\cdot\boldsymbol{u} = Q + Q_\ell + (e_{\ell 0} - e_0)w_\ell + \boldsymbol{u}\cdot\boldsymbol{\sigma} + (\boldsymbol{u}_\ell - \boldsymbol{u})\cdot\boldsymbol{F}_\ell \tag{5}$$

where

$$\boldsymbol{F}_\ell = -\rho_\ell\left(\frac{\partial \boldsymbol{u}_\ell}{\partial t} + \boldsymbol{u}_\ell\cdot\nabla\boldsymbol{u}_\ell\right),\ \boldsymbol{\sigma} = (\boldsymbol{u} - \boldsymbol{u}_\ell)w_\ell,\ \text{and}\ \ Q_\ell = -\rho_\ell C\left(\frac{\partial T_\ell}{\partial t} + \boldsymbol{u}_\ell\cdot\nabla T_\ell\right) \tag{6}$$

Defining

$$\delta\boldsymbol{u}_\ell = \boldsymbol{u}_\ell - \boldsymbol{u},\ \delta T_\ell = T_\ell - T,\ \text{and}\ \rho = \rho_g + \rho_\ell = \rho_g(1 + C_m) \tag{7}$$

Eqs. (1) and (2) can be manipulated:

$$\frac{\partial \rho}{\partial t} + \boldsymbol{u}\cdot\nabla\rho = \mathcal{W} \tag{8}$$

with $\mathcal{W} = -\rho\nabla\cdot\boldsymbol{u} - \nabla\cdot(\rho_\ell\delta\boldsymbol{u}_\ell)$. Using those same definitions, Eq. (5) can be further simplified to

$$\rho \frac{\partial \boldsymbol{u}}{\partial t} + \rho \boldsymbol{u} \cdot \nabla \boldsymbol{u} + \nabla p = \boldsymbol{\mathcal{F}}$$

$$\rho \bar{C}_v \left(\frac{\partial T}{\partial t} + \boldsymbol{u} \cdot \nabla T \right) = -p \nabla \cdot \boldsymbol{u} + Q + \delta Q + (e_{\ell 0} - e_0) w_\ell + \boldsymbol{u} \cdot \boldsymbol{\sigma} + \delta \boldsymbol{u}_\ell \cdot \boldsymbol{F}_\ell \tag{9}$$

Where

$$\boldsymbol{\mathcal{F}} = -\rho_\ell \left(\frac{\partial \delta \boldsymbol{u}_\ell}{\partial t} + \delta \boldsymbol{u}_\ell \cdot \nabla \delta \boldsymbol{u}_\ell + \delta \boldsymbol{u}_\ell \cdot \nabla \boldsymbol{u} + \boldsymbol{u} \cdot \nabla \delta \boldsymbol{u}_\ell \right) - \boldsymbol{\sigma}$$

$$\delta Q = -\rho_\ell C_v \left(\frac{\partial \delta T_\ell}{\partial t} + \delta \boldsymbol{u}_\ell \cdot \nabla \delta T_\ell + \delta \boldsymbol{u}_\ell \cdot \nabla T + \boldsymbol{u} \cdot \nabla \delta T_\ell \right)$$

and the mass-weighted specific heat values can be defined as

$$\bar{C}_v = \frac{C_v + C_m C}{1 + C_m}, \text{ and } \bar{C}_p = \frac{C_p + C_m C}{1 + C_m}$$

Here $C_m = \rho_\ell / \rho_g$ is the density ratio of the condensed phase to the gaseous phase. The perfect gas law can be modified from $p = \rho_g R T$, describing the gas only, to

$$p = \frac{\rho R T}{1 + C_m} = \rho \bar{R} T$$

where $\bar{R} = \bar{C}_p - \bar{C}_v$ is the mass-weighted specific gas constant. Additionally, the speed of sound can be written as

$$\bar{a} = (\bar{\gamma} \bar{R} T)^{1/2} = \left[\frac{\bar{\gamma}}{1 + C_m} \left(\frac{p}{\rho_g} \right) \right]^{1/2}$$

where $\bar{\gamma} = \bar{C}_p/\bar{C}_v$ is the mass-weighted specific heat ratio. The addition of Eq. (8) multiplied by $\bar{R}T$ to Eq. (9) multiplied by $\bar{R}/\bar{C}_v$ with the application of the perfect gas law and further manipulations results in

$$\frac{\partial p}{\partial t} + \bar{\gamma} p \nabla \cdot \boldsymbol{u} = -\boldsymbol{u} \cdot \nabla p + \mathcal{P} \tag{10}$$

With

$$\mathcal{P} = \frac{\bar{R}}{\bar{C}_v}[Q + \delta Q + \delta \boldsymbol{u}_\ell \cdot \boldsymbol{F}_\ell + (e_{\ell 0} - e_0) w_\ell + \boldsymbol{u} \cdot \boldsymbol{\sigma} - \bar{C}_v \nabla \cdot (\rho_\ell \delta \boldsymbol{u}_\ell)]$$

This completes the formulation of the conservation equations incorporating the effects of the condensed material. Next, the nonlinear wave equation can be derived. The dependent variables can be split into mean and fluctuating components:

$$\rho(\boldsymbol{r}, t) = \bar{\rho} + \rho'(\boldsymbol{r}, t), \quad \boldsymbol{u}(\boldsymbol{r}, t) = \overline{\boldsymbol{u}}(\boldsymbol{r}) + \boldsymbol{u}'(\boldsymbol{r}, t), \; p(\boldsymbol{r}, t) = \bar{p} + p'(\boldsymbol{r}, t), \quad \ldots$$

The fluctuating quantities are assumed to be much smaller than the mean quantities:

$$p' \ll \bar{p}, \quad \rho' \ll \bar{\rho}, \quad \boldsymbol{u}' \ll \overline{\boldsymbol{u}}, \quad \ldots$$

Substitution of the decomposed forms of the dependent variables into Eqs. (9) and (10) yields

$$\begin{gathered}(\bar{\rho} + \rho')\frac{\partial \boldsymbol{u}'}{\partial t} + \bar{\rho}(\overline{\boldsymbol{u}} \cdot \nabla \boldsymbol{u}' + \boldsymbol{u}' \cdot \nabla \overline{\boldsymbol{u}} + \boldsymbol{u}' \cdot \nabla \boldsymbol{u}') + \nabla p' = \boldsymbol{\mathcal{F}}' \\ \frac{\partial p'}{\partial t} + \bar{\gamma} p' \nabla \cdot (\overline{\boldsymbol{u}} + \boldsymbol{u}') + \bar{\gamma} \bar{p} \nabla \cdot \boldsymbol{u}' = -(\overline{\boldsymbol{u}} + \boldsymbol{u}') \cdot \nabla p' + \mathcal{P}'\end{gathered} \tag{11}$$

From Eq. (11), the partial derivative of the fluctuating velocity can be defined as

$$\frac{\partial \boldsymbol{u}'}{\partial t} = \frac{1}{\bar{\rho}}\left[-\nabla p' - \bar{\rho}(\bar{\boldsymbol{u}} \cdot \nabla \boldsymbol{u}' + \boldsymbol{u}' \cdot \nabla \bar{\boldsymbol{u}} + \boldsymbol{u}' \cdot \nabla \boldsymbol{u}') - \rho' \frac{\partial \boldsymbol{u}'}{\partial t} + \boldsymbol{\mathcal{F}}'\right] \tag{12}$$

Finally, taking the partial derivative of Eq. (11), inserting the definition from Eq. (12), and manipulating the outcome results in the nonlinear wave equation:

$$\frac{1}{\bar{\rho}\bar{a}^2}\frac{\partial^2 p'}{\partial t^2} - \frac{1}{\bar{\rho}}\nabla^2 p' = \mathcal{M} - \frac{1}{\bar{\rho}}\nabla \cdot \boldsymbol{\mathcal{D}} \tag{13}$$

Here,

$$\mathcal{M} = \frac{1}{\bar{\rho}\bar{a}^2}\left(\bar{\boldsymbol{u}} \cdot \nabla \frac{\partial p'}{\partial t} + \frac{\partial}{\partial t}(\boldsymbol{u}' \cdot \nabla p') + \bar{\gamma}\frac{\partial p'}{\partial t}\nabla \cdot \bar{\boldsymbol{u}} + \bar{\gamma}\frac{\partial}{\partial t}(p'\nabla \cdot \boldsymbol{u}') - \frac{\partial \mathcal{P}'}{\partial t}\right)$$

contains the monopole source terms, and

$$\boldsymbol{\mathcal{D}} = \bar{\rho}(\bar{\boldsymbol{u}} \cdot \nabla \boldsymbol{u}' + \boldsymbol{u}' \cdot \nabla \bar{\boldsymbol{u}}) + \left(\bar{\rho}\boldsymbol{u}' \cdot \nabla \boldsymbol{u}' + \rho' \frac{\partial \boldsymbol{u}'}{\partial t}\right) - \boldsymbol{\mathcal{F}}'$$

encompasses the dipole source terms.

If the pressure is assumed to be time-harmonic,

$$p'(\boldsymbol{r}, t) = p'(\boldsymbol{r})e^{i\omega t}$$

Eq. (13) simplifies to an inhomogeneous Helmholtz equation:

$$-\frac{\omega^2 p'}{\bar{\rho}\bar{a}^2} - \frac{1}{\bar{\rho}}\nabla^2 p' = \mathcal{M} - \frac{1}{\bar{\rho}}\nabla \cdot \boldsymbol{\mathcal{D}} \tag{14}$$

where ω is the angular eigenfrequency that can be converted to eigenfrequency f by dividing by 2π. The density $\bar{\rho}$ and sound speed $\bar{a}$ can be complex-valued to simulate losses due to viscosity or porous materials. Most of the analysis assumes there are no monopole or dipole sources. Equation (14) thus reduces to the homogenous form of the Helmholtz equation:

$$-\frac{\omega^2 p'}{\bar{\rho}\bar{a}^2} - \frac{1}{\bar{\rho}}\nabla^2 p' = 0 \tag{15}$$

APPENDIX B. GREEN'S FUNCTION

The Green's function acting on distributions satisfies the equation:

$$(k^2 - \nabla^2)G(x|x_0) = \delta(x - x_0) \tag{1}$$

where $\delta(x - x_0)$ is the delta function in three dimensions. An integral equation for $\hat{p}$ can then be found by multiplying Eq. (4.8) by G and Eq. (1) by $\hat{p}$, subtracting the two equations, and integrating over the volume of the combustor:

$$\hat{p}(\boldsymbol{r}) = \iiint G(\boldsymbol{x}|\boldsymbol{x_0})h(\boldsymbol{x_0}, \hat{p})dV \tag{2}$$

The traditional solution of G is the solution for a unit harmonic source, a delta function, placed at $\boldsymbol{x_0}$ and subject to proper boundary conditions.

REFERENCES

[1] Lieuwen, T.C., Yang, V., *Combustion Instabilities in Gas Turbine Engines: Operational Experience, Fundamental Mechanisms and Modeling*, Progress in Astronautics and Aeronautics, Vol. 210 (2005). doi: 10.2514/4.866807.

[2] Lieuwen, T.C., Yang, V., *Gas Turbine Emissions*, Cambridge University Press, Cambridge, England, U.K. (2013). doi: 10.2514/1.J053061.

[3] Yang, V., Brill, T.B., Ren, W.-Z., *Solid Propellant Chemistry Combustion and Motor Interior Ballistics*, Progress in Astronautics and Aeronautics, Vol. 185, (2000). doi: 10.2514/4.866562.

[4] Yang, V., Habiballah, M., Hulka, J., Popp, M., *Liquid Rocket Thrust Chambers: Aspects of Modeling, Analysis, and Design*, Progress in Astronautics and Aeronautics, Vol. 200, (2004). doi: 10.2514/4.866760.

[5] O'Connor, J., Acharya, V., and Lieuwen, T.C., "Transverse Combustion Instabilities: Acoustic, Fluid Mechanic, and Flame Processes," *Progress in Energy and Combustion Science* 49 (2015) 1–39. doi: 10.1016/j.pecs.2015.01.001.

[6] Gröning, S., Hardi, J.S., Suslov, D., Oschwald, M., "Injector-Driven Combustion Instabilities in a Hydrogen/Oxygen Rocket Combustor," *Journal of Propulsion and Power*, 32 (2016) 560-573. doi: 10.2514/1.B35768.

[7] Poinsot, T., Veynante, D., *Theoretical and Numerical Combustion*. RT Edwards, Inc., (2005). ISBN-13: 978-1930217102

[8] Huang, Y., Yang, V., "Dynamics and Stability of Lean-premixed Swirl-stabilized Combustion," *Progress in Energy and Combustion Science*, 35 (2009) 293-364. doi: 10.1016/j.pecs.2009.01.002.

[9] Bazarov, V.G., Yang, V., "Liquid-propellant Rocket Engine Injector Dynamics," *Journal of Propulsion and Power*, 14 (1998) 797-806. http://doi.org/10.2514/2.5343

[10] Bazarov, V., Yang, V., Puri, P., "Design and Dynamics of Jet and Swirl injectors," *Liquid Rocket Thrust Chambers: Aspects of Modeling, Analysis, and Design*,

Progress in Astronautics and Aeronautics, Vol. 200 (2004), Chapter 2, pp. 19-103. http://doi.org/10.2514/5.9781600866760.0019.0103.

[11] Wang, X., Yang, V., "Supercritical Mixing and Combustion of Liquid-Oxygen/ Kerosene Bi-Swirl Injectors," *Journal of Propulsion and Power*, 33 (2017) 316-322. http://doi.org/10.2514/1.B36262.

[12] Zong, N., Yang, V., "Cryogenic Fluid Dynamics of Pressure Swirl Injectors at Supercritical Conditions," *Physics of Fluids*, 20 (2008), 056103. http://doi.org/10.1063/1.2905287.

[13] Wang, X., Huo, H., Wang, Y., Yang, V., "Comprehensive Study of Cryogenic Fluid Dynamics of Swirl Injectors at Supercritical Conditions," *AIAA Journal* (2017). http://doi.org/10.2514/1.J055868

[14] Sutton, G. P., and Biblarz, O., *Rocket Propulsion Elements*, 8th Edition, John Wiley & Sons, Inc. (2010), New Jersey, U.S.A. ISBN-13: 978-0470080245.

[15] Dranovsky, M. L., *Combustion Instabilities in Liquid Rocket Engines: Testing and Development Practices in Russia*. Progress in Astronautics and Aeronautics. American Institute of Aeronautics and Astronautics (2007). http://arc.aiaa.org/doi/book/10.2514/4.866906.

[16] Parsley, R. C. and Zhang, B., "Thermodynamic Power Cycles for Pump-Fed Liquid Rocket Engines," *Liquid Rocket Thrust Chambers: Aspects of Modeling, Analysis, and Design*, Progress in Astronautics and Aeronautics, Vol. 200 (2004), Chap. 18. http://doi.org/10.2514/5.9781600866760.0621.0648

[17] Oefelein, J. C., and Yang, V., "Comprehensive Review of Liquid-Propellant Combustion Instabilities in F-1 Engines." *Journal of Propulsion and Power* 9, no. 5 (1993), 657–77. http://doi.org/10.2514/3.23674.

[18] You, D., Ku, D. D., and Yang, V., "Acoustic Waves in Baffled Combustion Chamber with Radial and Circumferential Blades." *Journal of Propulsion and Power* 29, no. 6 (2013): 1453–67. doi:10.2514/1.B34923.

[19] Rahman, S., Pal, S., and Santoro, R., "Swirl Coaxial Atomization - Cold-Flow and Hot-Fire Experiments." In 33rd Aerospace Sciences Meeting and Exhibit. American Institute of Aeronautics and Astronautics (1995) http://arc.aiaa.org/doi/abs/10.2514/6.1995-381.

[20] Kenny, J. R., Moser, M. D., Hulka, J., and Jones, G., "Cold Flow Testing for Liquid Propellant Rocket Injector Scaling and Throttling," 42nd AIAA/ASME/SAE/ASEE Joint Propulsion Conference (2006). http://ntrs.nasa.gov/search.jsp?R=20060047749.

[21] Santoro, R. J., and Merkle, C. L., "Main Chamber and Preburner Injector Technology," Final Report for NASA Cooperative Agreement Grant No. NCC 8-46 (1999). http://ntrs.nasa.gov/search.jsp?R=19990049416.

[22] Miller, K., Sisco, J., Nugent, N., and Anderson, W., "Combustion Instability with a Single-Element Swirl Injector." *Journal of Propulsion and Power* 23, no. 5 (2007): 1102–12. https://doi.org/10.2514/1.26826.

[23] Selle, L., Blouquin, R., Théron, M., Dorey, L.-H., Schmid, Martin, and Anderson, W., "Prediction and Analysis of Combustion Instabilities in a Model Rocket Engine." *Journal of Propulsion and Power* 30, no. 4 (2014): 978–90. https://doi.org/10.2514/1.B35146.

[24] Morgan, C. J., Shipley, K. J., and Anderson, W. E., "Comparative Evaluation Between Experiment and Simulation for a Transverse Instability." *Journal of Propulsion and Power* 31, no. 6 (2015): 1696–1706. https://doi.org/10.2514/1.B35759.

[25] Harvazinski, M., Huang, C., Sankaran, V., Feldman, T., Anderson, W., Merkle, C., and Talley, D. G., "Coupling between Hydrodynamics, Acoustics, and Heat Release in a Self-Excited Unstable Combustor." *Physics of Fluids* 27, no. 4 (2015): 045102. https://doi.org/10.1063/1.4916673.

[26] Chen, W., Allen, J. K., Mavris, D. N., and Mistree, F., "A Concept Exploration Method for Determining Robust Top-level Specifications," *Engineering Optimization* 26, no. 2 (1996), 137-158. https:// doi.org/10.1080/03052159608941114.

[27] Myers, R. H. and Montgomery, D. C., Anderson-Cook, C. M., *Response Surface Methodology: Process and Product Optimization Using Designed Experiments*, 3rd Edition, John Wiley & Sons, Inc., New York, U.S.A. (2009). ISBN-13: 987-0470174463.

[28] Queipo, N. V., Haftka, R. T., Shyy, W., Goel, T., Vaidyanathan, R., and Tucker, P. K., "Surrogate-Based Analysis and Optimization." Progress in Aerospace Sciences 41, no. 1 (2005), 1–28. https://doi.org/10.1016/j.paerosci.2005.02.001.

[29] Santner, T.J., Williams, B.J., Notz, W.I., *The Design and Analysis of Computer Experiments*, Springer Science & Business Media, New York, U.S.A. (2013). ISBN: 978-1-4419-2992-1.

[30] Manski, D., Goertz, C., Sassnick, H.-D., Hulka, J. R., Goracke, B. D., and Levack, D. J. H., "Cycles for earth-to-orbit propulsion", *Journal of Propulsion and Power* 14, no. 5 (1998), 588–604. doi:10.2514/2.5351.

[31] Vasin, A. A., Kamensky, S. D., Katorgin, B. I., Kolesnikov, A. I., Nosov, V. P., Stavrulov, A. I., Fedorov, V. V., Chvanov, V. K., "Liquid-propellant rocket engine chamber and its casing". US6244041 B1, filed September 10, 1999, and issued June 12, 2001. http://www.google.com/patents/US6244041.

[32] Richardson, R., "Linear and Non Linear Dynamics of Swirl Injectors," PhD Thesis, Department of Aeronautics and Astronautics, Purdue University (2006)

[33] Ismailov, M., and Heister, S. D., "Dynamic Response of Rocket Swirl Injectors, Part I: Wave Reflection and Resonance." *Journal of Propulsion and Power* 27, no. 2 (2011): 402–411. https://doi.org/10.2514/1.B34044

[34] Ismailov, M., and Heister, S. D., "Dynamic Response of Rocket Swirl Injectors, Part II: Nonlinear Dynamic Response." *Journal of Propulsion and Power* 27, no. 2 (2011): 412–421. https://doi.org/10.2514/1.B34045

[35] Fu, Q.-F., and Yang, L.-J., "Theoretical and Experimental Study of the Dynamics of a Liquid Swirl Injector." *Journal of Propulsion and Power* 26, no. 1 (2010), 94–101. https://doi.org/10.2514/1.44271.

[36] Yang, L.-J., and Fu, Q.-F., "Theoretical Study of Dynamic Characteristic of Open-End Liquid Swirl Injector." *57th International Astronautical Congress*. American Institute of Aeronautics and Astronautics (2006). https://doi.org/10.2514/6.IAC-06-C4.P.3.09.

[37] Matas, J.-P., Hong, M., and Cartellier, A., "Stability of a Swirled Liquid Film Entrained by a Fast Gas Stream." *Physics of Fluids* 26, no. 4 (2014), 042108. https://doi.org/10.1063/1.4871395.

[38] Wang, X., Zhang, L., Li, Y., Yeh, S.-T., and Yang, V., "Supercritical combustion of gas-centered liquid-swirl coaxial injectors", *Journal of Propulsion and Power*, submitted 2018.

[39] Zong, N., Meng, H., Hsieh, S.-Y., and Yang, V., "A Numerical Study of Cryogenic Fluid Injection and Mixing under Supercritical Conditions." *Physics of Fluids* 16, no. 12 (2004), 4248–4261. https://doi.org/10.1063/1.1795011

[40] Yang, V., and Culick, F. E. C., "On the Existence and Stability of Limit Cycles for Transverse Acoustic Oscillations in a Cylindrical Combustion Chamber. 1: Standing Modes." *Combustion Science and Technology* 72, no. 1-3 (1990), 37–65. https://doi.org/10.1080/00102209008951639

[41] Harrje, D. T., "Liquid propellant rocket combustion instability", Technical Report, SP-194, NASA (1972). http://ntrs.nasa.gov/search.jsp?R=19720026079.

[42] Kenny, R. J., Hulka, J. R., Moser, M. D., and Rhys, N. O., "Effect of Chamber Backpressure on Swirl Injector Fluid Mechanics." *Journal of Propulsion and Power* 25, no. 4 (2009), 902–913. https://doi.org/10.2514/1.38537

[43] Chen, X., and Yang, V., "Effect of Ambient Pressure on Liquid Swirl Injector Flow Dynamics." *Physics of Fluids* 26, no. 10 (2014), 102104. https://doi.org/10.1063/1.4899261

[44] Kim, S., Khil, T., Kim, D., and Yoon, Y., "Effect of Geometric Parameters on the Liquid Film Thickness and Air Core Formation in a Swirl Injector." *Measurement Science and Technology* 20, no. 1 (2009), 015403. http://doi.org/10.1088/0957-0233/20/1/015403

[45] Bazarov, V., "Design of Injectors for Self-Sustaining of Combustion Chambers Acoustic Stability," International Symposium on Energy Conversion Fundamentals, Moscow Inst. of Aviation Technology (2004). http://doi.org/10.2514/6.2006-4722

[46] **"**International Council on Systems Engineering, Systems Engineering Vision 2020*,"* INCOSE-TP-2004-004-02, Version/Revision: 2.03, Dated September 2007

[47] Mavris, D.N., DeLaurentis, D.A., Bandte, O., and Hale, M.A., "A Stochastic Approach to Multi-disciplinary Aircraft Analysis and Design", 36th AIAA Aerospace Sciences Meeting and Exhibit, Aerospace Sciences Meetings, American Institute of Aeronautics and Astronautics, AIAA 98-0912 (1998). https://doi.org/10.2514/6.1998-912

[48] Forrester, A. I. J., Sóbester, A., and Keane, A. J., "Multi-Fidelity Optimization via Surrogate Modelling," *Proceedings of the Royal Society of London A:*

Mathematical, Physical and Engineering Sciences 463, no. 2088 (2007), 3251–69. https://doi.org/10.1098/rspa.2007.1900.

[49] Kennedy, M. C., and O'Hagan, A., "Predicting the Output from a Complex Computer Code When Fast Approximations Are Available." *Biometrika* 87, no. 1 (2000), 1–13.

[50] Qian, P. Z. G., and Wu, C. F. J., "Bayesian Hierarchical Modeling for Integrating Low-Accuracy and High-Accuracy Experiments." *Technometrics* 50, no. 2 (2008), 192–204. https://doi.org/10.1198/004017008000000082.

[51] Alexandrov, N. M., Lewis, R. M., Gumbert, C. R., Green, L. L., and Newman, P. A., "Approximation and Model Management in Aerodynamic Optimization with Variable-Fidelity Models." *Journal of Aircraft* 38, no. 6 (2001), 1093–1101. https://doi.org/10.2514/2.2877.

[52] Shyy, W., Papila, N., Vaidyanathan, R., and Tucker, K., "Global Design Optimization for Aerodynamics and Rocket Propulsion Components." *Progress in Aerospace Sciences* 37, no. 1 (2001), 59–118. https://doi.org/10.1016/S0376-0421(01)00002-1.

[53] Simpson, Y. W., Mauery, T. M., Korte, J. J., and Mistree, F., "Kriging Models for Global Approximation in Simulation-Based Multidisciplinary Design Optimization." *AIAA Journal* 39, no. 12 (2001), 2233–41. https://doi.org/10.2514/2.1234.

[54] Jeong, S., Murayama, M., and Yamamoto, K., "Efficient Optimization Design Method Using Kriging Model." *Journal of Aircraft* 42, no. 2 (2005), 413–20. https://doi.org/10.2514/1.6386.

[55] Xiong, Y., Chen, W., and Tsui, K.-L., "A New Variable-Fidelity Optimization Framework Based on Model Fusion and Objective-Oriented Sequential Sampling." *Journal of Mechanical Design* 130, no. 11 (2008), 111401-111401–9. https://doi.org/10.1115/1.2976449.

[56] Robinson, T. D., Eldred, M. S., Willcox, K. E., and Haimes, R., "Surrogate-Based Optimization Using Multifidelity Models with Variable Parameterization and Corrected Space Mapping." *AIAA Journal* 46, no. 11 (2008), 2814–22. https://doi.org/10.2514/1.36043.

[57] Bui-Thanh, T., Willcox, K., and Ghattas, O., "Model Reduction for Large-Scale Systems with High-Dimensional Parametric Input Space." *SIAM Journal on Scientific Computing* 30, no. 6 (2008), 3270–88. https://doi.org/10.1137/070694855.

[58] Sacks, J., Welch, W. J., Mitchell, T. J., and Wynn, H. P., "Design and Analysis of Computer Experiments." *Statistical Science* 4, no. 4 (1989), 409–23. https://doi.org/10.1214/ss/1177012413.

[59] Simpson, T., Toropov, V., Balabanov, V., and Viana, F., "Design and Analysis of Computer Experiments in Multidisciplinary Design Optimization: A Review of How Far We Have Come - Or Not." In 12th AIAA/ISSMO Multidisciplinary Analysis and Optimization Conference. American Institute of Aeronautics and Astronautics (2008). http://arc.aiaa.org/doi/abs/10.2514/6.2008-5802.

[60] Choi, S., Alonso, J. J., and Kroo, I. M., "Two-Level Multifidelity Design Optimization Studies for Supersonic Jets." *Journal of Aircraft* 46, no. 3 (2009), 776–90. https://doi.org/10.2514/1.34362.

[61] Han, Z., Zimmerman, R., and Görtz, S., "Alternative Cokriging Method for Variable-Fidelity Surrogate Modeling." *AIAA Journal* 50, no. 5 (2012), 1205–10. https://doi.org/10.2514/1.J051243.

[62] March, A., and Willcox, K., "Provably Convergent Multifidelity Optimization Algorithm Not Requiring High-Fidelity Derivatives." *AIAA Journal* 50, no. 5 (2012), 1079–89. https://doi.org/10.2514/1.J051125.

[63] Peherstorfer, B., Willcox, K., and Gunzburger, M., "Survey of Multifidelity Methods in Uncertainty Propagation, Inference, and Optimization." Technical Report Aerospace Computational Design Laboratory TR-16-1 (2016), n.d. https://doi.org/10.1007/s00158-016-1550-y.

[64] Mavris, D.N., "Application of Machine Learning for Aircraft Design", CDT – Big Data Analytics and Machine Intelligence Team Hosting, Machine Learning Technologies and Their Applications to Scientific and Engineering Domains Workshop (2016), Pearl Young and Reid 1, NASA Langley Research Center, Hampton, VA.

[65] Matheron, G., "Principles of Geostatistics," *Economic Geology*, 58 (1963), 1246-1266. https://doi: 10.2113/gsecongeo.58.8.1246

[66] Mak, S., Sung, C.-L., Wang, X., Yeh, S.-T., Chang, Y.-H., Joseph, V.R., Yang, V., Wu, C. F.J., "An Efficient Surrogate Model for Emulation and Physics Extraction of Large Eddy Simulations," *Journal of American Statistical Association*, (2017).

[67] Williams, B., Higdon, D., Gattiker, J., Moore, L., McKay, M., Keller-McNulty, S., "Combining Experimental Data and Computer Simulations, with an Application to Flyer Plate Experiments," *Bayesian Analysis*, 1 (2006), 765-792. http://doi: 10.1214/06-BA125

[68] Rougier, J., "Efficient Emulators for Multivariate Deterministic Functions," *Journal of Computational and Graphical Statistics*, 17 (2008), 827-843. http://doi: 10.1198/106186008X384032

[69] Hung, Y., Joseph, V.R., Melkote, S.N., "Analysis of Computer Experiments with Functional Response," *Technometrics*, 57 (2015), 35-44. http://doi: 10.1080/00401706.2013.869263

[70] Qian, P.Z.G., Wu, H., Wu, C.J., "Gaussian Process Models for Computer Experiments with Qualitative and Quantitative Factors," *Technometrics*, 50 (2008), 383-396. http://doi: 10.1198/004017008000000262

[71] Zhou, Q., Qian, P.Z., Zhou, S., "A Simple Approach to Emulation for Computer Models with Qualitative and Quantitative Factors," *Technometrics*, 53 (2011), 266-273. http://doi: 10.1198/TECH.2011.10025

[72] Bayarri, M., Berger, J., Cafeo, J., Garcia-Donato, G., Liu, F., Palomo, J., Parthasarathy, R., Paulo, R., Sacks, J., Walsh, D., "Computer Model Validation with Functional Output," *The Annals of Statistics* (2007), 1874-1906. http://doi: : 10.1214/009053607000000163

[73] Banerjee, S., Gelfand, A.E., Finley, A.O., Sang, H., "Gaussian Predictive Process Models for Large Spatial Data Sets," *Journal of the Royal Statistical Society: Series B* (Statistical Methodology), 70 (2008), 825-848. http://doi: 10.1111/j.1467-9868.2008.00663.x

[74] Nguyen, V. B., Buffoni, M., Willcox, K., and Khoo, B. C., "Model Reduction for Reacting Flow Applications." *International Journal of Computational Fluid Dynamics* 28, no. 3–4 (2014), 91–105. https://doi.org/10.1080/10618562.2014.911848.

[75] Ling, J., and Templeton, J., "Evaluation of Machine Learning Algorithms for Prediction of Regions of High Reynolds Averaged Navier Stokes Uncertainty." *Physics of Fluids* 27, no. 8 (2015), 085103. https://doi.org/10.1063/1.4927765.

[76] Singh, A.P., and Duraisamy, K., "Using Field Inversion to Quantify Functional Errors in Turbulence Closures." *Physics of Fluids* 28, no. 4 (2016), 045110. https://doi.org/10.1063/1.4947045.

[77] Parish, E. J., and Duraisamy, K., "A Paradigm for Data-Driven Predictive Modeling Using Field Inversion and Machine Learning." *Journal of Computational Physics* 305 (2016), 758–74. https://doi.org/10.1016/j.jcp.2015.11.012.

[78] Ling, J., Kurzawski, A., and Templeton, J., "Reynolds Averaged Turbulence Modelling Using Deep Neural Networks with Embedded Invariance." *Journal of Fluid Mechanics* 807 (2016), 155–66. https://doi.org/10.1017/jfm.2016.615.

[79] Wang, J.-X., Wu, J.-L., and Xiao, H., "Physics-Informed Machine Learning for Predictive Turbulence Modeling: Using Data to Improve RANS Modeled Reynolds Stresses." *arXiv:1606.07987 [Physics]*, (2016). http://arxiv.org/abs/1606.07987

[80] Qian, Z., Seepersad, C. C., Joseph, V. R., Allen, J. K., and Wu, C. F. J., "Building Surrogate Models Based on Detailed and Approximate Simulations." *Journal of Mechanical Design* 128, no. 4 (2005), 668–77. https://doi.org/10.1115/1.2179459.

[81] Willcox, K., and Peraire, J., "Balanced Model Reduction via the Proper Orthogonal Decomposition." *AIAA Journal* 40, no. 11 (2002), 2323–30. https://doi.org/10.2514/2.1570.

[82] Lucia, D. J., and Beran, P. S., "Projection Methods for Reduced Order Models of Compressible Flows." *Journal of Computational Physics* 188, no. 1 (2003), 252–80. https://doi.org/10.1016/S0021-9991(03)00166-9.

[83] Rowley, C. W., Colonius, T., Murray, R. M., "Model Reduction for Fluids, Using Balanced Proper Orthogonal Decomposition." *International Journal of Bifurcation and Chaos* 15, no. 03 (2005), 997–1013.

[84] Walton, S., Hassan, O., and Morgan, K., "Reduced Order Modelling for Unsteady Fluid Flow Using Proper Orthogonal Decomposition and Radial Basis Functions." *Applied Mathematical Modelling* 37, no. 20–21 (2013), 8930–45. https://doi.org/10.1016/j.apm.2013.04.025.

[85] Benner, P., Gugercin, S., and Willcox, K., “A Survey of Projection-Based Model Reduction Methods for Parametric Dynamical Systems.” *SIAM Review* 57, no. 4 (2015), 483–531. https://doi.org/10.1137/130932715.

[86] Lumley, J.L., "The Structure of Inhomogeneous Turbulent Flows," *Atmospheric Turbulence and Radio Wave Propagation*, 790 (1967), 166-178.

[87] Loève, M., *Probability Theory: Foundations, Random Sequences*, van Nostrand Princeton, NJ, 1955.

[88] Higdon, D., Gattiker, J., Williams, B., Rightley, M., "Computer Model Calibration using High-dimensional Output," *Journal of the American Statistical Association*, 103 (2008) 570-583. doi: 10.1198/016214507000000888

[89] Wang, X., Wang, Y., Yang, V., "Geometric Effects on Liquid Oxygen/Kerosene Bi-Swirl Injector Flow Dynamics at Supercritical Conditions," *AIAA Journal*, Vol. 55, No. 10 (2017). http://doi.org/10.2514/1.J055952

[90] Yang, V., "Modeling of Supercritical Vaporization, Mixing, and Combustion Processes in Liquid-fueled Propulsion Systems," *Proceedings of the Combustion Institute*, 28 (2000), 925-942. http://doi.org//10.1016/S0082-0784(00)80299-4

[91] Meng, H., Yang, V., "A Unified Treatment of General Fluid Thermodynamics and its Application to a Preconditioning Scheme," *Journal of Computational Physics*, 189 (2003), 277-304. http://doi.org//10.1016/S0021-9991(03)00211-0

[92] Zong, N., Yang, V., "An efficient preconditioning scheme for real-fluid mixtures using primitive pressure–temperature variables," *International Journal of Computational Fluid Dynamics*, Vol. 21, Issue 5-6 (2007), 217-230. https://doi.org/10.1080/10618560701584373

[93] Joseph, V.R., Gul, E., and Ba, S., "Maximum Projection Designs for Computer Experiments," *Biometrika*, 102 (2015), 371-380. http://doi.org/10.1093/biomet/asv002

[94] Loeppky, J.L., Sacks, J., and Welch, W.J., "Choosing the Sample Size of a Computer Experiment: A Practical Guide," *Technometrics*, 51 (2009), 366-376. http://doi.org/10.1198/TECH.2009.08040

[95] Sobol', I.M., "Global Sensitivity Indices for Nonlinear Mathematical Models and their Monte Carlo estimates," *Mathematics and Computers in Simulation*, 55 (2001), 271-280. http://doi.org/10.1016/S0378-4754(00)00270-6

[96] Wu, C.J., Hamada, M.S., *Experiments: Planning, Analysis, and Optimization*, John Wiley & Sons, New York, U.S.A. (2011). ISBN: 978-0-471-69946-0

[97] Sobol', I.M., "Distribution of Points in a Cube and Integration Nets," *Uspekhi Matematicheskikh Nauk*, 21 (1966) 271-272.

[98] Geurts, P., Irrthum, A., and Wehenkel, L., "Supervised Learning with Decision tree-based Methods in Computational and Systems Biology," *Molecular Biosystems*, 5 (2009), 1593-1605. http://doi.org/10.1039/B907946G

[99] Blockeel, H., Schietgat, L., Struyf, J., Džeroski, S., and Clare, A., "Decision Trees for Hierarchical Multilabel Classification: A Case Study in Functional Genomics," European Conference on Principles of Data Mining and Knowledge Discovery, Springer, Berlin (2006), 18-29. http://doi.org/10.1007/11871637_7

[100] Friedman, J., Hastie, T., and Tibshirani, R., *The Elements of Statistical Learning*, Springer Series in Statistics Springer, Berlin, (2001). ISBN: 978-0-387-84857-0

[101] Breiman, L., Friedman, J., Stone, C.J., Olshen, R.A., *Classification and Regression Trees*, CRC Press, London (1984). ISBN-13: 978-0412048418

[102] Xiao, M., Breitkopf, P., Coelho, R. Filomeno, Knopf-Lenoir, C., Sidorkiewicz, M., and Villon, P., "Model Reduction by CPOD and Kriging," *Structural and Multidisciplinary Optimization*, 41 (2010), 555-574. http://doi.org/10.1007/s00158-009-0434-9

[103] Joseph, V.R., and Kang, L., "Regression-based Inverse Distance Weighting with Applications to Computer Experiments," *Technometrics*, 53 (2011), 254-265. http://doi.org/10.1198/TECH.2011.09154

[104] Dexter, C. E., Fisher, M. F., Hulka, J., Denisov, K. P., Shibanov, A. A., and Agarkov, A. F., "Scaling Techniques for Design, Development, and Test," *Liquid Rocket Thrust Chambers: Aspects of Modeling, Analysis, and Design*, Progress in Astronautics and Aeronautics, Vol. 200, (2004), Chapter 16, 553-600. http://doi.org/10.2514/5.9781600866760.0553.0600

[105] Rasmussen, C.E. and Williams, C.K.I., *Gaussian Processes for Machine Learning*, the MIT Press (2006). ISBN: 9780262182539

[106] Casella, G., Berger, R.L., *Statistical Inference*, Duxbury Press, Pacific Grove, CA, (2002). ISBN-10: 8131503941

[107] Liu, D.C., and Nocedal, J., "On the Limited Memory BFGS Method for Large Scale Optimization," *Mathematical Programming*, 45 (1989), 503-528. http://doi.org/10.1007/BF01589116

[108] Ranjan, P., Bingham, D., and Michailidis, G., "Sequential Experiment Design for Contour Estimation From Complex Computer Codes," *Technometrics*, Vol. 50, no. 4, 527-547 (2008). http://doi.org/10.1198/004017008000000541.

[109] Zinn, B. T., and Lieuwen, T. C., *Combustion instabilities: Basic Concepts, Combustion Instabilities in Gas Turbine Engines: Operational Experience, Fundamental Mechanisms, and Modeling*, edited by T. C. Lieuwen and V. Yang, Progress in Astronautics and Aeronautics, Vol. 210, AIAA, Reston, VA, 2005, Chap. 1.

[110] Strutt, J.W. (Lord Rayleigh), "The Explanation of Certain Acoustic Phenomena", *Nature* 18, no. 145 (1878), 319–321.

[111] Crocco, L., "Aspects of Combustion Instability in Liquid Propellant Rocket Motors," Part I, *J. Am. Rocket Soc.* 21 (1951) 163–178.

[112] Crocco, L., "Aspects of Combustion Instability in Liquid Propellant Rocket Motors," Part II, *J. Am. Rocket Soc.* 22 (1952) 7–16.

[113] Harrje, D. T., "Liquid Propellant Rocket Combustion Instability," Technical Report, SP-194, NASA, January 1, 1972. http://ntrs.nasa.gov/search.jsp?R=19720026079.

[114] Duvvur, A., C. H. Chiang, and Sirignano, W. A., "Oscillatory Fuel Droplet Vaporization - Driving Mechanism for Combustion Instability." *Journal of Propulsion and Power* 12, no. 2 (1996), 358–65. http://doi.org/10.2514/3.24036.

[115] Bazarov, V. G., and Yang, V., "Liquid-Propellant Rocket Engine Injector Dynamics." *Journal of Propulsion and Power* 14, no. 5 (1998), 797–806. http://doi.org/10.2514/2.5343.

[116] Yang, V., and Anderson, W. E., *Liquid Rocket Engine Combustion Instability*. Vol. 169. Progress in Astronautics and Aeronautics. American Institute of Aeronautics and Astronautics (1995). http://arc-test.aiaa.org/doi/book/10.2514/4.866371.

[117] Oefelein, J. C., and Yang, V., "Modeling High-Pressure Mixing and Combustion Processes in Liquid Rocket Engines", *Journal of Propulsion and Power* Vol. 14, no. 5 (1998), 843-857. https://doi.org/10.2514/2.5349.

[118] Yang, V., "Modeling of Supercritical Vaporization, Mixing, and Combustion Processes in Liquid-Fueled Propulsion Systems," *Proceedings of the Combustion Institute*, Vol. 28 (2000), 925-942. http://doi.org/10.1016/S0082-0784(00)80299-4

[119] Poinsot, T., and Veynante, D., *Theoretical and Numerical Combustion*. RT Edwards, Inc. (2005).

[120] Zhang, L., Wang, X., Li, Y., Yeh, S.-T., and Yang, V., "Supercritical Fluid Flow Dynamics and Mixing in a Gas-Centered Liquid-Swirl Coaxial Injector", *Physics of Fluids*, submitted 2018.

[121] Li, Y., Wang, X., Zhang, L., Yeh, S.-T., and Yang, V., "A Parametric Study of Gas-Centered Liquid-Swirl Coaxial Injector Flow Dynamics at Supercritical Conditions, *AIAA Journal*, submitted 2018.

[122] Wang, X., Zhang, L., Li, Y., Yeh, S.-T., and Yang, V., "Supercritical Combustion of Gas-Centered Liquid-Swirl Coaxial Injectors," *Journal of Propulsion and Power*, submitted 2018.

[123] Li, H. G., Zong, N., Lu, X. Y., and Yang, V., "A Consistent Characteristic Boundary Condition for General Fluid Mixture and its Implementation in a Preconditioning Scheme," *Advances in Applied Mathematics and Mechanics* Vol. 4, no. 1 (2012), 72-92. https://doi.org/10.4208/aamm.11-m1160

[124] Bodony, D. J., "Analysis of Sponge Zones for Computational Fluid Mechanics," *Journal of Computational Physics* Vol. 212, no. 2 (2006), 681-702. https://doi.org/10.1016/j.jcp.2005.07.014

[125] Dowling, A. P., "The Calculation of Thermoacoustic Oscillations," *Journal of Sound and Vibration* 180, no. 4 (1995), 557–81. http://doi.org/10.1006/jsvi.1995.0100.

[126] Keller, J. J., "Thermoacoustic Oscillations in Combustion Chambers of Gas Turbines," *AIAA Journal* 33, no. 12 (1995), 2280–87. http://doi.org/10.2514/3.12980.

[127] Dowling, A. P., "A Kinematic Model of a Ducted Flame," *Journal of Fluid Mechanics* 394 (1999), 51–72. http://doi.org/10.1017/S0022112099005686.

[128] Paschereit, C. O., Schuermans, B., Polifke, W., and Mattson, O., "Measurement of Transfer Matrices and Source Terms of Premixed Flames," *Journal of Engineering for Gas Turbines and Power* 124, no. 2 (2002), 239–47. http://doi.org/10.1115/1.1383255.

[129] Pankiewitz, C., and Sattelmayer, T., "Time Domain Simulation of Combustion Instabilities in Annular Combustors," *Journal of Engineering for Gas Turbines and Power* 125, no. 3 (2003), 677–85. http://doi.org/10.1115/1.1582496.

[130] Dowling, A. P., and Stow, S.R., "Acoustic Analysis of Gas Turbine Combustors," *Journal of Propulsion and Power* 19 (2003), 751–764. https://doi.org/10.2514/2.6192

[131] Roux, S., Lartigue, G., Poinsot, T., Meier, U., Bérat, C., "Studies of Mean and Unsteady Flow in a Swirled Combustor using Experiments, Acoustic Analysis, and Large Eddy Simulations," *Combustion and Flame* 141 (2005), 40–54. https://doi.org/10.1016/j.combustflame.2004.12.007

[132] Giauque, A., Selle, L., Gicquel, L., Poinsot, T., Buechner, H., Kaufmann, P., and Krebs, W., "System Identification of a Large-Scale Swirled Partially Premixed Combustor using LES and Measurements," *Journal of Turbulence* 6 (2005), N21. http://doi.org/10.1080/14685240512331391985.

[133] Huang, Y., Wang, S., and Yang, V., "Systematic Analysis of Lean-Premixed Swirl-Stabilized Combustion," *AIAA Journal* 44, no. 4 (2006), 724–40. http://doi.org/10.2514/1.15382

[134] Nicoud, F., Benoit, L., Sensiau, C., and Poinsot, T., "Acoustic Modes in Combustors with Complex Impedances and Multidimensional Active Flames," *AIAA Journal* 45, no. 2 (2007), 426–41. http://doi.org/10.2514/1.24933.

[135] Urbano, A., Douasbin, Q., Selle, L., Staffelbach, G., Cuenot, B., Schmitt, T., Ducruix, S., and Candel, S., "Study of Flame Response to Transverse Acoustic Modes from the LES of a 42-Injector Rocket Engine," *Proceedings of the Combustion Institute* Vol. 36, no. 2 (2017), 2633-2639 http://doi.org/10.1016/j.proci.2016.06.042.

[136] Culick, F. E. C., and Yang, V., Overview of Combustion Instabilities in Liquid-Propellant Rocket Engines, *Liquid Rocket Engine Combustion Instability*, edited by V. Yang and W. E. Anderson, Progress in Astronautics and Aeronautics, Vol. 169, AIAA, Washington, DC (1995), Chap. 1.

[137] Strahle, W.C., "On Combustion Generated Noise," *Journal of Fluid Mechanics* 49, no. 2 (1971), 399–414. http://doi.org/10.1017/S0022112071002167.

[138] Fleifil, M., Annaswamy, A. M., Ghoneim, Z. A., and Ghoniem, A. F., "Response of a Laminar Premixed Flame to Flow Oscillations: a Kinematic Model and Thermoacoustic Instability Results," *Combustion and Flame* 106, no. 4 (1996), 487–510. http://doi.org/10.1016/0010-2180(96)00049-1.

[139] You, D., Huang, Y., and Yang, V., "A Generalized Model of Acoustic Response of Turbulent Premixed Flame and its Application to Gas-Turbine Combustion Instability Analysis," *Combustion Science and Technology* 177, no. 5–6 (2005),1109–50. http://doi.org/10.1080/00102200590927012.

[140] Preetham, Santosh, H., and Lieuwen, T., "Dynamics of Laminar Premixed Flames Forced by Harmonic Velocity Disturbances," *Journal of Propulsion and Power* 24, no. 6 (2008), 1390–1402. http://doi.org/10.2514/1.35432.

[141] Ducruix, S., Durox, D., and Candel, S., "Theoretical and Experimental Determinations of the Transfer Function of a Laminar Premixed Flame," *Proceedings of the Combustion Institute* 28, no. 1 (2000), 765–73. http://doi.org/10.1016/S0082-0784(00)80279-9.

[142] Noiray, N., Durox, D., Schuller, T., and Candel, S., "A Unified Framework for Nonlinear Combustion Instability Analysis Based on the Flame Describing Function," *Journal of Fluid Mechanics* 615 (2008), 139–67. http://doi.org/10.1017/S0022112008003613.

[143] Palies, P., Durox, D., Schuller, T., and Candel, S., "The Combined Dynamics of Swirler and Turbulent Premixed Swirling Flames," *Combustion and Flame* 157, no. 9 (2010), 1698–1717. http://doi.org/10.1016/j.combustflame.2010.02.011.

[144] Palies, P., Durox, D., Schuller, T., and Candel, S., "Nonlinear Combustion Instability Analysis Based on the Flame Describing Function Applied to Turbulent Premixed Swirling Flames," *Combustion and Flame* 158, no. 10 (2011), 1980–91. http://doi.org/10.1016/j.combustflame.2011.02.012.

[145] McManus, K. R., Poinsot, T., and Candel, S., "A Review of Active Control of Combustion Instabilities," *Progress in Energy and Combustion Science* 19, no. 1 (1993), 1–29. http://doi.org/10.1016/0360-1285(93)90020-F.

[146] Bendat, J., and Piersol, A., *Random Data: Analysis and Measurement Procedures*, Wiley, New York (1986).

[147] Fung, Y.-T., and Yang, V., "Active Control of Nonlinear Pressure Oscillations in Combustion Chambers," *Journal of Propulsion and Power* 8, no. 6 (1992), 1282–89. http://doi.org/10.2514/3.11474.

[148] Koshigoe, S., Komatsuzaki, T., and Yang, V., "Adaptive Control of Combustion Instability with On-line System Identification," *Journal of Propulsion and Power* 15, no. 3 (1999), 383–89. http://doi.org/10.2514/2.5456.

[149] Dowling, A.P., Morgans, A.S., "Feedback Control of Combustion Oscillations," *Annual Review of Fluid Mechanics* 37 (2005), 151–182. http://doi.org/10.1146/annurev.fluid.36.050802.122038.

[150] Lieuwen, T. C., "Experimental Investigation of Limit-Cycle Oscillations in an Unstable Gas Turbine Combustor," *Journal of Propulsion and Power* 18, no. 1 (2002), 61–67. http://doi.org/10.2514/2.5898.

[151] Polifke, W., Poncet, A., Paschereit, C. O., and Döbbeling, K., "Reconstruction of Acoustic Transfer Matrices by Instationary Computational Fluid Dynamics," *Journal of Sound and Vibration* 245, no. 3 (2001), 483–510. http://doi.org/10.1006/jsvi.2001.3594.

[152] Huber, A., Polifke, W., "Dynamics of Practical Premixed Flames, Part II: Identification and Interpretation of CFD Data," *International Journal of Spray and*

Combustion Dynamics 1 (2009), 229–249. https://doi.org/10.1260/175682709788707440

[153] Tay-Wo-Chong, L., Bomberg, S., Ulhaq, A., Komarek, T., and Polifke, W., "Comparative Validation Study on Identification of Premixed Flame Transfer Function," *Journal of Engineering for Gas Turbines and Power* 134, no. 2 (2012), 021502. https://doi.org/10.1115/1.4004183.

[154] Polifke, W., "Black-Box System Identification for Reduced Order Model Construction," *Annals of Nuclear Energy* 67 (2014), 109–28. https://doi.org/10.1016/j.anucene.2013.10.037

[155] Silva, C. F., Emmert, T., Jaensch, S., and Polifke, W., "Numerical Study on Intrinsic Thermoacoustic Instability of a Laminar Premixed Flame," *Combustion and Flame* 162, no. 9 (2015), 3370–78. http://doi.org/10.1016/j.combustflame.2015.06.003. 24

[156] Sovardi, C., Jaensch, S., and Polifke, W., "Concurrent Identification of Aero-Acoustic Scattering and Noise Sources at a Flow Duct Singularity in Low Mach Number Flow," *Journal of Sound and Vibration* 377 (2016), 90–105. http://doi.org/10.1016/j.jsv.2016.05.025.11.

[157] Berkooz, G., Holmes, P., and Lumley, J. L., "The Proper Orthogonal Decomposition in the Analysis of Turbulent Flows," *Annual Review of Fluid Mechanics* 25, no. 1 (1993), 539-575.

[158] Sirovich, L., Kirby, M., and Winter, M., "An Eigenfunction Approach to Large Scale Transitional Structures in Jet Flow," *Physics of Fluids A: Fluid Dynamics* 2, no. 2 (1990), 127–36. http://doi.org/10.1063/1.857815.

[159] Box, G. E. P., and Jenkins, G. M, *Time Series Analysis, Control, and Forecasting*, San Francisco, CA: Holden Day 3226.3228 (1976), 10.

[160] McCullagh, P., and Nelder, J. A., *Generalized Linear Models*, Vol. 37. CRC Press (1989). ISBN-13: 978-0412317606

[161] Friedman, J., Hastie, T., and Tibshirani, R., *The Elements of Statistical Learning*, Springer, Berlin (2001). ISBN-13: 978-0387848570

[162] Zhang, C.-H., "Nearly Unbiased Variable Selection Under Minimax Concave Penalty," *The Annals of Statistics* Vol. 38, no. 2 (2010), 894-942. http://doi.org/10.1214/09-AOS729

[163] Mazumder, R., Friedman, J. H., and Hastie, T, "SparseNet: Coordinate Descent with Nonconvex Penalties," *Journal of the American Statistical Association*, Vol. 106, 495 (2011), 1125-1138. https://doi.org/10.1198/jasa.2011.tm09738

[164] Urbano, A., Selle, L., Staffelbach, G., Cuenot, B., Schmitt, T., Ducruix, S., and Candel, S., "Exploration of Combustion Instability Triggering using Large Eddy Simulation of a Multiple Injector Liquid Rocket Engine," *Combustion and Flame* 169 (2016), 129–40. http://doi.org/10.1016/j.combustflame.2016.03.020.

[165] Komarek, T., and Polifke, W., "Impact of Swirl Fluctuations on the Flame Response of a Perfectly Premixed Swirl Burner," *Journal of Engineering for Gas Turbines and Power* 132, no. 6 (2010), 061503–061503. http://doi.org/10.1115/1.4000127.

[166] Bellows, B. D., Bobba, M. K., Seitzman, J. M., and Lieuwen, T., "Nonlinear Flame Transfer Function Characteristics in a Swirl-Stabilized Combustor," *Journal of Engineering for Gas Turbines and Power* 129, no. 4 (2006), 954-961. http://doi.org/10.1115/1.2720545.

[167] Kim, K. T., Lee, J. G., Quay, B. D., and Santavicca, D. A., "Spatially Distributed Flame Transfer Functions for Predicting Combustion Dynamics in Lean Premixed Gas Turbine Combustors," *Combustion and Flame* 157, no. 9 (2010), 1718–30. http://doi.org/10.1016/j.combustflame.2010.04.016.

[168] Truffin, K., and Poinsot, T., "Comparison and Extension of Methods for Acoustic Identification of Burners," *Combustion and Flame* 142, no. 4 (2005), 388–400. http://doi.org/10.1016/j.combustflame.2005.04.001.

[169] Huang, Y., and Yang, V., "Dynamics and Stability of Lean-Premixed Swirl-Stabilized Combustion," *Progress in Energy and Combustion Science* 35 (2009), 293–364. https://doi.org/10.1016/j.pecs.2009.01.002.

[170] Law, C. K, and Sung, C. J, "Structure, Aerodynamics, and Geometry of Premixed Flamelets," *Progress in Energy and Combustion Science* 26, no. 4–6 (2000), 459–505. http://doi.org/10.1016/S0360-1285(00)00018-6.

[171] O'Connor, J., and Lieuwen, T., "Recirculation Zone Dynamics of a Transversely Excited Swirl Flow and Flame," *Physics of Fluids* 24, no. 7 (2012), 075107. http://doi.org/10.1063/1.4731300.

[172] Lu, X., Wang, S., Sung, H.-G., Hsieh, S.-Y., and Yang, V., "Large-Eddy Simulations of Turbulent Swirling Flows Injected into a Dump Chamber," *Journal of Fluid Mechanics* 527 (2005), 171–95. http://doi.org/10.1017/S0022112004002927.

[173] De Luca, L., Price, E. W., and Summerfield, M., "Prediction of the Stability of Unsteady Motions in Solid-Propellant Rocket Motors," *Nonsteady Burning and Combustion Stability of Solid Propellants*., Vol. 143, Progress in Astronautics and Aeronautics (1992), 719-779. https://doi.org/10.2514/5.9781600866159.0719.0779.

[174] Martin, C. E., Benoit, L. J.-L., Sommerer, Y., Nicoud, F., and Poinsot, T., "Large-Eddy Simulation and Acoustic Analysis of a Swirled Staged Turbulent Combustor," *AIAA Journal*, Vol. 44, no. 4 (2006), 741-750. https://doi.org/10.2514/1.14689.

[175] Howe, M. S., "On the Theory of Unsteady High Reynolds Number Flow Through a Circular Aperture," *Proceedings of the Royal Society of London A: Mathematical, Physical and Engineering Sciences*, Vol. 366, no. 1725 (1979), 205-223. http://doi.org/10.1098/rspa.1979.0048

[176] Wang, T.-S., "Thermophysics Characterization of Kerosene Combustion," *Journal of Thermophysics and Heat Transfer*, Vol. 15, no. 2 (2001), 140-147. https://doi.org/10.2514/2.6602

[177] Lioi, C., Ku, D., and Yang, V., "Linear Acoustic Analysis of Main Combustion Chamber of an Oxidizer-Rich Staged Combustion (ORSC) Engine," *Journal of Propulsion and Power*, submitted (2018).